

**NANOGAP-ENABLED STUDY OF ELECTRODE REACTIONS BY SCANNING
ELECTROCHEMICAL MICROSCOPY**

by

Nikoloz Nioradze

BS, Georgian Technical University, 1993

MS, University of Pittsburgh, 2010

Submitted to the Graduate Faculty of
The Kenneth P. Dietrich School of Arts and Sciences in partial fulfillment
of the requirements for the degree of
Doctor of Philosophy

University of Pittsburgh

2014

UNIVERSITY OF PITTSBURGH
DIETRICH SCHOOL OF ARTS AND SCIENCES

This dissertation was presented

by

Nikoloz Nioradze

It was defended on

December 5, 2014

and approved by

David H. Waldeck, Professor, Department of Chemistry

Adrian C. Michael, Professor, Department of Chemistry

Minhee Yun, Associate Professor, Department of Electrical & Computer Engineering

Dissertation Advisor: Shigeru Amemiya, Associate Professor, Department of Chemistry

Copyright © by Nikoloz Nioradze

2014

**NANOGAP-ENABLED STUDY OF ELECTRODE REACTIONS BY SCANNING
ELECTROCHEMICAL MICROSCOPY**

Nikoloz Nioradze, PhD

University of Pittsburgh, 2014

The nanogap quasi-steady-state voltammetry, developed in my work, presents the way to monitor and study rapid electron transfer reactions on macroscopic substrates of scanning electrochemical microscopy (SECM). It combines the cyclic voltammetry and SECM and monitors substrate reaction as a tip current. The resulting plot of i_T versus E_S features the retraceable sigmoidal shape of a quasi-steady state voltammogram although a transient peak-shape voltammogram is obtained simultaneously at the macroscopic substrate. This simplifies measurement and analysis of a quasi-steady-state voltammogram and gives information about thermodynamic as well as kinetic parameters of the reaction taking place at the interface. No charging current at the amperometric tip, high and adjustable mass transport under the tip and high spatial resolution are all advantages of quasi-steady-state voltammetry. I also introduced generalized theory for nanoscale i_T - E_S voltammetry of substrate reactions with arbitrary reversibility and mechanism under comprehensive experimental conditions including any substrate potential and both SECM modes (feedback and substrate generation tip collection, SG/TC). I nanofabricated submicrometer size highly reliable Pt SECM tips and found the way of protection of these tiny electrodes from the damage caused either by electrostatic discharge or electrochemical etching. Subsequent application of quasi-steady-state voltammetry and reliable nanofabricated SECM probes enabled sensitive detection of adsorption of organic impurities from air and ultrapure water to the HOPG surface as evidenced by redox reaction of ferrocenylmethyl)trimethyl ammonium (FcTMA⁺). Study revealed that hydrophobic contaminant layer slows down the access of hydrophilic aqueous redox species to the underlying HOPG surface, thereby yielding a lower standard rate constant, k^0 . Moreover, this barrier effects stronger to a

more charged form (FcTMA^{2+}) of a redox couple so that the electron-transfer reaction of the more hydrophilic form is slower to yield a lower k^0 value.

TABLE OF CONTENTS

1.0 INTRODUCTION.....	1
1.1 REFERENCES.....	4
2.0 QUASI-STEADY-STATE VOLTAMMETRY of RAPID ELECTRON	
TRANSFER REACTIONS AT THE MACROSCOPIC SUBSTRATE OF THE	
SCANNING ELECTROCHEMICAL MICROSCOPE	5
2.1 INTRODUCTION.....	5
2.2 THEORY.....	8
2.2.1 Model.....	8
2.2.2 Geometrical Requirements for Quasi-Steady-State Voltammetry.....	10
2.2.3 Requirement of Reversible Substrate Reaction for	
Quasi-Steady-State Voltammetry.....	13
2.2.4 Analytical Expressions for Quasi-Steady-State Voltammograms.....	14
2.2.5 Kinetic Analysis of a Pair of Quasi-Steady-State Voltammograms.....	16
2.3 EXPERIMENTAL SECTION.....	17
2.3.1 Chemicals.....	17
2.3.2 SECM Measurement.....	17
2.4 RESULTS AND DISCUSSION.....	18
2.4.1 Reversible ET Reaction of FcMeOH.....	18
2.4.2 Nearly Reversible ET Reaction of TCNQ.....	21
2.5 CONCLUSIONS.....	24
2.6 SUPPORTING INFORMATION.....	25
2.6.1 Finite Element Simulation.....	25
2.6.2 Mediator Concentrations under Quasi-Steady-State Conditions.....	29

2.6.3	Effect of Unequal Diffusion Coefficients on i_T-E_S Voltammograms.....	29
2.6.4	Reversibility of Substrate Voltammograms.....	30
2.6.5	Equilibrium Mediator Concentrations at the Surface of a Macroscopic Substrate.....	31
2.6.6	Kinetically Limited i_T-E_S Voltammograms with Partially Retraceable Regions.....	32
2.6.7	Analytical Equations for Quasi-Steady-State i_T-E_S Voltammograms.....	33
2.6.8	Analytical Equations for Quasi-Steady-State i_T-E_S Voltammograms for Species R (FcMeOH).....	37
2.6.9	Effects of Thermodynamic and Kinetic Parameters.....	38
2.6.10	Tip Fabrication and Characterization.....	39
2.6.11	Observation of Current Spikes in i_T-E_S Voltammograms.....	41
	ACKNOWLEDGMENT.....	43
	2.7 REFERENCES.....	44
3.0	GENERALIZED THEORY FOR NANOSCALE VOLTAMMETRIC MEASUREMENTS OF HETEROGENEOUS ELECTRON-TRANSFER KINETICS AT MACROSCOPIC SUBSTRATES BY SCANNING ELECTROCHEMICAL MICROSCOPY.....	47
3.1	INTRODUCTION.....	47
3.2	MODEL.....	50
3.3	RESULTS AND DISCUSSION.....	54
3.3.1	Simulations of Nanoscale i_T-E_S Voltammograms Based on the MHC Formalism.....	54
3.3.2	Determination of Kinetic Parameters from MHC Responses.....	57
3.3.3	Analytical Equations for Nanoscale i_T-E_S Voltammograms.....	61
3.3.4	Experimental Observation of MHC Limiting Current.....	64

3.4 CONCLUSIONS.....	67
3.5 SUPPORTING INFORMATION.....	68
3.5.1 Finite Element Simulation.....	68
3.5.2 Analytical Equation for Irreversible Substrate Reactions (Eq. 15).....	72
3.5.3 Analytical Equations for Quasi-Steady-State i_T-E_S Voltammograms (Eq.17, 18).....	73
ACKNOWLEDGMENT.....	76
3.6 REFERENCES.....	77
4.0 ORIGINS OF NANOSCALE DAMAGE TO GLASS SEALED PLATINUM ELECTRODES WITH SUBMICROMETER AND NANOMETER SIZE.....	81
4.1 INTRODUCTION.....	81
4.2 ELECTROSTATIC DISCHARGE AND PROTECTION AGAINST IT.....	83
4.3 EXPERIMENTAL SECTION.....	83
4.3.1 Electrode Fabrication and Characterization.....	83
4.3.2 Electrostatic Discharge caused by Operator.....	84
4.3.3 Electrochemical Damage of Electrode by Potentiostat.....	88
4.3.4 Protection Against Damage of Electrode.....	90
4.4 CONCLUSION.....	90
4.5 SUPPORTING INFORMATION.....	91
4.5.1 Chemicals.....	91
4.5.2 Fabrication of Glass-Sealed Pt UMEs.....	91
4.5.3 ESD Protections.....	92
4.5.4 SEM Characterization of Pt UMEs.....	93
4.5.5 X-Ray EDS of Electrochemically Damaged Pt UMEs.....	94

4.5.6	Electrochemical Measurements.....	95
4.5.7	Activation and Inactivation of the “Cell on between Runs” Function.....	95
4.5.8	Electrochemical Damage during CV Measurement.....	96
4.5.9	Current Paths for Tip Damage.....	97
	ACKNOWLEDGMENT.....	99
4.6	REFERENCES.....	100
5.0	ORGANIC CONTAMINATION OF HIGHLY ORIENTED PYROLYTIC GRAPHITE AS STUDIED BY SCANNING ELECTROCHEMICAL MICROSCOPY.....	103
5.1	INTRODUCTION.....	103
5.2	EXPERIMENTAL SECTION.....	106
5.2.1	Chemicals and Materials.....	106
5.2.2	Water Purification.....	107
5.2.3	Tip Fabrication.....	107
5.2.4	SECM Measurement.....	108
5.3	RESULTS AND DISCUSSION.....	109
5.3.1	Clean Surface of Pt Tips.....	109
5.3.2	Approach Curve at HOPG in Filtered Water.....	110
5.3.3	Nanogap Voltammetry at HOPG in Filtered Water.....	111
5.3.4	Highly Positive Approach Curve at HOPG in UV-Treated Water.....	114
5.3.5	High Electroactivity of HOPG in ~ 1 ppb TOC Water.....	116
5.3.6	Effects of Contaminations from Air and Water.....	119
5.4	CONCLUSIONS.....	121
5.5	SUPPORTING INFORMATION.....	122
5.5.1	FIB Milling.....	122

5.5.2	Feedback Current at Tip-Substrate Contact.....	123
5.5.3	Sealed SECM Cell.....	125
5.5.4	Water Purification with Old Filters.....	125
5.5.5	CV of FcTMA ⁺ at HOPG.....	126
5.5.6	Elemental Analysis of Ultrapure Water.....	127
5.5.7	Tunneling Current Between the Tip and HOPG.....	127
	ACKNOWLEDGMENT.....	129
5.6	REFERENCES.....	130
6.0	CONCLUSIONS.....	133

LIST OF TABLES

Table 3-1. Reaction parameters and requirements for observing a kinetic limiting currents at HOPG.....	75
Table 5-1. Parameters from Figure 5-4A.....	113
Table 5-2. Parameters from Figure 5-6.....	119
Table 5-3. Concentrations of Various Elements in Ultrapure Water.....	127

LIST OF FIGURES

Figure 2-1. Scheme of SECM experiments in the (a) steady-state positive feedback mode, and in (b) feedback and (c) SG/TC modes for a quasireversible substrate reaction under the tip.....7

Figure 2-2. Reversible i_T-E_S voltammograms simulated for various tip-substrate distances (solid curves). Closed circles represent eqs 6 and 8. The inset shows a simultaneously simulated reversible voltammogram at the substrate.....11

Figure 2-3. Effect of D_R/D_O on i_T-E_S voltammograms simulated for $L = 0.25$ (solid curves). Closed circles represent 6 and 8.....12

Figure 2-4. Effect of normalized standard ET rate constant, λ_O' , on simulated i_T-E_S voltammograms (solid curves). Simulated reversible curves are represented by black dotted lines, which nearly overlap with curves for $\lambda_O' = 10$. Closed circles represent eqs 6 and 8.....14

Figure 2-5. Quasi-steady-state i_T-E_S voltammograms for 0.5 mM FcMeOH (solid lines) as obtained using a 0.48- μm -radius Pt tip with $RG = 1.5$ in feedback (top) and SG/TC (bottom) modes at various tip-substrate distances. The tip was held at 0.35 or 0.05 V vs Ag/AgCl for feedback or SG/TC modes, respectively. The substrate potential was cycled at 50 mV/s. Closed circles represent reversible theoretical voltammograms (eqs 44 and 46 supporting Information). The inset shows a reversible voltammogram as simultaneously measured at the substrate.....20

Figure 2-6. Quasi-steady-state i_T-E_S voltammograms for TCNQ (solid lines) The tip was held at -0.235 or 0 V vs Ag for feedback or SG/TC modes, respectively. Substrate potential was cycled at 50 mV/s. The inset shows a reversible voltammogram simultaneously measured at the substrate (with a peak separation of 61mV).....22

Figure 2-7. Geometry of a SECM diffusion problem in the cylindrical coordinate. The simulation space (light blue) is surrounded by seven boundaries (red, blue, and green lines). Boundary conditions at

the tip and the substrate (red lines) are given in the text. There is no normal flux at symmetry axis and insulating surfaces (blue lines). Simulation space limits are represented by green lines. The flux of species O at the red dot represents a substrate current.....27

Figure 2-8. Simulated concentration profile of species R in the SG–TC mode for a reversible substrate reaction at $E_S = E^0$ and $L = 0.25$. See Figure 1-2 for other parameters.....29

Figure 2-9. Effect of D_R/D_O on i_T-E_S voltammograms (solid lines) for a reversible substrate reaction as obtained at a tip with $RG =$ (a) 1.5 or (b) 10 at $L = 0.25$ in feedback (top) and SG/TC (bottom) modes. Closed circles represent eqs 6 and 8.....30

Figure 2-10. Effect of normalized standard ET rate constant, λ_O' , on substrate voltammograms at $\sigma = 0.01$ as simultaneously obtained with i_T-E_S voltammograms in Figure 2-4.....31

Figure 2-11. Model for an SECM-based thin layer cell.....33

Figure 2-12. Effect of kinetic (α and λ_O') and thermodynamic (E^0) parameters on simulated quasisteady-state i_T-E_S voltammograms. A red curve with $(\alpha, \lambda_O', E^0 \text{ mV}) = (0.5, 2, 0)$ is superimposed with black and blue curves (a) for the feedback mode using $(0.2, 0.25, -30)$ and $(0.8, 10, 8)$, respectively, or (b) for the SG/TC mode using $(0.2, 12.5, -10)$ and $(0.8, 0.25, 30)$, respectively. Dotted lines represent reversible curves for $E^0 = 0 \text{ mV}$38

Figure 2-13. SEM images of pulled, heat-annealed, and FIB-milled Pt tips (from left to right). Scale bars are $2 \mu\text{m}$39

Figure 2-14. An SECM approach curve to a glass substrate (open circles) as obtained for 0.1 mM TCNQ in acetonitrile/0.1 M TBAClO₄ using a 0.42- μm -radius Pt tip with $RG = 2.3$ held at -0.1 V vs Ag. Probe scan rate, 22.5 nm/s. The solid line represents a theoretical approach curve to an insulator ($RG = 2.3$ in ref. 43).....40

Figure 2-15. An SECM approach curve to a 2.5-mm-radius disk Pt electrode (open circles) as obtained for 0.5 mM FcMeOH in 0.2 M NaCl using a 0.48- μm -radius Pt tip with $RG = 1.5$. The tip and the substrate were held at 0.35 and 0 V vs Ag/AgCl, respectively. Probe scan rate, 15.0 nm/s. The solid

line represents a theoretical approach curve to a conductor (eq 11 from ref. 28). The inset shows a scheme for a contact between the flat tip and the highest protrusion at the polished Pt substrate.....41

Figure 2-16. An i_T-E_S voltammogram for 0.1 mM TCNQ in acetonitrile/0.1 M TBAClO₄ with a 2.5-mm-radius disk Pt electrode (red line) as obtained using a 0.51- μ m-radius Pt tip with $RG = 2.0$ in the SG/TC mode. The tip was held at 0.2 V vs Ag. Substrate potential was cycled at 50 mV/s.....42

Figure 3-1. Potential-dependent parts of MHC ET rate constants, $k_{s,t}/k^0$ and $k_{s,b}/k^0$, for reduction and oxidation, respectively, at the substrate as evaluated using Matlab for $\lambda^* =$ (a, a') 20, (b, b') 40, and (c, c') 60 as well as using Mathematica (circles). Dotted lines represent substrate potentials where 99 % of k_{lim} is achieved for $\lambda^* =$ (d, d') 20, (e, e') 40, and (f, f') 60 at 298 K (see eq 9). Dashed lines represent BV kinetics with $\alpha = 0.5$52

Figure 3-2. Simulated i_T-E_S voltammograms based on the MHC formalism with $\lambda^* = 40$ and $\log \lambda'_0 =$ (a, a') 1, (b, b') 0, (c, c') -1, (d, d') -2, (e, e') -3, (f, f') -4, (g, g') -5, and (h, h') -6. Dotted lines correspond to substrate potentials where 99 % of k_{lim} is achieved at 298 K (see eq 9).....55

Figure 3-3. Simulated i_T-E_S voltammograms based on MHC kinetics with $\lambda^* = 40$ (circles) and 60 (solid lines) and BV kinetics with $\alpha = 0.5$ (dotted lines). Dashed lines represent MHC responses with $\lambda^* = 60$ and $\lambda'_0 =$ (b) 7.5×10^{-3} , (c) 5×10^{-4} , and (d) 1×10^{-5}59

Figure 3-4. Simulated i_T-E_S voltammograms based on the MHC formalism (solid lines) with $\lambda^* = 40$ and $\lambda'_0 =$ (a) 1×10^{-3} and (b) 1×10^{-5} . Dashed and dotted lines represent simulated i_T-E_S voltammograms based on BV kinetics with (a) $\lambda'_0 = 5 \times 10^{-2}$ and $\alpha = 0.60$ and 0.40, respectively, and (b) $\lambda'_0 = 9 \times 10^{-3}$ and $\alpha = 0.82$ and 0.18, respectively.....60

Figure 3-5. Theoretical approach curves (solid lines) calculated using eq 15 with the MHC formalism for $\lambda^* = 40$ and $\Lambda =$ (a) 6.7, (b) 2.8, (c) 1.1, and (d) 0.15. Dotted and dashed lines represent purely positive (eq 23) and negative (eq 22) feedback curves, respectively.....64

Figure 3-6. Experimental CV (circles) of $\text{Fe}(\text{CN})_6^{4-}$ at the low defect basal plane surface of HOPG at $v = 10 \text{ V/s}$ read from the original CV in ref. 44 using Engauge Digitizer (<http://digitizer.sourceforge.net/>). Solid and dotted lines represent simulated CVs based on MHC ($\lambda^* = 32$, $k^0 = 5.6 \times 10^{-6} \text{ cm/s}$, and $E^0 = 0.21 \text{ V}$) and BV ($\alpha = 0.5$, $k^0 = 5.0 \times 10^{-7} \text{ cm/s}$, and $E^0 = 0.22 \text{ V}$) kinetics, respectively. The inset shows α_{app} (circles) calculated from eq 19 with the MHC formalism for $\lambda^* =$ (a) 20, (b) 40, and (c) 60 using Mathematica. Linear regions are represented by solid lines with $d\alpha_{\text{app}}/dE = 0.397$, 0.215, and 0.148, respectively, and the intercept at $\alpha_{\text{app}} = 0.5$. Dotted lines in the inset indicate substrate potentials where 99 % of k_{lim} is achieved for $\lambda^* =$ (d, d') 20, (e, e') 40, and (f, f') 60 at 298 K (see eq 9).....66

Figure 3-7. Simulated $i - E$ voltammograms based on the MHC formalism with $\lambda^* = 60$ and $\log =$ (a, a') 1, (b, b') 0, (c, c') -1, (d, d') -2, (e, e') -3, (f, f') -4, (g, g') -5, (h, h') -6, (i, i') -7, (j, j') -8, and (k, k') -9. Dotted lines correspond to substrate potentials where 99 % of k_{lim} is achieved at 298 K (see eq 9).....69

Figure 3-8. Simulated $i - E$ voltammograms based on the MHC formalism with $\lambda^* = 20$ and $\log \lambda'_0 =$ (a, a') 1, (b, b') 0, (c, c') -1, (d, d') -2, (e, e') -3, and (f, f') -4. Dotted lines correspond to substrate potentials where 99 % of k_{lim} is achieved at 298 K (see eq 9).....70

Figure 3-9. Simulated substrate CVs based on (a) MHC formalism with $\lambda^* = 40$ and (b) BV formalism with $\alpha = 0.5$; $\log \lambda'_0 =$ (a) 1, (b) 0, (c) -1, (d) -2, (e) -3, (f) -4, (g) -5, and (h) -6. Curves a and b are reversible and overlap with each other. Dotted lines correspond to substrate potentials where 99 % of k_{lim} is achieved at 298 K (see eq 9).....71

Figure 3-10. Simulated $i_T - E_S$ voltammograms based on BV kinetics with $\alpha = 0.5$ and

$\log \lambda'_0 =$ (a, a') 1, (b, b') 0, (c, c') -1, (d, d') -2, (e, e') -3, (f, f') -4, (g, g') -5, (h, h') -6, (i, i') -7, (j, j') -8, and (k, k') -9.....72

Figure 3-11. Simulated $i_T - E_S$ voltammograms based on the MHC formalism (solid lines) with $\lambda^* = 40$ and $\lambda'_0 =$ (a) 1×10^{-3} and (b) 1×10^{-5} . Dashed and dotted lines represent $i_T - E_S$ voltammograms calculated using eqs 15 and 17 (or 18), respectively.....73

Figure 4-1. SEM images of a borosilicate-sealed Pt UME (A) before and (B) after ESD damage. Parts (C) and (D) show moderately and weakly damaged Pt UMEs, respectively. Scale bars are $1 \mu\text{m}$84

Figure 4-2. SECM approach curve (circles) at an unbiased Au substrate as obtained using the severely ESD-damaged Pt UME (its SEM image is shown in Figure 4-1B) with FcMeOH as a redox mediator. The tip potential was 0.35 V against a Ag/AgCl reference electrode. Tip scan rate, 19 nm/s. The red line represents a theoretical positive-feedback curve for an inlaid disk tip with $RG = 2.5$. The inset shows the CV of 0.5 mM FcMeOH at the damaged UME in 0.1 M KCl. Potential sweep rate, 20 mV/s.....86

Figure 4-3. SEM images of a ~ 110 nm-diameter Pt nanoelectrode (A) before and (B) after ESD damage. Scale bars are $1 \mu\text{m}$. (C) Background-subtracted CV of 0.5 mM FcMeOH in 0.1 M KCl as obtained using the ESD-damaged Pt nanoelectrode. Potential sweep rate, 5 mV/s.....87

Figure 4-4. (A) SEM and (B) X-ray EDS images of a Pt UME after measurement of the 38 CVs of 0.5 mM FcMeOH in 0.1 M KCl. Scale bars are $1 \mu\text{m}$. In the EDS image, orange dots indicate the presence of Pt. (C) Flow of transient current through the Pt tip between ground and a saturated amplifier under an open-loop configuration at the beginning or end of CV measurement. Red arrows indicate current flow while w, r, and c represent working, reference, and Counter electrodes.....88

Figure 4-5. Images of the glass-sealed Pt UMEs stored on conductive foams in (left) plastic and

(right) aluminum cases.....93

Figure 4-6. SEM images of (A and B) a FIB-milled Pt UME with a thick glass sheath and (C and D) an as-pulled Pt UME. The images were taken (A and C) before and (B and D) after ESD damage.

Scale bars are 1 μm94

Figure 4-7. (A) SEM image of the electrochemically damaged Pt UME with locations where (B)

X-ray EDS was taken. Scale bar is 0.5 μm95

Figure 4-8. (A) Some of the 38 CVs of FcMeOH at a glass-sealed Pt UME and (B) limiting currents. Potential sweep rate, 20 mV/s. In part (A), the numbers indicate the order of potential cycles.

The “cell on between runs” function was active (or inactive) before measurement of the CVs shown by red (or black) line and dots in parts (A) and (B), respectively.....97

Figure 4-9. SEM images of the Pt tips electrochemically etched by turning on and off the reference/counter electrode for each of 30 potential cycles between -0.05 and 0.4 V while the tip was (A) connected to or (B) disconnected from a working electrode cable. The tips were immersed in the solution but were not turned on. Scale bars, 1 μm98

Figure 5-1. Scheme of the (A) feedback and (B) SG/TC modes of SECM at the contaminated HOPG surface under a glass-sealed Pt tip. Fc^+ and Fc^{2+} represent FcTMA^+ and FcTMA^{2+} , respectively.....106

Figure 5-2. Experimental (circles) and theoretical (red line) approach curves at an unbiased Au substrate in 0.5 mM FcMeOH and 0.1 M KCl as obtained by using an FIB-milled Pt tip with $\theta = 1.5^\circ$, $a = 0.47$ μm , and $RG = 2.0$. Probe scan rate, 19 nm/s. Tip potential, 0.35 V vs. Ag/AgCl.....109

Figure 5-3. Approach curves at HOPG in 0.3 mM FcTMA^+ and 0.05 M KCl (circles) as fitted to theoretical curves limited by mediator diffusion (red line) or by ET kinetics at the HOPG surface (blue line). Probe scan rate, 49 nm/s. Tip and substrate potentials, 0.5 and 0.1 V vs. Ag/AgCl, respectively. The theoretical curves used $a = 0.48$ μm , $RG = 2.5$111

Figure 5-4. Experimental (solid lines) and theoretical (dotted lines) nanogap voltammograms at

HOPG in 0.3 mM FcTMA⁺ and 0.05 M KCl prepared by water purified through (A) fresh and (B) 17 month old filters. Potential sweep rate, 0.05 V/s. Tip potentials are 0.5 and 0.15 V for the feedback and SG/TC modes, respectively. Theoretical curves used (a, RG) = (A) (0.48 μm , 2.5) and (B) (0.54 μm , 1.8) in addition to $E^{0c} = 0.34$ V (vertical dotted lines) and parameters in Table 1.....112

Figure 5-5. Approach curves at the HOPG surface in 0.3 mM FcTMA⁺ and 0.05 M KCl in UV-treated ultrapure water (A) before and (B) after filtration through an additional activated-carbon filter. Probe scan rate, 49 nm/s. Tip and substrate potentials, 0.50 and 0.15 V vs. Ag/AgCl, respectively. The theoretical curves used (a, RG) = (0.48 μm , 2.5) and (0.48 μm , 2.5) for (A) and (B), respectively.....116

Figure 5-6. Nanogap voltammograms at HOPG in ~1 ppb-TOC water containing 0.3 mM FcTMA⁺ and 0.05 M KCl. Solid and dotted lines represent experimental and theoretical voltammograms, respectively. The parameters used for the theoretical curves are listed in Table 2. Potential sweep rate, 0.05 V/s. Tip potential, 0.50 and 0.15 V in the feedback and SG/CT modes, respectively.....118

Figure 5-7. Scheme of diffusional transport of FcTMA²⁺ (or FcTMA⁺) through a contaminant layer on the HOPG surface in (A) 20 and (B) 2 ppb-TOC water.....121

Figure 5-8. Scheme of FIB milling of glass-sealed Pt tips (A) without and (B) with tilting the Sample stage.....123

Figure 5-9. Experimental (circles) and theoretical (red line) approach curves at an unbiased Au substrate in 0.5 mM FcMeOH and 0.1 M KCl as obtained by FIB-milled Pt tips with (θ, a, RG) = (1.0°, 0.47 μm , 2.1) and (2.0°, 0.47 μm , 1.8) in (A) and (B), respectively. Probe scan rate, 19 nm/s.....123

Figure 5-10. Simulated tip current at the contact of a disk-shaped tip with (A) conductive or (B) insulating substrate tilted by θ_c (see the inset of part A).....124

Figure 5-11. Scheme of a SECM cell with an aqueous solution in the compartment based on glass wall and Teflon cap and base.....125

Figure 5-12. Experimental (circles) and theoretical (solid lines) approach curves at HOPG in 0.3 mM FcTMA⁺ and 0.05 M KCl in water purified by old filters. The theoretical curve used $a = 0.48 \mu\text{m}$ and $RG = 1.8$126

Figure 5-13. A reversible CV of FcTMA⁺ at the HOPG surface in ultrapure water purified by using 17 months old filters for the Nanopure water purifier.....126

Figure 5-14. Tunneling current on nanogap voltammograms at HOPG in 0.3 mM FcTMA⁺ and 0.05 M KCl in ~1 ppb-TOC water. Potential sweep rate, 0.05 V/s.....128

1.0 INTRODUCTION

My PhD work is aimed to develop a methodology to study the electrochemical reactivity of various substrates of scanning electrochemical microscopy using reliable nanofabricated electrodes.

The understanding of potential-dependent electron transfer (ET) kinetics at interfaces is of prime importance both for fundamental and practical reasons. The voltammetry of heterogeneous ET reactions at the electrode of scanning electrochemical microscopy (SECM) is well studied and applied to determine large standard ET rate constants at nanometer sized electrodes. In contrast, measurements of potential-dependent electron transfer processes, taking place at SECM substrates, are significantly limited. To address this issue, I have developed novel methods based on quasi-steady-state voltammetry of rapid ET reactions at macroscopic substrates of scanning electrochemical microscopy and applied this powerful technique to study the electrochemical activity of highly oriented pyrolytic graphite (HOPG).

In the second chapter, I report on a novel method for scanning electrochemical microscopy to enable quasi-steady-state voltammetry of rapid electron transfer (ET) reactions at macroscopic substrates.¹ I demonstrate that the amperometric current at a tip, i_T , in any SECM mode (feedback, substrate generation tip collection SG/TC) maintains a quasi-steady-state during the cyclic sweep of potential (E_S) on the substrate around redox couple's formal potential, as long as the tip is positioned sufficiently close to a macroscopic substrate and a substrate reaction is reversible except under the tip. The resulting plot of i_T versus E_S features the retraceable sigmoidal shape of a quasi-steady state voltammogram although a transient peak- shape voltammogram is obtained simultaneously at the macroscopic substrate. Advantages of monitoring a substrate reaction as a tip current rather than as a substrate current includes the simple measurement and analysis of a quasi-steady-state voltammogram, no charging current at the amperometric tip, high and adjustable mass transport under the tip, and high spatial resolution. Moreover, a kinetic limitation in a quasi-steady-state i_T - E_S voltammogram can be uniquely discriminated from the effect of ohmic potential drop. Importantly, a pair of quasi-steady-state i_T - E_S voltammograms thus obtained in

feedback and SG/TC modes is more informative than each voltammogram and allows for the reliable determination of all transport, thermodynamic, and kinetic parameters. The quasi-steady-state approach developed in this work will find various applications beyond the study of rapid substrate reactions. For instance, the separate assessment of transfer coefficient for cathodic and anodic reactions will be important when the double layer or Marcus-Hush effect is significant.

In the third chapter I report on a generalized theory for nanoscale i_T-E_S voltammetry of substrate reactions with arbitrary reversibility and mechanism under comprehensive experimental conditions including any substrate potential and both SECM modes (feedback and substrate generation tip collection, SG/TC).² The Marcus-Hush-Chidsey (MHC) formalism is employed for heterogeneous outer-sphere ET reactions to enable time-dependent finite element simulations of nanoscale i_T-E_S voltammograms for various kinetic regimes beyond the limit of Butler-Volmer (BV) kinetics. The MHC model is more realistic at large overpotentials where ET rate constants become smaller than predicted by BV kinetics and eventually become potential-independent in contrast to classical Marcus “inverted” behavior. This analytical approach facilitates applications of i_T-E_S voltammetry to non-BV systems.

In chapter 4, I introduce nanofabrication of SECM tips and the way of protection of these tiny electrodes from the damage caused either by electrostatic discharge or electrochemical etching.³ Platinum electrodes sealed in borosilicate or lead doped glass were produced by the laser-based mechanical pulling of glass insulated platinum wire. After pulling, the glass sealed platinum electrodes were heat annealed to make the glass retract from the very tip of electrode. The focused ion-beam (FIB) milling of the heat-annealed tip across the meniscus region of the glass layer was applied to make sharp tip with desirable inner and outer radii. In this work, I show that submicrometer and nanometer sized glass-sealed Pt ultramicroelectrodes (UME) can be easily and unknowingly damaged at the nanoscale to significantly lower their current responses. Such small tips can be damaged by electrostatic discharge (ESD) in air, which can recess the Pt tip and contaminate it with removed Pt and glass. In addition, submicrometer-and nanometer-

size Pt UMEs can be electrochemically etched in electrolyte solution and contaminated with Pt nanoparticles that are removed from the tip at the beginning or end of voltammetric/amperometric measurement when connection of the UMEs to a potentiostat is internally switched on or off, respectively. Recession and contamination owing to electrostatic and electrochemical damage can be a reason why nanoelectrodes often lose a current response or give a low SECM feedback in current– distance curves. I provide information about how to avoid tip damage from ESD or electrochemical etching and maintain reliable and solid performance of the Pt ultramicroelectrode for electrochemical measurements.

The fifth chapter applies of quasi-steady-state voltammetry to study the rapid electron transfer reactions at the macroscopic substrate, such as highly ordered pyrolytic graphite (HOPG), of the scanning electrochemical microscope.⁴ In this chapter, I demonstrate sensitive detection of adsorption of organic impurities from air and ultrapure water to the HOPG surface. The hydrophobic contaminant layer slows down the access of hydrophilic aqueous redox species, (ferrocenylmethyl)trimethyl ammonium (FcTMA^+) to the underlying HOPG surface, thereby yielding a lower standard rate constant, k^0 . The hindering effect of contaminants is stronger for a more charged form of a redox couple (FcTMA^{2+}) so that the electron-transfer reaction of the more hydrophilic form is slower to yield a lower k^0 value. Significantly, the nanogap voltammetry approach is the only electrochemical method that is powerful enough to reveal these behaviors by monitoring the kinetics of both the oxidation and the reduction of a redox couple under high mass transport conditions across a nanometer-wide gap between the HOPG and a Pt tip. In this chapter I also demonstrate reliable performance of the nanofabricated Pt tips by measuring highly positive approach curves on a gold surface and creating a gap with a width of down to 12 nm between Pt tip and Au substrate. This fact indicates that any anomalous behavior of the HOPG electrode is not caused by the surface contamination of a Pt tip.

1.1 REFERENCES

- (1) Nioradze, N.; Jiyeon Kim, J.; Amemiya, A. *Anal. Chem.* **2011**, 83, 828–835
- (2) Amemiya, S.; Nioradze, N.; Santhosh, P.; Deible, M., J. *Anal. Chem.* **2011**, 83, 5928-5935
- (3) Nioradze, N.; Chen, R.; Kim, J.; Shen, M.; Santhosh, P.; Amemiya, S. *Anal. Chem.* **2013**, 85, 6198–6202
- (4) Nioradze, N.; Chen, R.; Kurapati, N.; Khvataeva-Domanov, A.; Mabic, S.; Amemiya, S., submitted to *Anal. Chem.* **2014**

2.0 QUASI-STEADY-STATE VOLTAMMETRY of RAPID ELECTRON TRANSFER REACTIONS AT THE MACROSCOPIC SUBSTRATE OF THE SCANNING ELECTROCHEMICAL MICROSCOPE

This work has been published as N. Nioradze, J. Kim, S. Amemiya, Quasi-Steady-State Voltammetry of Rapid Electron Transfer Reactions at the Macroscopic Substrate of the Scanning Electrochemical Microscope, *Anal. Chem.* **2011** 83, 828–835. The thesis author fabricated electrodes, collected and analyzed experimental data.

2.1 INTRODUCTION

We report on a novel theory and experiment for scanning electrochemical microscopy (SECM) to enable quasi-steady-state voltammetry of rapid electron transfer (ET) reactions at macroscopic substrates. With this powerful approach, the substrate potential is cycled widely across the formal potential of a redox couple while the reactant or product of a substrate reaction is amperometrically detected at the tip in the feedback or substrate generation/tip collection mode, respectively. The plot of tip current versus substrate potential features the retraceable sigmoidal shape of a quasi-steady-state voltammogram although a transient voltammogram is obtained at the macroscopic substrate. Finite element simulations reveal that a short tip-substrate distance and a reversible substrate reaction (except under the tip) are required for quasi-steady-state voltammetry. Advantageously, a pair of quasi-steady-state voltammograms is obtained by employing both operation modes to reliably determine all transport, thermodynamic, and kinetic parameters as confirmed experimentally for rapid ET reactions of ferrocenemethanol and 7,7,8,8-tetracyanoquinodimethane at a Pt substrate with ~ 0.5 μm -radius Pt tips positioned at 90 nm–1 μm distances. Standard ET rate constants of ~ 7 cm/s were obtained for the latter mediator as the largest determined for

substrate reaction by SECM. Various potential applications of quasi-steady-state voltammetry are also proposed.

Scanning electrochemical microscopy (SECM) has evolved as a powerful electroanalytical tool to investigate heterogeneous electron transfer (ET) reactions at electrode/solution interfaces. High versatility and spatial resolution are inherent advantages of SECM against other electrochemical methods.^{1,2} For instance, outer-sphere heterogeneous ET reactions have been studied by SECM to resolve the heterogeneous surface electroactivity of various electrodes and materials. SECM has been also developed to successfully probe inner-sphere heterogeneous ET reactions for the rapid screening of electrocatalysts and photocatalysts in combinatorial arrays. In standard SECM measurements, a disk ultramicroelectrode tip is positioned near a target electrode or material as a substrate to monitor ET kinetics at the local substrate surface under the tip. Typically, tip and substrate electrodes are biased externally to independently control ET rates at the respective electrode/solution interfaces.³ Alternatively, only an SECM tip is biased to drive and monitor a heterogeneous ET reaction at an unbiased electrode⁴ or at an electroactive material on an insulator⁵ as a substrate. Greater understanding of potential-dependent ET kinetics at electrode/solution interfaces is of paramount importance both fundamentally⁶ and practically⁷ and relies on voltammetry.⁸ In fact, voltammetry of heterogeneous ET reactions at the tip of SECM is well established⁹ and has been successfully applied to determine large standard ET rate constants, k^0 , of up to ~ 17 cm/s at nanometer-sized tips.¹⁰ In comparison, the SECM measurement of potential-dependent ET rates at substrates is significantly limited. In the traditional feedback mode of SECM (Figure 2-1a), substrate potential, E_s , is held far from the formal potential, $E^{0'}$, of a redox couple to achieve steady state, where a substrate reaction ($R \rightarrow O + e$) is opposite to a diffusion-limited reaction at the tip ($O + e \rightarrow R$).³ A rapid substrate reaction, however, is accelerated enough at E_s far from $E^{0'}$ to be controlled by mass transport without reaching a kinetic regime,¹¹ thereby limiting the largest k^0 value measured by this approach to 0.42 cm/s¹² so far. In contrast, a rapid substrate reaction is slowed at E_s around $E^{0'}$ to be reversible or even quasireversible. Advantageously, a

quasireversible reaction gives both thermodynamic (E^0) and kinetic (k^0 and transfer coefficient, α) parameters¹³ as demonstrated for quasi reversible substrate reactions by employing the feedback mode^{3,11} (Figure 2-1b) or the substrate generation/tip collection (SG/TC) mode¹⁴ (Figure 2-1c), where the substrate-generated species, R, is detected at the tip at a diffusion-limited rate. The amperometric tip current in either mode, however, is transient with a reversible or quasireversible reaction at a macroscopic substrate, which results in the time-dependent growth of a mediator concentration gradient around the tip-substrate gap. Eventually, a quasi-steady state is reached around the gap with a separation of a few micrometers after a macroscopic substrate is held at a fixed potential for ~ 5 s^{9,15,16} or when the potential of a macroscopic substrate is swept very slowly at 2 mV/s.¹⁷ True steady state (not quasi-steady state) can be achieved in the SG/TC mode by employing an ultramicroelectrode as a substrate,^{14,18-20} which restricts the size of examinable substrates.

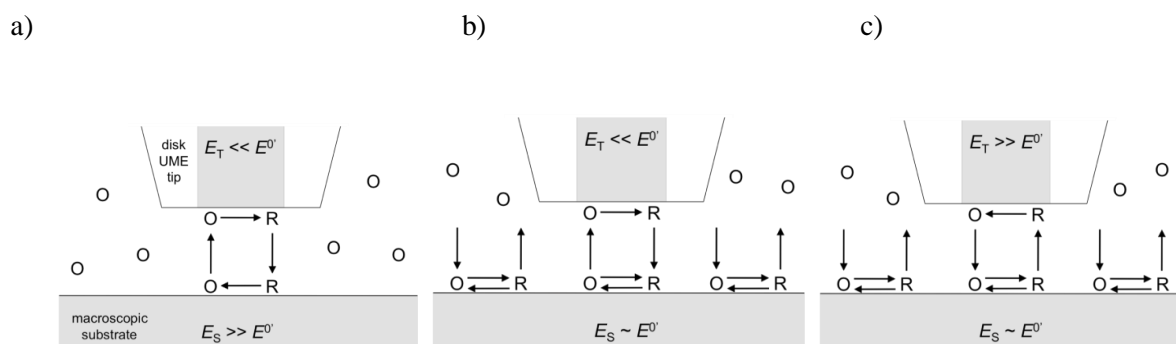


Figure 2-1. Scheme of SECM experiments in the (a) steady-state positive feedback mode, and in (b) feedback and (c) SG/TC modes for a quasireversible substrate reaction under the tip.

Here we report on novel theory and experiment for SECM to enable quasi-steady-state voltammetry of rapid ET reactions at macroscopic substrates in the wide range of substrate potential around E^0 . We demonstrate that the amperometric current at a tip, i_T , in either feedback or SG/TC mode maintains a quasi-steady-state during the cyclic sweep of E_S around E^0 when (i) the tip is positioned sufficiently close to a

macroscopic substrate and (ii) a substrate reaction is reversible except under the tip. The resulting plot of i_T versus E_S features the retraceable sigmoidal shape of a quasi-steady-state voltammogram although a transient peak-shaped voltammogram is obtained simultaneously at the macroscopic substrate. Advantages of monitoring a substrate reaction as a tip current rather than as a substrate current include the simple measurement and analysis of a quasi-steady-state voltammogram, no charging current at the amperometric tip, high and adjustable mass transport under the tip, and high spatial resolution. Moreover, a kinetic limitation in a quasi-steady-state i_T-E_S voltammogram can be unambiguously discriminated from the effect of ohmic potential drop. Importantly, a pair of quasi-steady-state i_T-E_S voltammograms thus obtained in feedback and SG/TC modes is more informative than each voltammogram and allows for the reliable determination of all transport, thermodynamic, and kinetic parameters as recently demonstrated for steady-state nanopipet voltammetry of a common ion at liquid/liquid interfaces.^{21,22} In contrast to the common-ion approach, a pair of quasi-steady-state i_T-E_S voltammograms is obtained simply by moving the tip potential to the feedback or SG/TC region when only one form of a redox couple is initially present in the bulk solution. In the following, we theoretically address requirements for quasi-steady-state i_T-E_S voltammetry by extending the theory of the tip voltammetric counterpart.⁹ We also apply quasi-steady-state i_T-E_S voltammetry to the kinetic study of rapid substrate reactions to obtain large k^0 values of up to ~ 7 cm/s as the largest value determined for a substrate reaction by SECM. Various potential applications of quasi-steady-state i_T-E_S voltammetry are also proposed.

2.2 THEORY

2.2.1 Model

We simulated i_T-E_S voltammograms under various geometric and kinetic conditions by solving standard diffusion problems for SECM (see the Supporting Information). Specifically, axisymmetric, time-dependent diffusion problems (Figure 2-7 in the Supporting Information) were solved by employing COMSOL Multiphysics finite element package (version 3.5a, COMSOL, Inc., Burlington, MA; a

simulation report is attached with the Supporting Information). A current was calculated for the diffusion-limited detection of the original mediator, O, in the feedback mode (Figure 2-1b) or the substrate-generated species, R, in the SG-TC mode (Figure 2-1c) to give a pair of i_T - E_S voltammograms at the same tip-substrate distance. Positive tip (and substrate) currents are based on the reduction of the original mediator so that feedback and SG/TC tip responses appear in the upper and lower panels of the following graphs, respectively. The dimensionless flux of species O at the edge of a macroscopic substrate (red dot in Figure 2-7 in the Supporting Information) represents a substrate current.

A tip current was obtained in the normalized form (eq 9 in the Supporting Information) with respect to a limiting current for species O at the tip in the bulk solution, $i_{T,\infty}$, as given by

$$i_{T,\infty} = 4xnFD_0c_0^*a \quad (1)$$

Where x is expressed by eq 10 in the Supporting Information²³ as a function of RG ($=rg/a$; rg and a are outer and inner tip radii, respectively), $n = 1$ for a one-electron process as considered in this model (eq 14 in the Supporting Information), and D_O and c_0^* are the diffusion coefficient and concentration of the original mediator in the bulk solution, respectively. Features of simulated i_T - E_S voltammograms depend on the following dimensionless parameters

$$L = d / a \quad (\text{dimensionless tip-substrate distance}) \quad (2)$$

$$\sigma = a^2 Fv / 4D_0RT \quad (\text{dimensionless sweep rate for substrate potential}) \quad (3)$$

$$\xi = \sqrt{D_O / D_R} \quad (\text{dimensionless diffusion coefficient ratio}) \quad (4)$$

$$\lambda'_0 = k^0 d / D_O \quad (\text{dimensionless standard ET rate constant}) \quad (5)$$

Where d is the tip-substrate distance, v is the sweep rate for substrate potential, and D_R is the diffusion coefficient of species R in the bulk solution. v

2.2.2 Geometrical Requirements for Quasi-Steady-State Voltammetry

Finite element simulations demonstrate that a quasi-steady-state i_T - E_S voltammogram requires a sufficiently short distance between the tip and the substrate. Figure 2-2 shows the effect of the tip-substrate distance, L , on i_T - E_S voltammograms as simulated for a tip with $RG = 1.5$. In this simulation, a reversible reaction ($\lambda_{O'} = 125$) for a redox couple with identical diffusion coefficients ($\xi=1$) was driven at the whole substrate surface during the cycle sweep of substrate potential at $\sigma = 0.01$. At short tip-substrate distances of $L \leq 0.5$, an i_T - E_S voltammogram in either feedback or SG/TC mode is retraceable on forward and reverse potential sweeps. The retraceable sigmoidal plot of i_T versus E_S corresponds to a quasi-steady-state voltammogram and not a true steady-state voltammogram. In fact, a transient peak-shaped voltammogram results from the plot of substrate current versus substrate potential under the same condition (the inset of Figure 2-2), confirming a time-dependent change in concentration profiles of redox mediators near the macroscopic substrate (Figure 2-8 in the Supporting Information). It is noteworthy that the wide range of substrate potentials in both cathodic and anodic regions far from $E^{0'}$ is applicable under quasi-steady-state conditions to obtain an i_T - E_S voltammogram with the whole sigmoidal shape. In contrast, a true steady state is achieved for a reversible substrate reaction only at $E_S - E^{0'} \geq 120\text{mV}$ on the forward sweep, where no substrate reaction occurs, i.e., zero current in a substrate voltammogram. Subsequently, only limiting currents in the traditional steady-state feedback mode³ are observed in this limited potential range.

A quasi-steady-state tip current is obtained at a sufficiently short tip-substrate distance, where concentrations of redox mediators around the tip uniformly and instantaneously follow their concentrations at the substrate surface (Figure 2-8 in the Supporting Information), i.e., the tip sees substrate surface concentrations as bulk concentrations. In addition, substrate surface concentrations must quickly reach quasi-steady-state at different substrate potentials to give a retraceable i_T - E_S voltammogram. This requirement is satisfied under local equilibrium conditions at the substrate/solution interface with a reversible substrate reaction (see below).

In contrast to the short distance region, concentrations of redox mediators at longer distances from a macroscopic substrate do not instantaneously follow their substrate surface concentrations (Figure 2-8 in the Supporting Information). Therefore, longer tip-substrate distances of $L \geq 1.0$ result in unretraceable i_T - E_S voltammograms under the same condition (Figure 2-2) where a reverse wave shifts toward more extreme potentials with respect to the corresponding forward wave. We also found that the current at a tip with smaller RG reaches quasi-steady state more quickly under practical conditions with $D_O \neq D_R$ ($\xi \neq 1$). For instance, a tip with $RG = 1.5$ gives quasi-steady-state voltammograms at $\sigma = 0.01$ and $L = 0.25$ in a range of $0.5D_O < D_R < 2D_O$ that is typical for aqueous and organic electrolyte solutions (Figure 2-3a).

As σ increases to 0.1 (Figure 2-9a in the Supporting Information), an i_T - E_S voltammogram with $D_O \neq D_R$ slightly deviates from a quasi-steady-state behavior. The requirement of $\sigma \leq 0.01$ for quasi-steady-state corresponds to $a \leq 3.3 \mu\text{m}$ in eq 3 with $v = 50 \text{ mV/s}$ and $D_O = 5 \times 10^{-6} \text{ cm}^2/\text{s}$, thereby corresponding to

$d \leq 0.81 \mu\text{m}$ at $L = 0.25$. Micrometer- or submicrometer-radius tips with $RG = 1.5$ can readily approach to such short distances from a substrate (see the Results and Discussion).

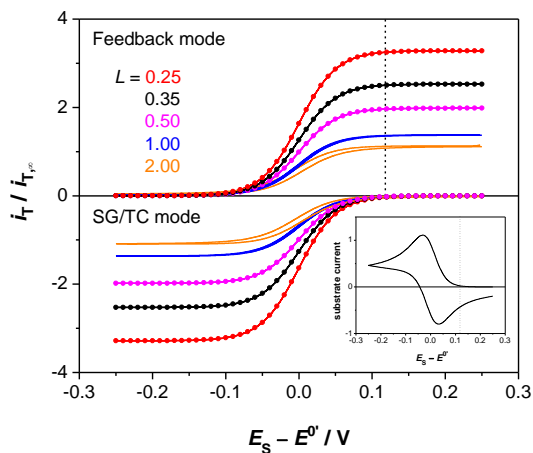


Figure 2-2. Reversible i_T - E_S voltammograms simulated for various tip-substrate distances (solid curves). Closed circles represent eqs 6 and 8. The inset shows a simultaneously simulated reversible voltammogram at the substrate

In comparison, significantly smaller σ (≤ 0.001) is required for obtaining nearly quasi-steady-state voltammograms at a tip with $RG = 10$ under the same condition with $D_O \neq D_R$ (see Figure 2-3b and Figure 2-9b in the Supporting Information for $\sigma = 0.01$ and 0.001 , respectively). The requirements of $a \leq 1.0 \mu\text{m}$ for $\sigma \leq 0.001$ and $d \leq 0.25 \mu\text{m}$ for $L=0.25$ are difficult to be achieved using conventional tips with large RG (for instance, as in ref 24, $a = \sim 0.5 \mu\text{m}$ and $RG = \sim 7$ give $L > 0.7$). Overall, an SECM tip with small RG significantly facilitates the quasi-steady-state measurement of an i_T - E_S voltammogram under practical conditions.

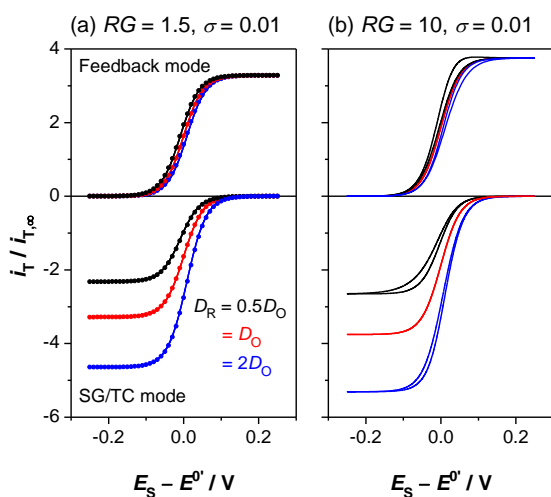


Figure 2-3. Effect of D_R/D_O on i_T - E_S voltammograms simulated for $L = 0.25$ (solid curves). Closed circles represent 6 and 8

This RG effect with $\xi \neq 1$ is explained as follows. When oxidized and reduced forms of a redox couple have unequal diffusion coefficients, transient concentration profiles of these redox mediators in the tip-substrate gap relax toward the final quasi-steady-state profiles by their radial diffusion between the gap and the bulk solution as extensively simulated for tip chronoamperometry in both positive feedback¹⁵ and SG-TC¹⁶ modes. A shorter radial diffusion distance under a thinner insulating sheath surrounding the tip results in quicker attainment of quasi-steady state.

2.2.3 Requirement of Reversible Substrate Reaction for Quasi-Steady-State Voltammetry

A dimensionless rate constant, $\lambda_{O'}$, was varied in finite element simulations to find that a substrate reaction must be reversible except under the tip to obtain the whole i_T-E_S voltammogram under quasi-steady-state conditions. Figure 2-4 shows i_T-E_S voltammograms for a tip with $RG = 1.5$ as simulated for various $\lambda_{O'}$ values with $R = 0.5$, $\sigma = 0.01$, $L = 0.25$, and $\xi = 1$. Quasi-steady-state i_T-E_S voltammograms are obtained only with $\lambda_{O'} \geq 0.3$ when substrate voltammograms are reversible or nearly reversible at this dimensionless scan rate (Figure 2-12 in the Supporting Information). This requirement of a reversible reaction at the exterior substrate surface for quasi-steady-state i_T-E_S voltammetry is explained as follows. When a substrate reaction is reversible, substrate surface concentrations of redox mediators are always equilibrated with time-dependent substrate potentials. In fact, the convolution principle confirms that equilibrium concentrations of species O and R at the exterior substrate surface uniquely correspond to substrate potentials independent of the rate and direction of the potential sweep (eqs 23a and 23b in the Supporting Information). Eventually, equilibrium surface concentrations immediately control mediator concentrations around a narrow tip-substrate gap (Figure 2-8 in the Supporting Information), where local quasi-steady state is maintained during the cyclic sweep of substrate potential.

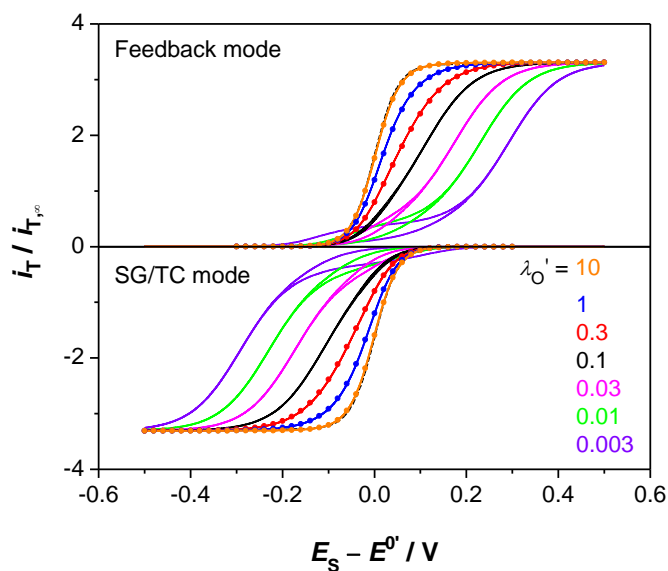


Figure 2-4. Effect of normalized standard ET rate constant, λ'_O , on simulated i_T-E_S voltammograms (solid curves). Simulated reversible curves are represented by black dotted lines, which nearly overlap with curves for $\lambda'_O = 10$. Closed circles represent eqs 6 and 8.

In contrast, i_T-E_S voltammograms for kinetically limited substrate reactions at the exterior surface ($\lambda'_O \leq 0.1$ in Figure 2-4) are partially untraceable around their foot. These voltammograms with slow substrate kinetics become retraceable at more extreme potentials, where a substrate reaction is diffusion-limited (for more detailed discussion, see the Supporting Information). These partially untraceable i_T-E_S voltammograms are beyond the scope of this work and will be addressed in future work.

2.2.4 Analytical Expressions for Quasi-Steady-State Voltammograms

Quasi-steady-state i_T-E_S voltammograms can be expressed using analytical equations as obtained by extending the theory of the tip voltammetric counterpart⁹ (see the Supporting Information for their

derivations). When the original mediator O is detected at the tip in the feedback mode (Figure 2-1b), the quasi-steady-state tip current in the normalized form, $I_{T,O}^{FB}(E_S, L)$, is given by

$$I_{T,O}^{FB}(E_S, L) = \frac{\pi}{2xL(2/\theta_S + 2\theta_S^{\alpha-1}/\lambda'_O + \xi^2 + 1)} + \frac{\xi\theta_S}{\xi\theta_S + 1} \left[I_{T,d}(L) - \frac{\pi}{2xL(\xi^2 + 1)} \right] \quad (6)$$

$$\text{With } \theta_S = \exp[F(E_S - E^{0'})/RT] \quad (7)$$

where $I_{T,d}(L)$ is the normalized tip current under diffusion-limited positive feedback conditions. In addition, the normalized quasi-steady-state tip current in the SG/TC mode, $I_{T,R}^{ST}(E_S, L)$, is given by

$$I_{T,R}^{ST}(E_S, L) = - \left\{ \frac{\pi}{2xL(2\xi^2\theta_S + 2\theta_S^\alpha/\lambda'_O + \xi^2 + 1)} + \frac{1}{\xi\theta_S + 1} \left[\frac{I_{T,d}(L)}{\xi} - \frac{\pi}{2xL(\xi^2 + 1)} \right] \right\} \quad (8)$$

Equations 6 and 8 are valid when a solution initially contains only species O as assumed in the Theory section. Alternatively, eqs 44 and 46 in the Supporting Information must be used for feedback and SG/TC modes, respectively, when only species R is initially present in the bulk solution.

These analytical equations agree well (<1% error) with simulation results for both reversible (Figures 2-2, 2-3a, and Figure 2-11 in the Supporting Information) and quasireversible ($\lambda'_O \geq 0.3$ in Figure 2-4) conditions under the tip with $RG = 1.5$ or 10 when $D_O = D_R$. These equations, however, are less accurate with $D_O \neq D_R$, where the assumption of local mass balance in the tip-substrate gap (eqs 28 and 48 in the Supporting Information) is not exact. With $D_O \neq D_R$, the total concentration of redox molecules in the gap at quasi-steady-state is different from their initial total concentration because of their radial diffusion

between the gap and the bulk solution.^{15,16} Nevertheless, errors in eqs 6 and 8 increase only up to ~4% for reversible redox couples with $D_R = 0.5D_O$ or $2D_O$ (Figure 2-3a and Figure 2-9b in the Supporting Information).

2.2.5 Kinetic Analysis of a Pair of Quasi-Steady-State Voltammograms

As recently discussed in detail for steady-state voltammetry,^{21,22} a pair of quasi-steady-state i_T-E_S voltammograms in both operation modes allows for the reliable determination of thermodynamic (E^0) and kinetic (R and k^0) parameters even when a substrate reaction under a tip is nearly reversible. The shape of a nearly reversible quasi-steady-state voltammogram depends on kinetic parameters too weak to reliably determine both kinetic and thermodynamic parameters. For instance, an i_T-E_S voltammogram with a relatively large λ_O' value of 2 and a normal R value of 0.5 nearly overlaps with an i_T-E_S voltammogram with an anomalously large (or small) R value of 0.8 (or 0.2) by adjusting λ_O' and E^0 accordingly for either feedback or SG/TC mode (Figures 2-12a and 2-12b in the Supporting Information, respectively). Different combinations of λ_O' and E^0 , however, must be used for curves in different operation modes to be superimposed with each other. This result indicates that the unique combination of thermodynamic and kinetic parameters can be obtained from a pair of quasi-steady-state i_T-E_S voltammograms for a nearly reversible substrate reaction under a tip.

It should be noted that the kinetic analysis of a pair of quasi-steady-state i_T-E_S voltammograms requires $I_{T,d}(L)$ and ξ values as obtained from the corresponding pair of limiting currents in feedback and SG/TC modes. The respective limiting currents are equivalent to $I_{T,d}(L)$ in eq 6 and $-I_{T,d}(L)/\xi$ in eq8 when the solution initially contains only species O. In contrast, a limiting current of $-\xi I_{T,d}(L)$ is given by eq 46 in the Supporting Information for the SG/TC mode when only species R is initially present in the bulk solution. Noticeably, the knowledge of ξ is also required for the determination of E^0 from the position of a reversible quasi-steady-state i_T-E_S voltammogram (see Figure 2-3 for the ξ -dependent shift of i_T-E_S voltammograms).

2.3 EXPERIMENTAL SECTION

2.3.1 Chemicals

Ferrocenemethanol (FcMeOH, Aldrich, Milwaukee, WI) was recrystallized twice from hexane prior to use. All aqueous solutions were prepared with 18.3 M Ω cm deionized water (Nanopure, Barnstead, Dubuque, IA). 7,7,8,8-Tetracyano-quinodimethane (TCNQ, Aldrich) was recrystallized twice from acetone. Tetrabutylammonium (TBA) perchlorate (Aldrich) was used as organic supporting electrolytes in anhydrous acetonitrile (Aldrich).

2.3.2 SECM Measurement

Approximately 0.5 μ m-radius Pt tips with a small RG of 1.5-2.5 (Figure 2-13c in the Supporting Information) were fabricated and characterized as described in the Supporting Information. A tip was brought within a short distance of <1 μ m from a Pt substrate by monitoring the tip current in the positive feedback mode and was positioned at a fixed distance from the substrate during i_T - E_S voltammetry using a commercial SECM instrument with inchworm motors (CHI 900, CH Instruments, Austin, TX). An SECM stage was placed on a vibration isolation platform (model 63-533, TMC, Peabody, MA). The bipotentiostat of another SECM instrument (CHI 910B, CH Instruments) was employed to simultaneously monitor tip and substrate currents during the cyclic sweep of substrate potential. Positive currents at the tip and substrate correspond to the oxidation of 0.5 mM FcMeOH in 0.2 M NaCl or the reduction of 0.1 mM TCNQ in 0.1M TBAClO₄. Subsequently, feedback and SG/TC tip responses for both mediators consistently appear in the upper and lower panels of the following graphs, respectively. A 2.5 mm-radius Pt disk electrode (Pine Research Instrumentation, Raleigh, NC) was employed as a substrate. The Pt substrate was polished with alumina paste slurry (0.05 μ m) on microcloth pads (Buehler, Lake Bluff, IL) and sonicated three times in deionized water for 5 min, in H₂SO₄ containing 3% H₂Cr₂O₇ for 10 min, and again in deionized water for 15 min. A 125 μ m-radius Ag wire (99.9%, Aldrich) was coated with AgCl to serve as an aqueous reference

electrode. Inner and outer compartments of a double junction nonaqueous Ag reference electrode (BASi, West Lafayette, IN) were filled with acetonitrile solutions of 0.1 M TBAClO₄ with and without 0.01 M AgNO₃, respectively.

2.4 RESULTS AND DISCUSSION

2.4.1 Reversible ET Reaction of FcMeOH

A 0.48 μ m-radius Pt tip with RG = 1.5 was employed to obtain quasi-steady-state i_T - E_S voltammograms for FcMeOH at a 2.5 mm-radius Pt substrate (solid curves in Figure 2-5). Either in the feedback or SG/TC mode, a sigmoidal i_T - E_S voltammogram on the forward sweep of substrate potential completely overlaps with that on the reverse sweep. In contrast, simultaneously measured voltammograms at the macroscopic substrate are peak-shaped and transient (the inset of Figure 2-5). These results confirm that the retraceable i_T - E_S voltammograms were mainly obtained under quasi-steady-state conditions.

True steady state was achieved only at $E_S < \sim 40$ mV on the forward sweep of substrate potential when the oxidation of FcMeOH at the substrate was negligible as estimated from the substrate voltammogram. Only limiting currents were obtained under the true steady-state conditions as employed for the traditional feedback mode,³ where the range of applicable substrate potentials is significantly limited. Noticeably, FcMeOH gives a reversible voltammogram at the macroscopic Pt substrate (with a peak separation of 60 mV in the inset of Figure 2-5), which is required for obtaining a quasi-steady-state i_T - E_S voltammogram.

A pair of limiting currents in feedback and SG/TC modes at the same tip-substrate distance was analyzed to determine all transport parameters (d , D_{FcMeOH^+} , and D_{FcMeOH}). An enhanced limiting current in the feedback mode is equivalent to a total positive feedback current of $I_{T,d}(L)$ in eq 44 in the Supporting Information, thereby yielding tip-substrate distances of $L=0.19$ - 2.4 in eq 11 in the Supporting Information ($d=91$ nm- 1.1μ m for $a=0.48\mu$ m). Interestingly, quasi-steady-state voltammograms were obtained at a long

tip-substrate distance of $L = 2.4$ with the minimal tip-current enhancement of $\sim 10\%$. This result confirms that quasi-steady-state does not require a feedback distance and is achieved at tip-substrate distances where concentrations of redox mediators uniformly and instantaneously follow their equilibrium substrate surface concentrations (Figure 2-8 in the Supporting Information). Moreover, limiting currents of $-\xi IT_d(L)$ in the SG/TC mode (eq 46 in the Supporting Information) at different tip-substrate distances give consistent ξ values of $(D_{\text{FcMeOH}^+}/D_{\text{FcMeOH}})^{1/2} = 1.06 \pm 0.02$, thereby yielding $D_{\text{FcMeOH}^+} = 8.8 \times 10^{-6} \text{ cm}^2/\text{s}$ for $D_{\text{FcMeOH}} = 7.8 \times 10^{-6} \text{ cm}^2/\text{s}$ as determined from $i_{T,\infty}$ at well characterized tips using eq 45 in the Supporting Information.

All quasi-steady-state i_T-E_S voltammograms thus obtained for FcMeOH are indistinguishable from theoretical voltammograms for reversible ET reactions at the whole surface of a macroscopic substrate (closed circles in Figure 2-5), thereby yielding consistent $E^{0'}$ values of 157.8 (0.5 mV vs Ag/AgCl). These $E^{0'}$ values agree with half-wave potentials of reversible tip voltammograms in the bulk solution and also with averages of anodic and cathodic peak potentials of reversible substrate voltammograms. The half-wave potentials and the averages of peak potentials, however, are based on the convolution of $E^{0'}$ and ξ and are equivalent to $E^{0'}$ only when $\xi=1$. In contrast, $E^{0'}$ and ξ are separately obtainable from positions and limiting currents of a pair of quasi-steady-state i_T-E_S voltammograms, respectively. This feature of quasi-steady-state i_T-E_S voltammetry will be useful for the study of redox couples with unequal diffusion coefficients, e.g., in room temperature ionic liquids.²⁵

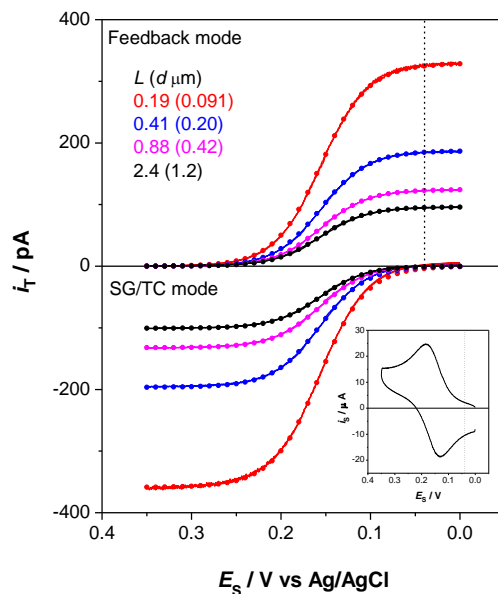


Figure 2-5. Quasi-steady-state i_T - E_S voltammograms for 0.5 mM FcMeOH (solid lines) as obtained using a 0.48- μm -radius Pt tip with $RG = 1.5$ in feedback (top) and SG/TC (bottom) modes at various tip-substrate distances. The tip was held at 0.35 or 0.05 V vs Ag/AgCl for feedback or SG/TC modes, respectively. The substrate potential was cycled at 50 mV/s. Closed circles represent reversible theoretical voltammograms (eqs 28 and 30 supporting Information). The inset shows a reversible voltammogram as simultaneously measured at the substrate.

Reversible i_T - E_S voltammograms for FcMeOH are consistent with a large k^0 value of $\sim 7\text{cm/s}$ for this mediator at nanometer- sized Pt tips (25-290 nm radius) as determined by tip voltammetry,¹⁰ where the tip potential was swept to oxidize FcMeOH while the substrate potential was fixed for the diffusion-limited reduction of FcMeOH⁺. This k^0 value is 7-8 times larger than the largest mass transfer coefficients of $D_{\text{FcMeOH}^+}/d=0.95\text{cm/s}$ and $D_{\text{FcMeOH}}/d=0.84\text{cm/s}$ at the shortest tip-substrate distance of 91 nm in Figure 2-5, which is larger than or barely comparable to tip-substrate distances of 18-122 nm required for obtaining kinetically limited nanotip voltammograms for FcMeOH.¹⁰ Nevertheless, it should be mentioned that our quasi-steady-state approach moves the range of applicable substrate potentials within (120 mV from E^0 , which is comparable to the range of tip potentials required for slowing the nearly reversible oxidation of

FcMeOH at the Pt nanotips to determine the large k^0 value. Overall, these comparisons indicate that the upper limit of measurable k^0 values at substrates by quasi-steady-state i_T - E_S voltammetry should be comparable to that at tips by tip voltammetry when the same tip-substrate distance is employed.

2.4.2 Nearly Reversible ET Reaction of TCNQ

The one-electron reduction of TCNQ at a 2.5 mm-radius Pt electrode was investigated using a 0.53 μm -radius Pt tip with $\text{RG} = 1.9$ (solid curves in Figure 2-6).

Quasi-steady-state i_T - E_S voltammograms thus obtained for TCNQ changed from reversible to nearly reversible as the tip was positioned closer to the Pt substrate, where tip-substrate distances were determined from limiting currents of $I_{T,d}(L)$ in the feedback mode using eq 11 in the Supporting Information. At relatively large distances of $L = 1.9$ and 0.92 , the i_T - E_S voltammograms fit well with the corresponding reversible voltammograms (closed circles) as obtained from eqs 6 and 8 to give an E^0 value of -88mV vs Ag. In contrast, the i_T - E_S voltammograms at shorter tip-substrate distances of $L=0.30$ and 0.18 are broader and shifted toward more extreme potentials in comparison to reversible voltammograms (dotted curves). The experimental voltammograms in both feedback and SG/TC modes fit very well with theoretical curves for nearly reversible substrate reactions under the tip (closed circles), thereby yielding a normal R value of 0.5 and $\lambda_o' = 4.0$ and 2.5 at the respective distances in addition to the same E^0 value of -88 mV . The λ_o' values correspond to consistent k^0 values of 5.1 and 5.3 cm/s , respectively, which supports the reliability of this kinetic study. In contrast to reversible FcMeOH (Figure 2-5) with $k^0 \approx 7\text{cm/s}$, 10 similar k^0 values for TCNQ result in a kinetic limitation at similar tip-substrate distances because of larger diffusion coefficients of TCNQ and its anion radical in acetonitrile as determined from limiting currents of $-I_{T,d}(L)/\xi$ in the SG/TC mode (eq 8). Specifically, $\xi = 1.13 \pm 0.05$ thus obtained is comparable to a literature value of 1.039 and gives $D_{\text{TCNQ}^-} = 1.6 \times 10^{-5}\text{ cm}^2/\text{s}$ for $D_{\text{TCNQ}} = 2.0 \times 10^{-5}\text{ cm}^2/\text{s}$ as determined from $i_{T,\infty}$ at well characterized tips using eq 1.

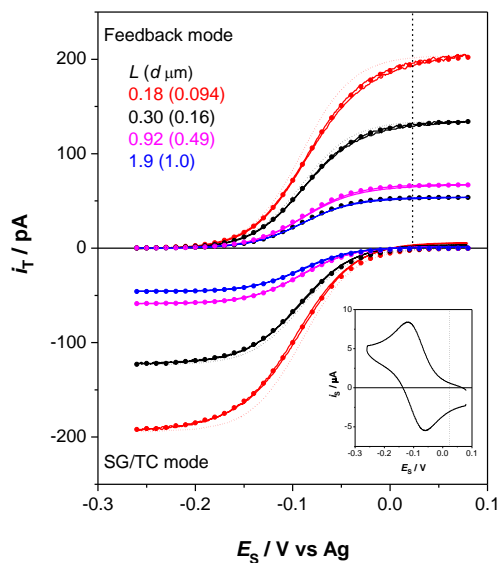


Figure 2-6. Quasi-steady-state i_T - E_S voltammograms for TCNQ (solid lines) The tip was held at -0.235 or 0 V vs Ag for feedback or SG/TC modes, respectively. Substrate potential was cycled at 50 mV/s. The inset shows a reversible voltammogram simultaneously measured at the substrate (with a peak separation of 61mV).

We carried out quasi-steady-state i_T - E_S voltammetry for TCNQ at various lateral tip positions over the Pt substrate to obtain k^0 values in the range of 3-7 cm/s (data not shown), which quantitatively reveals the heterogeneous electroactivity of the macroscopic Pt surface. These k^0 values are larger than values of ~ 1 cm/s for TCNQ at Pt nanotips as determined by tip voltammetry.¹⁰ We ascribe this difference to a more rough surface of a polished Pt macroelectrode,²⁶ which is confirmed by the direct contact of smooth Pt tips with Pt protrusions at the substrate surface (Figure 2-15 in the Supporting Information) and also by the observation of numerous spikes based on tunneling current between the tip and the protrusions near the contact distance (Figure 2-16 in the Supporting Information). Overall, the k^0 values as obtained by i_T - E_S voltammetry in this work are effective values. These effective values are still much smaller than a value of $\sim 2 \times 10^3$ cm/s as expected from the Marcus theory for TCNQ with a large self-exchange rate constant of $4 \times 10^9 \text{ M}^{-1} \text{ s}^{-1}$.¹⁰

The k^0 values of up to ~ 7 cm/s thus determined for TCNQ by quasi-steady-state i_T - E_S voltammetry are much larger than a k^0 value of 0.42 cm/s for the H_2 oxidation at a Pt substrate,¹² which had been the largest k^0 value determined for a substrate reaction by SECM. In comparison to the previous SECM studies of substrate ET kinetics, sharper tips with smaller a and RG were employed in this work to achieve shorter tip-substrate distances and, subsequently, higher mass-transport conditions. In addition, the determination of the large k^0 values for TCNQ requires quasi-steady-state conditions. The intrinsically rapid reaction of TCNQ at a Pt substrate must be slowed at ES within ± 120 mV from $E^{0'}$ to observe a kinetic limitation (Figure 2-6). In contrast, only limiting currents are obtained for this rapid mediator under traditional steady-state feedback conditions, where substrate potential must be positive enough with respect to $E^{0'}$ to avoid significant TCNQ reduction at the substrate ($E_S - E^{0'} > 120$ mV on the forward potential sweep as estimated from the reversible substrate voltammogram in Figure 2-6). Moreover, the reliability of this kinetic measurement is improved significantly by employing both feedback and SG/TC modes under quasi-steady-state conditions. Finite element simulations of nearly reversible substrate reactions under the tip, e.g., $\lambda_{O'} = 2.0$ in Figure 2-12 in the Supporting Information, indicate that a pair of quasi-steady-state voltammograms is essential for reliable determination of both thermodynamic and kinetic parameters for TCNQ with large $\lambda_{O'}$ (= 4.0 and 2.5 in Figure 2-6).

Finally, a good overlap between forward and reverse waves of a kinetically limited i_T - E_S voltammogram for TCNQ confirms the negligible contribution of an iR drop between substrate and reference electrodes to substrate potential. In contrast to the kinetic effect, the iR drop effect depends on the direction of the cyclic sweep of substrate potential to shift forward and reverse waves toward opposite directions, thereby yielding an unretraceable voltammogram under quasi-steady-state conditions. In fact, retraceable i_T - E_S voltammograms were obtained for TCNQ at a low concentration of 0.1 mM, which reduces the iR drop. Importantly, an i_T - E_S voltammogram at this low concentration is well-defined because an amperometric tip current is free from a charging current and is enhanced by the efficient mass transport

of redox mediators between the tip and the substrate. In contrast, a charging current is significant in the corresponding substrate voltammogram (the inset of Figure 2-6). Overall, no information from a substrate voltammogram is needed for the analysis of a quasi-steady-state i_T - E_S voltammogram while the respective voltammograms provide global and local information about the electroactivity of the Pt substrate.

2.5 CONCLUSIONS

We developed a novel SECM approach to enable quasi-steady-state voltammetry of rapid ET reactions at macroscopic substrates. The wide range of substrate potentials is applicable under quasi-steady-state conditions to cover both cathodic and anodic regions far from E^0 , one of which reaches the limited range of substrate potentials employed in the traditional steady-state feedback mode.³ Subsequently, a pair of quasi-steady-state i_T - E_S voltammograms is obtained in both feedback and SG/TC modes to enable the separate and reliable determination of all transport (D_O , D_R , and d), thermodynamic (E^0), and kinetic (R and k^0) parameters. This quasi-steady-state approach requires a short tip-substrate distance and a reversible reaction at a macroscopic substrate except under the tip to be intrinsically suitable for the kinetic study of a rapid substrate reaction, which can be slowed at substrate potentials around E^0 and probed both cathodically and anodically under high mass-transport conditions. In fact, k^0 values of up to ~ 7 cm/s for TCNQ as obtained by this approach are the largest determined for a substrate reaction by SECM. A larger k^0 value will be determinable by narrowing the tip-substrate gap, which requires a smoother substrate or a smaller tip as demonstrated for the tip voltammetric counterpart.¹⁰

The quasi-steady-state approach developed in this work will find various applications beyond the study of rapid substrate reactions. For instance, the separate assessment of transfer coefficient for cathodic and anodic reactions will be important when the double layer or Marcus-Hush effect is significant.⁶ A voltammetric SG/TC measurement with a macroscopic substrate at quasi-steady state is complementary to the true steady-state counterpart with an ultramicroelectrode substrate as recently developed for the SG/TC

study of short-lived intermediates.^{19,20} Quasi-steady-state i_T - E_s voltammetry at different lateral tip positions results in multiple images of a heterogeneous substrate surface based on topography (d), intrinsic electroactivity (k^0), and ET mechanism (α). Moreover, a tip can be scanned at just outside of the feedback distances from a substrate at quasi-steady state to enable the feedback-free, direct imaging of the “surface concentration” of a target species generated or consumed at a substrate electrode. The imaging of an electrode surface concentration contrasts to the SG/TC imaging of a mediator concentration far from a substrate¹⁸ and, interestingly, rather resembles the surface plasmon resonance imaging of electrode reactions,²⁷ which probes concentrations of both forms of a redox couple at the electrode surface.

2.6 SUPPORTING INFORMATION

2.6.1 Finite Element Simulation

The SECM diffusion problem defined in the Theory section was solved in a dimensionless form by employing the finite element method. A tip current, i_T , was normalized with respect to a limiting current at an inlaid disk tip in the bulk solution, $i_{T,\infty}$, to obtain a dimensionless tip current, I_T , as

$$I_T = \frac{i_T}{i_{T,\infty}} = \frac{2\pi}{x} \int_0^1 R \left[\frac{\partial C_o(R, L, \tau)}{\partial Z} \right] dR \quad (9)$$

The x values simulated for different RG values at $L = 50$ agree with theoretical values as given by²⁸

$$x = 1 + 0.639 \left[1 - \frac{2}{\pi} \arctan\left(\frac{1}{RG}\right) \right] - 0.186 \left\{ 1 - \left[\frac{2}{\pi} \arctan\left(\frac{1}{RG}\right) \right]^2 \right\} \quad (10)$$

The reliability of our simulation results was further confirmed by the good agreement of simulated

$I_{T,d}(L)$ values with theoretical values as given by²⁸

$$I_{T,d}(L) = \alpha(RG) + \frac{\pi}{4x \arctan(L)} + \left[1 - \alpha(RG) - \frac{1}{2x} \right] \frac{2}{\pi} \arctan(L) \quad (11)$$

With

$$\alpha(RG) = \ln 2 + \ln 2 \left[1 - \frac{2}{\pi} \arctan\left(\frac{1}{RG}\right) \right] - \ln 2 \left\{ 1 - \left[\frac{2}{\pi} \arctan\left(\frac{1}{RG}\right) \right]^2 \right\} \quad (12)$$

Model. A cylindrical coordinate was employed (Figure 2-7) to define time-dependent axisymmetric diffusion equations for oxidized and reduced forms of a redox couple, O and R, respectively, as

$$\frac{\partial C_O(R, Z, \tau)}{\partial \tau} = 0.25 \left[\frac{\partial^2 C_O(R, Z, \tau)}{\partial R^2} + \frac{1}{R} \frac{\partial C_O(R, Z, \tau)}{\partial R} + \frac{\partial^2 C_O(R, Z, \tau)}{\partial Z^2} \right] \quad (13a)$$

$$\frac{\partial C_R(R, Z, \tau)}{\partial \tau} = \frac{0.25}{\xi^2} \left[\frac{\partial^2 C_R(R, Z, \tau)}{\partial R^2} + \frac{1}{R} \frac{\partial C_R(R, Z, \tau)}{\partial R} + \frac{\partial^2 C_R(R, Z, \tau)}{\partial Z^2} \right] \quad (13b)$$

where $c_O(r, z, t)$ and $c_R(r, z, t)$ are concentrations of the respective redox mediators in the solution.

Initially, only species O is present in the bulk solution, i.e., $c_O(r, z, 0) = c_O^*$ (the bulk concentration of O) and $c_R(r, z, 0) = 0$.

The cyclic sweep of substrate potential at a constant rate, v , is initiated at $t = 0$ from $E_S \gg E^{0'}$ toward the cathodic direction to drive a one-electron process at a macroscopic substrate as



where $k_{f,s}$ and $k_{b,s}$ are first-order heterogeneous rate constants. The rate constants are given by the Butler–Volmer relation as²⁹

$$k_{f,s} k^0 \exp[-\alpha F(E_s - E^{0'})/RT] \tag{15a}$$

$$k_{b,s} = k^0 \exp[(1 - \alpha)F(E_s - E^{0'})/RT] \tag{15b}$$

The use of the Butler–Volmer model is justified in this work, which is mainly concerned about the simple substrate reactions that give a normal α value of 0.5 and reach a diffusion limitation at substrate potentials where the Marcus model may be more appropriate, $|E - E^{0'}| \geq 0.15\text{V}$ for a redox couple with a reorganization energy of 1 eV.³⁰ Boundary conditions at insulating walls surrounding a tip and simulation space limits are given in Figure 2-7.

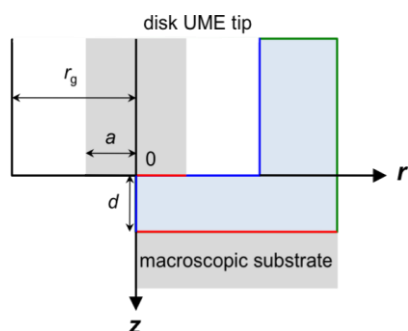


Figure 2-7. Geometry of a SECM diffusion problem in the cylindrical coordinate. The simulation space (light blue) is surrounded by seven boundaries (red, blue, and green lines). Boundary conditions at the tip and the substrate (red lines) are given in the text. There is no normal flux at symmetry axis and insulating surfaces (blue lines).

Simulation space limits are represented by green lines. The flux of species O at the red dot represents a substrate current.

Attached is the simulation result of a quasi-steady-state i_T-E_S voltammogram in the SG/TC mode for a nearly reversible substrate reaction under the tip ($\lambda'_0 = 2$) as obtained using the following dimensionless parameters.

$$R = r/a \quad (16)$$

$$Z = z/a \quad (17)$$

$$\tau = 4D_{O^*}t/a^2 \quad (18)$$

$$C_O(R, Z, \tau) = c_O(r, z, t)/C_O^* \quad (19a)$$

$$C_R(R, Z, \tau) = c_R(r, z, t)/C_O^* \quad (19b)$$

Diffusion equations for species O and R in the solution phase (eqs 1a and 1b, respectively) were also expressed in dimensionless forms as

$$\frac{\partial C_O(R, Z, \tau)}{\partial \tau} = 0.25 \left[\frac{\partial^2 C_O(R, Z, \tau)}{\partial R^2} + \frac{1}{R} \frac{\partial C_O(R, Z, \tau)}{\partial R} + \frac{\partial^2 C_O(R, Z, \tau)}{\partial Z^2} \right] \quad (20a)$$

$$\frac{\partial C_R(R, Z, \tau)}{\partial \tau} = \frac{0.25}{\xi^2} \left[\frac{\partial^2 C_R(R, Z, \tau)}{\partial R^2} + \frac{1}{R} \frac{\partial C_R(R, Z, \tau)}{\partial R} + \frac{\partial^2 C_R(R, Z, \tau)}{\partial Z^2} \right] \quad (20b)$$

Dimensionless diffusion coefficients of 0.25 and $0.25/\xi^2$ were used in eqs S10 and S11, respectively. Substrate boundary conditions were given by

$$0.25 \left[\frac{\partial C_O(R, Z, \tau)}{\partial Z} \right]_{Z=L} = \frac{0.25K}{\theta_S^\alpha} [\theta_S C_R(R, Z, \tau) - C_O(R, Z, \tau)] \quad (21a)$$

$$\frac{0.25}{\xi^2} \left[\frac{\partial C_R(R, Z, \tau)}{\partial Z} \right]_{Z=L} = \frac{0.25K}{\theta_S^{\alpha-1}} \left[\frac{C_O(R, Z, \tau)}{\theta_S} - C_R(R, Z, \tau) \right] \quad (21b)$$

with

$$K = k^0 a / D_O \quad (22)$$

In the attached simulation result, $K = 8$ at $L = 0.25$ is equivalent to $\lambda'_0 = 2$. Other boundary conditions and initial conditions were also defined in dimensionless forms. The overall simulation space is large enough and does not control simulation results.

2.6.2 Mediator Concentrations under Quasi-Steady-State Conditions.

Figure 2-8 shows the simulated concentration profile of a substrate-generated species, R, detected at the tip at a diffusionlimited rate in the SG/TC mode.

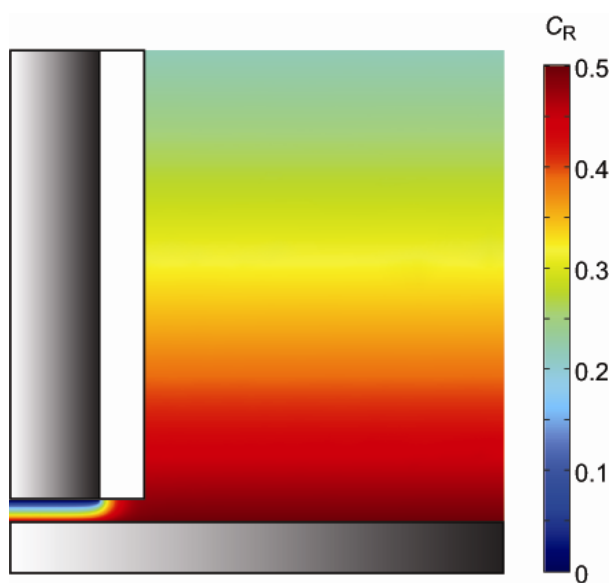


Figure 2-8. Simulated concentration profile of species R in the SG–TC mode for a reversible substrate reaction at $E_S = E^0$ and $L = 0.25$. See Figure 2-2 for other parameters.

2.6.3 Effect of Unequal Diffusion Coefficients on i_T – E_S Voltammograms.

Various D_R values were employed to examine their effect on σ values required for obtaining quasi-steady-state i_T – E_S voltammograms at a tip with $RG = 1.5$ or 10 (Figure 2-9) under the identical condition as employed for the simulation of voltammograms in Figure 2-3. With $D_R \neq D_O$, a voltammogram at a tip with $RG = 1.5$ is slightly untraceable at $\sigma = 0.1$ to give a little larger limiting current in the SG/TC mode than

expected from eq 8 (Figure 2-9a). With $D_R \neq D_O$, a much smaller σ value of 0.001 is required for obtaining nearly retraceable voltammograms at a conventional tip with $RG = 10$ to fit well with eqs 6 and 8 (Figure 2-9b)

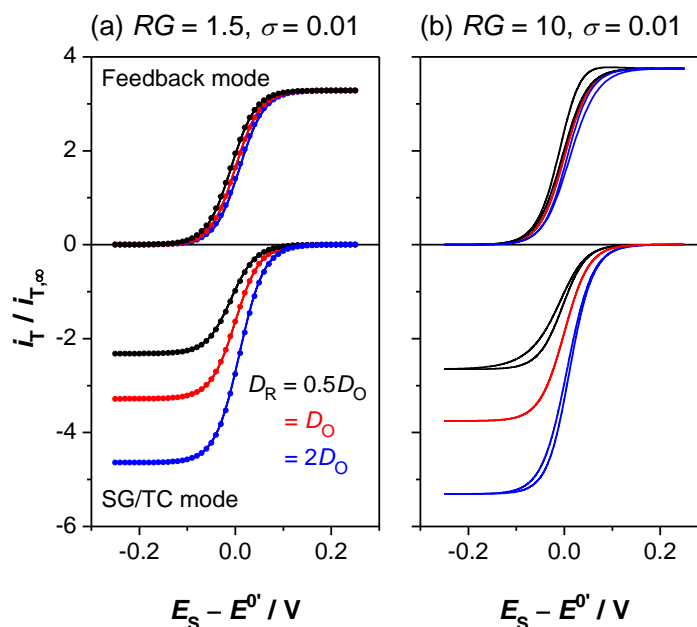


Figure 2-9. Effect of D_R/D_O on i_T-E_S voltammograms (solid lines) for a reversible substrate reaction as obtained at a tip with $RG =$ (a) 1.5 or (b) 10 at $L = 0.25$ in feedback (top) and SG/TC (bottom) modes. Closed circles represent eqs 6 and 8.

2.6.4 Reversibility of Substrate Voltammograms.

Figure 2-10 shows substrate voltammograms with various λ_O' values as obtained simultaneously with i_T-E_S voltammograms in Figure 4. At $\sigma = 0.01$, substrate voltammograms are reversible or nearly reversible with $\lambda_O' \geq 0.3$ while a smaller λ_O' value results in a less reversible substrate voltammogram.

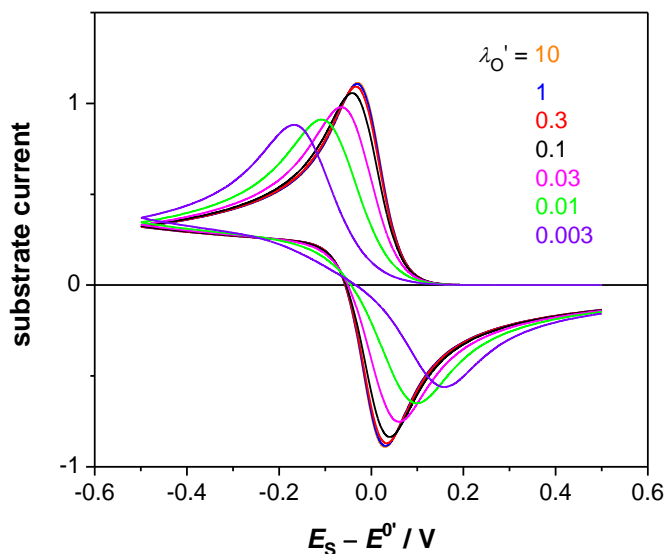


Figure 2-10. Effect of normalized standard ET rate constant, $\lambda_{O'}$, on substrate voltammograms at $\sigma = 0.01$ as simultaneously obtained with $i_T - E_S$ voltammograms in Figure 2-4.

2.6.5 Equilibrium Mediator Concentrations at the Surface of a Macroscopic Substrate.

When a heterogeneous ET reaction is reversible at the surface of a macroscopic substrate except under the tip, mediator concentrations at the exterior surface, $c_{O,S}^{ex}$ and $c_{R,S}^{ex}$, for species O and R, respectively, are equilibrated with and uniquely correspond to substrate potentials as given by

$$c_{O,S}^{ex} = c_O^* \xi \theta_S / (\xi \theta_S + 1) \quad (23a)$$

$$c_{R,S}^{ex} = c_O^* \xi \theta_S / (\xi \theta_S + 1) \quad (23b)$$

These equations were derived as follows using the convolution principle.³¹ When a solution initially contains only species O, mediator concentrations at the exterior surface are given by

$$c_{O,S}^{\text{ex}} = c_0^* - \frac{I_S(t)}{FA\sqrt{D_O}} \quad (24a)$$

$$c_{R,S}^{\text{ex}} = \frac{I_S(t)}{FA\sqrt{D_R}} \quad (24b)$$

where $I_S(t)$ represents the semi-integral of substrate current. In addition, the Nernst equation is given by

$$E_S = E^{0'} - \frac{RT}{nF} \ln \frac{c_{R,S}^{\text{ex}}}{c_{O,S}^{\text{ex}}} \quad (25)$$

The combination of eq 25 with eqs 24a and 24b gives eqs 23a and 23b.

2.6.6 Kinetically Limited i_T - E_S Voltammograms with Partially Retractable Regions

In Figure 2-4, i_T - E_S voltammograms for non-reversible substrate reactions with $\lambda_{O'} \leq 0.1$ at $\sigma = 0.01$ are retraceable at $E_S \gg E_{pa}$ and $E_S \ll E_{pc}$, where E_{pa} and E_{pc} are anodic and cathodic peak potentials of the corresponding substrate voltammograms. Under these diffusion-limited conditions at the exterior substrate surface, the corresponding concentrations of redox mediators are constant and identical on both forward and reverse potential sweeps. Conspicuously, i_T - E_S voltammograms in the feedback mode are retraceable at $E_S \gg E_{pa}$, where substrate surface concentrations are unchanging from the corresponding bulk concentrations, i.e., and , on both forward and reverse potential sweeps to give the identical tip current under steady-state and quasi-steady-state conditions, respectively. The different conditions are associated with zero and finite substrate currents at $E_S \gg E_{pa}$ on the respective potential sweeps. Moreover, constant surface concentrations of and are maintained at $E_S \ll E_{pc}$. Therefore, the identical quasi-steady-state tip current is obtained in the SG/TC mode at $E_S \ll E_{pc}$ on forward and reverse potential sweeps although the corresponding substrate currents are different.

2.6.7 Analytical Equations for Quasi-Steady-State i_T - E_s Voltammograms

In this section, eqs 6 and 8 are derived as analytical equations for quasi-steady-state i_T - E_s voltammograms in feedback and SG/TC modes, respectively, by extending the theory of quasi-steady-state tip voltammetry.³²

Model and Assumptions. Analytical equations for quasi-steady-state tip currents at different substrate potentials were obtained by extending a model for an SECM-based thin layer cell (TLC).³² In the extended model (Figure 2-11), the surface of a macroscopic substrate was divided into the TLC region under the tip and its exterior region. Different surface concentrations of redox mediators in the respective regions are given by $c_{O,S}^{TLC}$ and $c_{O,S}^{ex}$ for species O and by $c_{R,S}^{TLC}$ and $c_{R,S}^{ex}$ for species R. These distinct surface concentrations are due to a higher mass-transport condition at the region under the TLC than at the exterior region. Accordingly, a quasireversible reaction was assumed at the TLC region of the substrate surface. At the same time, a reversible substrate reaction at the exterior surface was assumed as a requirement for obtaining the whole i_T - E_s voltammogram under quasi-steady-state conditions (see eqs 23a and 23b). In contrast, surface concentrations of redox mediators at the disk tip, and for species O and R, respectively, were assumed to be uniform.³³

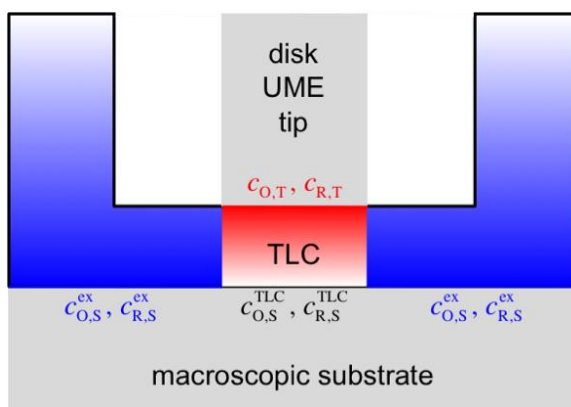


Figure 2-11. Model for an SECM-based thin layer cell.

The tip current in this leaky thin layer cell, i_T , is approximated as the sum of the feedback (or SG/TC) current from the substrate under the TLC, i_{TLC} , and the direct current from the bulk solution, i_{bulk} , thereby yielding³⁴

$$i_T(E_S, L) = i_{TLC}(E_S, L) + i_{bulk}(E_S, L) \quad (26)$$

The feedback (or SG/TC) current depends on the kinetics of a quasireversible ET reaction at the substrate surface under the tip and is included in the flux balance across the TLC between the tip and the substrate as

$$\frac{i_{TLC}(E_S, L)}{\pi a^2 n F} = -\left(k_{f,S} c_{O,S}^{TLC} - k_{b,S} c_{R,S}^{TLC}\right) = -\frac{D_O(c_{O,T} - c_{O,S}^{TLC})}{d} = -\frac{D_R(c_{R,S}^{TLC} - c_{R,T})}{d} \quad (27)$$

Mass balance in the TLC is also approximated to

$$c_{O,T} + c_{R,T} + c_{O,S}^{TLC} + c_{R,S}^{TLC} = 2c_O^* \quad (28)$$

where the equality is satisfied only with $D_O = D_R$.^{35,36} The direct current from the bulk solution at quasisteady state is determined by the tip–substrate distance and the concentration of a tip-detected species at the exterior surface of a macroscopic substrate (eq 23a or 23b for the feedback or SG/TC mode, respectively). This surface concentration is seen by a tip as a bulk concentration at short tip–substrate distances (Figure 2-8).

Feedback Mode. Eq 6 was obtained for quasi-steady-state i_T – E_S voltammograms in the feedback mode as follows. The diffusion-limited reduction of species O at the tip corresponds to in eqs 27 and 28, which gives

$$i_{TLC}(E_S, L) = \frac{2\pi n F D_O c_O^* a}{L(2/\theta_S + 2\theta_S^{\alpha-1} / \lambda'_O + \xi^2 + 1)} \quad (29)$$

The direct tip current from the bulk solution at quasi-steady state is related to the concentration of the original species O at the exterior surface of the substrate (eq 23a) as

$$i_{\text{bulk}}(E_S, L) = \frac{4xnFD_O c_O^* a \xi \theta_S}{\xi \theta_S + 1} f(L) \quad (30)$$

where $f(L)$ represents the dependence of i_{bulk} on the tip–substrate distance. The combination of eq 26

with eqs 29 and 30 gives the tip current in the feedback mode, $i_{\text{T,O}}^{\text{FB}}(E_S, L)$, as

$$i_{\text{T,O}}^{\text{FB}}(E_S, L) = 4xnFD_O c_O^* a \left[\frac{\pi}{2xL(2/\theta_S + 2\theta_S^{\alpha-1}/\lambda'_O + \xi^2 + 1)} + \frac{\xi \theta_S}{\xi \theta_S + 1} f(L) \right] \quad (31)$$

Moreover, $f(L)$ is obtained from the diffusion-limited positive-feedback current at a tip, $I_{\text{T,d}}(L)$, using eq 9 with $E_S \gg E^{0'}$ as

$$I_{\text{T,d}}(L) = \frac{i_{\text{T,O}}^{\text{FB}}(E_S \gg E^{0'}, L)}{4xnFD_O c_O^* a} \quad (32)$$

where eq 31 gives

$$i_{\text{T,O}}^{\text{FB}}(E_S \gg E^{0'}, L) = 4xnFD_O c_O^* a \left[\frac{\pi}{2xL(\xi^2 + 1)} + f(L) \right] \quad (33)$$

The combination of eq 32 with eq 33 results in

$$f(L) = I_{\text{T,d}}(L) - \frac{\pi}{2xL(\xi^2 + 1)} \quad (34)$$

Therefore, eq 31 is equivalent to

$$i_{\text{T,O}}^{\text{FB}}(E_S, L) = 4xnFD_O c_O^* a \left\{ \frac{\pi}{2xL(2/\theta_S + 2\theta_S^{\alpha-1}/\lambda'_O + \xi^2 + 1)} + \frac{\xi \theta_S}{\xi \theta_S + 1} \left[I_{\text{T,d}}(L) - \frac{\pi}{2xL(\xi^2 + 1)} \right] \right\} \quad (35)$$

The normalization of 35 with respect to $i_{\text{T},\infty}$ (eq 1) gives eq 6.

SG/TC Mode. Eq 8 was derived for the SG/TC mode. When the substrate-generated species, R, is oxidized at the tip at a diffusion-limited rate, i.e., $c_{\text{R,T}} = 0$, the combination of eq 27 with eq 28 yields

$$i_{\text{TLC}}(E_S, L) = -\frac{2\pi anFD_R \xi^2 c_O^*}{L(2\xi^2 \theta_S + 2\theta_S^\alpha / \lambda'_O + \xi^2 + 1)} \quad (36)$$

Also, the direct current from the bulk solution is given by the concentration of species R at the exterior substrate surface (eq 23b) as

$$i_{\text{bulk}}(E_S, L) = -\frac{4xnFD_R \xi c_O^* a}{\xi \theta_S + 1} f(L) \quad (37)$$

The combination of eq 32 with eqs 36 and 37 gives the tip current in the SG/TC mode, $i_{\text{T,R}}^{\text{ST}}(E_S, L)$, as

$$i_{\text{T,R}}^{\text{ST}}(E_S, L) = -4xnFD_R c_O^* a \xi \left[\frac{\pi \xi}{2xL(2\xi^2 \theta_S + 2\theta_S^\alpha / \lambda'_O + \xi^2 + 1)} + \frac{f(L)}{\xi \theta_S + 1} \right] \quad (38)$$

Now, $f(L)$ is obtained as follows. When the substrate potential is negative enough at $E_S \ll E^{0'}$, eq 38 is equivalent to the diffusion-limited tip current as

$$i_{\text{T,R}}^{\text{ST}}(E_S \ll E^{0'}, L) = -4xnFD_R c_O^* a \xi \left[\frac{\pi \xi}{2xL(\xi^2 + 1)} + f(L) \right] \quad (39)$$

This diffusion-limited tip current is also obtained from eq 9 as

$$i_{\text{T,R}}^{\text{ST}}(E_S \ll E^{0'}, L) = -4xnFD_R \xi c_O^* a I_{\text{T,d}}(L) \quad (40)$$

where eq 23b with $E_S \ll E^{0'}$ gives

$$c_{\text{R,S}}^{\text{ex}} = \xi c_O^* \quad (41)$$

The comparison of eq 39 with eq 40 yields

$$f(L) = I_{\text{T,d}}(L) - \frac{\pi \xi}{2xL(\xi^2 + 1)} \quad (42)$$

Overall, eq 38 is equivalent to

$$i_{T,R}^{ST}(E_S, L) = -4xnFD_O c_O^* a \left\{ \frac{\pi}{2xL(2\xi^2\theta_s + 2\theta_s^\alpha / \lambda'_O + \xi^2 + 1)} + \frac{1}{\xi\theta_s + 1} \left[\frac{I_{T,d}(L)}{\xi} - \frac{\pi}{2xL(\xi^2 + 1)} \right] \right\} \quad (43)$$

Eq 8 is obtained by the normalization of eq 43 with respect to $i_{T,\infty}$ (eq 1).

2.6.8 Analytical Equations for Quasi-Steady-State i_T - E_S Voltammograms for Species R (FcMeOH).

Quasi-steady-state i_T - E_S voltammograms for FcMeOH were analyzed using analytical equations as obtained when only species R is initially present in the solution. The corresponding tip current based on the oxidation of species R in the feedback mode is given as

$$I_{T,R}^{FB}(E_S, L) = \xi^2 \left\{ \frac{\pi}{2xL(2\xi^2\theta_s + 2\theta_s^\alpha / \lambda'_O + \xi^2 + 1)} + \frac{1}{\xi\theta_s + 1} \left[\frac{I_{T,d}(L)}{\xi^2} - \frac{\pi}{2xL(\xi^2 + 1)} \right] \right\} \quad (44)$$

Which is normalized with respect to

$$i_{T,\infty} = 4xnFD_R c_R^* a \quad (45)$$

where c_R^* is the bulk concentration of species R. In the SG/TC mode, the normalized tip current based on the reduction of species O is equivalent to

$$I_{T,O}^{ST}(E_S, L) = -\xi^2 \left\{ \frac{\pi}{2xL(2/\theta_s + 2\theta_s^{\alpha-1} / \lambda'_O + \xi^2 + 1)} + \frac{\xi\theta_s}{\xi\theta_s + 1} \left[\frac{I_{T,d}(L)}{\xi} - \frac{\pi}{2xL(\xi^2 + 1)} \right] \right\} \quad (46)$$

Derivations of eqs 34 and 46 are very similar to those of eqs 6 and 8 (see above) except for the following points. In the former case, a positive current is based on the oxidation of the original mediator R. Accordingly, the signs in the flux balance in the TLC are chosen to yield

$$\frac{i_{TLC}(E_S, L)}{\pi a^2 nF} = k_{f,S} c_{O,S}^{TLC} - k_{b,S} c_{R,S}^{TLC} = \frac{D_O(c_{O,T} - c_{O,S}^{TLC})}{d} = \frac{D_R(c_{R,S}^{TLC} - c_{R,T})}{d} \quad (47)$$

The bulk concentration of species R is used for mass balance in the TLC as

$$c_{O,T} + c_{R,T} + c_{O,S}^{\text{TLC}} + c_{R,S}^{\text{TLC}} = 2c_R^* \quad (48)$$

where the equality is satisfied only with $D_O = D_R$.^{35,36} Concentrations of redox mediators at the exterior surface of a substrate are given by the convolution principle as³¹

$$c_{O,S}^{\text{ex}} = \frac{\theta_S c_R^*}{\xi \theta_S + 1} \quad (49)$$

$$c_{R,S}^{\text{ex}} = \frac{c_R^*}{\xi \theta_S + 1} \quad (50)$$

2.6.9 Effects of Thermodynamic and Kinetic Parameters

Figure 2-11 show that a pair of quasisteady- state i_T-E_S voltammograms for a nearly reversible substrate reaction with $(\alpha, \lambda_O', E^0 \text{ mV}) = (0.5, 2, 0)$ is uniquely defined. Voltammograms with different combinations of the kinetic and thermodynamic parameters can be superimposed with each other either for the feedback or SG/TC mode. Voltammograms in the other operation mode, however, are very different.

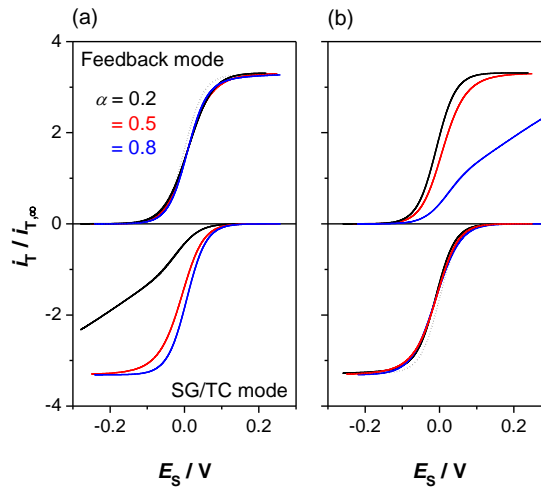


Figure 2-12. Effect of kinetic (α and λ_O') and thermodynamic (E^0) parameters on simulated quasisteady- state i_T-E_S voltammograms. A red curve with $(\alpha, \lambda_O', E^0 \text{ mV}) = (0.5, 2, 0)$ is superimposed with black and blue curves (a)

for the feedback mode using (0.2, 0.25, -30) and (0.8, 10, 8), respectively, or (b) for the SG/TC mode using (0.2, 12.5, -10) and (0.8, 0.25, 30), respectively. Dotted lines represent reversible curves for $E^0 = 0$ mV.

2.6.10 Tip Fabrication and characterization.

Approximately 0.5- μm -radius Pt tips with small RG of 1.5–2.5 were fabricated as reported elsewhere.³⁷ A Pb-doped glass tube (o.d./i.d. = 1.5 mm/1.1 mm, 10 cm in length, Corning 8161, Warner Instruments, Hamden, CT) was used for tip insulation because of its high resistivity and slightly higher thermal expansion coefficient than that of Pt.³⁸ The laser-based mechanical pulling of a glass-insulated Pt tip^{39,40} typically gave $a = \sim 0.1$ μm and $RG = \sim 5$ (Figure 2-13a). The glass layer surrounding the pulled tip was heated over the Pt-coil heater of a microforge (MF-900, Narishige, Tokyo, Japan) to melt and retract from the tip (Figure 2-13b). The exposition of the Pt tip from the thin glass layer was monitored in real time by using the high-magnification optical microscope of the microforge ($\times 35$ objective lens and $\times 15$ eyepiece). The focused ion-beam (FIB) milling⁴¹ of the heatannealed tip across the meniscus region of the glass layer gave a sharp tip with desirable inner and outer radii (Figure 2-13c).

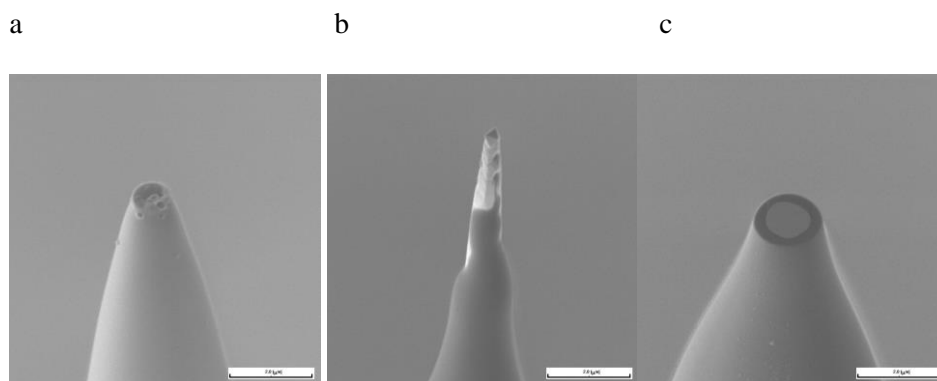


Figure 2-13. SEM images of pulled, heat-annealed, and FIB-milled Pt tips (from left to right). Scale bars are 2 μm .

The inner and outer radii of each FIB-milled tip were estimated from its scanning electron microscopic and focused ion beam images⁴¹ Due to slightly imperfect disk geometries of the metal and

surrounding glass (Figure 2-13c), apparent radii of a tip vary within $\pm 10\%$ from average radii. The average values are consistent with values determined from approach curves to an insulating substrate,⁴² which agree very well with the corresponding theoretical curve⁴³ (Figure 2-14). Noticeably, a contact between the tip and the smooth glass substrate occurs at a very short distance of $L < 0.1$ ($L = 0.075$ and $d = 31\text{nm}$ for $RG = 2.3$ in Figure 2-14). This result confirms that a FIB-milled tip is smooth and perpendicularly aligned with respect to the tip length.⁴¹

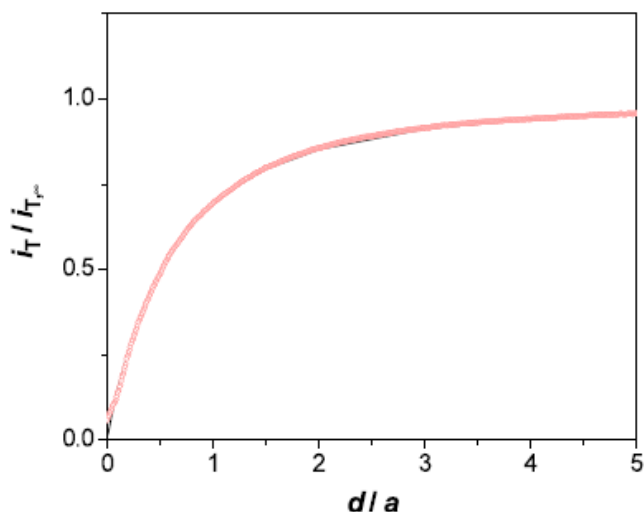


Figure 2-14. An SECM approach curve to a glass substrate (open circles) as obtained for 0.1 mM TCNQ in acetonitrile/0.1 M TBAClO₄ using a 0.42- μm -radius Pt tip with $RG = 2.3$ held at -0.1 V vs Ag. Probe scan rate, 22.5 nm/s. The solid line represents a theoretical approach curve to an insulator ($RG = 2.3$ in ref. 43).

Interestingly, a positive approach curve with a sharp FIB-milled tip to a Pt substrate shows a dramatic and quick increase in the tip current due to their direct contact at a short tip-substrate distance ($L = 0.18$ and $d = 86$ nm in Figure 2-15). This result indicates a direct contact between the flat Pt tip and the highest protrusion from the macroscopic Pt surface under the tip (the inset of Figure 2-15), indicating the significant roughness of the substrate surface. Nevertheless, the excellent fit between experimental and

theoretical approach curves for the Pt substrate demonstrates that the most region of the substrate surface under the tip is flat enough to give well defined tip–substrate distances.

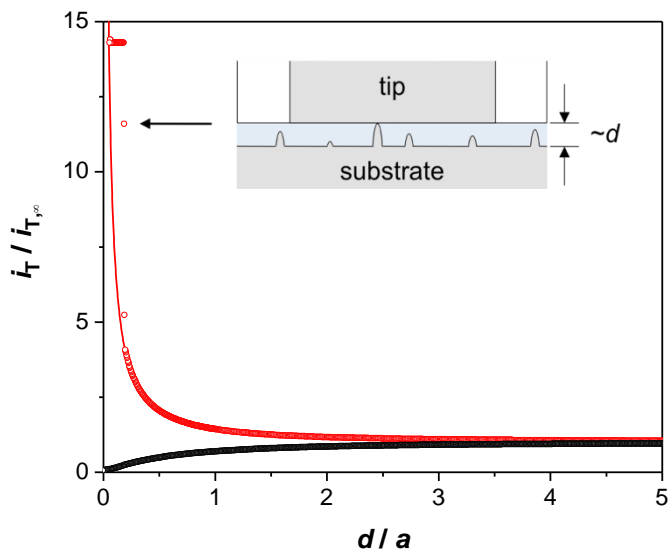


Figure 2-15. An SECM approach curve to a 2.5-mm-radius disk Pt electrode (open circles) as obtained for 0.5 mM FcMeOH in 0.2 M NaCl using a 0.48- μm -radius Pt tip with $RG = 1.5$. The tip and the substrate were held at 0.35 and 0 V vs Ag/AgCl, respectively. Probe scan rate, 15.0 nm/s. The solid line represents a theoretical approach curve to a conductor (eq 11 from ref. 28). The inset shows a scheme for a contact between the flat tip and the highest protrusion at the polished Pt substrate.

2.6.11 Observation of Current Spikes in i_T - E_S Voltammograms.

Numerous current spikes were observed for FcMeOH and TCNQ in feedback and SG/TC modes when a tip was positioned very close to a contact distance. For instance, $d = \sim 80$ nm is obtained from the limiting current in the i_T - E_S voltammogram for TCNQ in the SG/TC mode as shown in Figure 2-16. In this example, current spikes were observed on the reverse sweep of substrate potential. Some of the spikes at $-0.1 \text{ V} < E_S < 0.0 \text{ V}$ exceeded a measurable limit of -1.2 nA. We ascribe these current spikes to high tunneling current between the flat Pt tip and the protrusions at the rough Pt substrate (the inset of Figure 2-

15). Similar current spikes were observed in a tip voltammogram at a roughly polished Pt nanotip positioned above a smooth Au substrate.³⁹

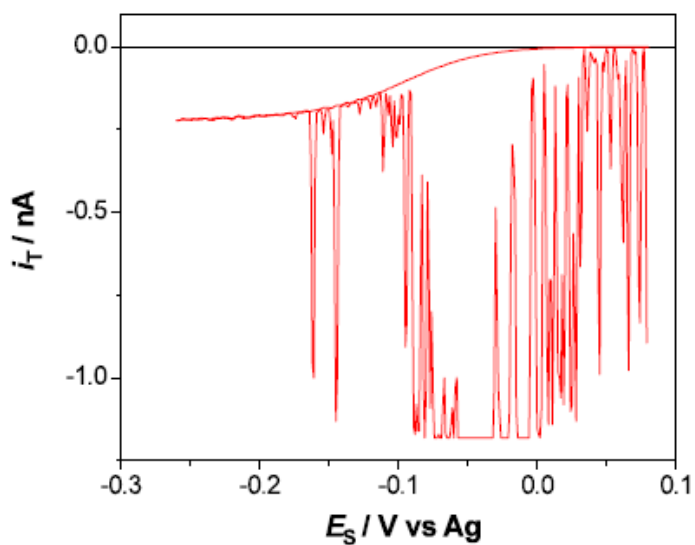


Figure 2-16. An i_T - E_S voltammogram for 0.1 mM TCNQ in acetonitrile/0.1 M TBAClO₄ with a 2.5- mm-radius disk Pt electrode (red line) as obtained using a 0.51- μ m-radius Pt tip with $RG = 2.0$ in the SG/TC mode. The tip was held at 0.2 V vs Ag. Substrate potential was cycled at 50 mV/s.

ACKNOWLEDGMENTS

The supports of this work by the National Institutes of Health (Grant GM073439) and the Petersen Institute of NanoScience and Engineering at the University of Pittsburgh are gratefully acknowledged.

2.7 REFERENCES

- (1) Bard, A. J.; Mirkin, M. V., Eds. Scanning Electrochemical Microscopy; Marcel Dekker: New York, 2001.
- (2) Amemiya, S.; Bard, A. J.; Fan, F.-R. F.; Mirkin, M. V.; Unwin, P. R. *Ann. Rev. Anal. Chem.* 2008, 1, 95.
- (3) Bard, A. J.; Mirkin, M. V.; Unwin, P. R.; Wipf, D. O. *J. Phys. Chem.* 1992, 96, 1861.
- (4) Xiong, H.; Guo, J.; Amemiya, S. *Anal. Chem.* 2007, 79, 2735.
- (5) Kim, J.; Xiong, H.; Hofmann, M.; Kong, J.; Amemiya, S. *Anal. Chem.* 2010, 82, 1605.
- (6) Feldberg, S. W. *Anal. Chem.* 2010, 82, 5176.
- (7) Garsany, Y.; Baturina, O. A.; Swider-Lyons, K. E.; Kocha, S. S. *Anal. Chem.* 2010, 82, 6321.
- (8) Bard, A. J.; Zoski, C. G. *Anal. Chem.* 2000, 72, 346A.
- (9) Zoski, C. G.; Luman, C. R.; Fernandez, J. L.; Bard, A. J. *Anal. Chem.* 2007, 79, 4957.
- (10) Sun, P.; Mirkin, M. V. *Anal. Chem.* 2006, 78, 6526.
- (11) Zoski, C. G.; Aguilar, J. C.; Bard, A. J. *Anal. Chem.* 2003, 75, 2959.
- (12) Zhou, J.; Zu, Y.; Bard, A. J. *J. Electroanal. Chem.* 2000, 491, 22.
- (13) Mirkin, M. V.; Bard, A. J. *Anal. Chem.* 1992, 64, 2293.
- (14) Dumitrescu, I.; Dudin, P. V.; Edgeworth, J. P.; Macpherson, J. V.; Unwin, P. R. *J. Phys. Chem. C* 2010, 114, 2633.
- (15) Martin, R. D.; Unwin, P. R. *J. Electroanal. Chem.* 1997, 439, 123.
- (16) Martin, R. D.; Unwin, P. R. *Anal. Chem.* 1998, 70, 276.
- (17) Engstrom, R. C.; Weber, M.; Wunder, D. J.; Burgess, R.; Winkquist, S. *Anal. Chem.* 1986, 58, 844.
- (18) Baltes, N.; Thouin, L.; Amatore, C.; Heinze, J. *Angew. Chem., Int. Ed.* 2004, 43, 1431.
- (19) Bi, S.; Liu, B.; Fan, F.-R. F.; Bard, A. J. *J. Am. Chem. Soc.* 2005, 127, 3690

- (20) Sanchez-Sanchez, C. M.; Rodriguez-Lopez, J.; Bard, A. J. *Anal. Chem.* **2008**, *80*, 3254.
- (21) Rodgers, P. J.; Amemiya, S.; Wang, Y.; Mirkin, M. V. *Anal. Chem.* **2010**, *82*, 84.
- (22) Wang, Y.; Velmurugan, J.; Mirkin, M. V.; Rodgers, P. J.; Kim, J.; Amemiya, S. *Anal. Chem.* **2010**, *82*, 77.
- (23) Lefrou, C. J. *Electroanal. Chem.* **2006**, *592*, 103.
- (24) Zuliani, C.; Walsh, D. A.; Keyes, T. E.; Forster, R. J. *Anal. Chem.* **2010**, *82*, 7135.
- (25) Ghilane, J.; Lagrost, C.; Hapiot, P. *Anal. Chem.* **2007**, *79*, 7383.
- (26) Fan, F. R. F.; Bard, A. J. *Anal. Chem.* **1988**, *60*, 751.
- (27) Shan, X. N.; Patel, U.; Wang, S. P.; Iglesias, R.; Tao, N. J. *Science* **2010**, *327*, 1363.
- (28) Lefrou, C. J. *Electroanal. Chem.* **2006**, *592*, 103.
- (29) Bard, A. J.; Faulkner, L. R. In *Electrochemical Methods: Fundamentals and Applications*, 2nd ed.; John Wiley & Sons: New York, **2001**, pp 94.
- (30) Feldberg, S. W.; Newton, M. D.; Smalley, J. F. In *Electroanalytical Chemistry: A Series of Advances, Vol 22*; Bard, A. J., Rubinstein, I., Eds.; Marcel Dekker, 2004; Vol. 22, pp 101.
- (31) Ref 29, pp 247.
- (32) Zoski, C. G.; Luman, C. R.; Fernandez, J. L.; Bard, A. J. *Anal. Chem.* **2007**, *79*, 4957.
- (33) Mirkin, M. V.; Bard, A. J. *Anal. Chem.* **1992**, *64*, 2293.
- (34) Mirkin, M. V.; Richards, T. C.; Bard, A. J. *J. Phys. Chem.* **1993**, *87*, 7672.
- (35) Martin, R. D.; Unwin, P. R. *J. Electroanal. Chem.* **1997**, *439*, 123.
- (36) Martin, R. D.; Unwin, P. R. *Anal. Chem.* **1998**, *70*, 276.
- (37) Kim, J.; Izadyar, A.; Nioradze, N.; Amemiya, S. *J. Am. Chem. Soc.* **2013**, *135*, 2321–2329.
- (38) Zhang, B.; Galusha, J.; Shiozawa, P. G.; Wang, G.; Bergren, A. J.; Jones, R. M.; White, R. J.; Ervin, E. N.; Cauley, C. C.; White, H. S. *Anal. Chem.* **2007**, *79*, 4778.
- (39) Sun, P.; Mirkin, M. V. *Anal. Chem.* **2006**, *78*, 6526.

- (40) Katemann, N. B.; Schuhmann, W. *Electroanalysis* **2002**, *14*, 22.
- (41) Ishimatsu, R.; Kim, J.; Jing, P.; Striemer, C. C.; Fang, D. Z.; Fauchet, P. M.; McGrath, J. L.; Amemiya, S. *Anal. Chem.* **2010**, *82*, 7127.
- (42) Shao, Y.; Mirkin, M. V. *J. Phys. Chem. B* **1998**, *102*, 9915.
- (43) Cornut, R.; Lefrou, C. *J. Electroanal. Chem.* **2007**, *608*, 59.

3.0 GENERALIZED THEORY FOR NANOSCALE VOLTAMMETRIC MEASUREMENTS OF HETEROGENEOUS ELECTRON-TRANSFER KINETICS AT MACROSCOPIC SUBSTRATES BY SCANNING ELECTROCHEMICAL MICROSCOPY

This work has been published as Shigeru Amemiya, Nikoloz Nioradze, Padmanabhan Santhosh, and Michael J. Deible, Generalized Theory for Nanoscale Voltammetric Measurements of Heterogeneous Electron-Transfer Kinetics at Macroscopic Substrates by Scanning Electrochemical Microscopy, *Anal. Chem.* **2011**, 83, 5928–5935. The thesis author contributed in considering nanoscale experimental conditions.

3.1 INTRODUCTION

Here we report on a generalized theory for scanning electrochemical microscopy to enable the voltammetric investigation of a heterogeneous electron-transfer (ET) reaction with arbitrary reversibility and mechanism at the macroscopic substrate. In this theory, we consider comprehensive nanoscale experimental conditions where a tip is positioned at a nanometer distance from a substrate to detect the reactant or product of a substrate reaction at any potential in the feedback or substrate generation/tip collection mode, respectively. Finite element simulation with the Marcus–Hush–Chidsey formalism predicts that a substrate reaction under the nanoscale mass transport conditions can deviate from classical Butler–Volmer behavior to enable the precise determination of standard ET rate constant and reorganization energy for a redox couple from the resulting tip current–substrate potential voltammogram as obtained at quasi-steady state. Simulated voltammograms are generalized in the form of analytical equations to allow for reliable kinetic analysis without the prior knowledge of the rate law. Our theory also predicts that a limiting tip current can be controlled kinetically to be smaller than the diffusion-limited current when a relatively inert electrode material is investigated under the nanoscale voltammetric conditions.

Scanning electrochemical microscopy (SECM) has been successfully applied for the investigation of heterogeneous electron-transfer (ET) reactions at various electroactive substrates comprised of metals, semiconductors, and carbons as well as those modified with monolayers and polymers.^{1, 2} Most of these SECM studies of important electrode materials are based on steady-state feedback measurements.³ Steady-state conditions facilitate imaging of heterogeneous substrate surfaces and kinetic mapping of "hot" spots, and simplify the measurement and analysis of an approach curve, a plot of tip current versus tip–substrate distance, from which a local ET rate constant can be determined conveniently using analytical equations.⁴ The feedback mode is also useful for the quantitative study of heterogeneous ET kinetics at unconventional substrates such as unbiased conductors,⁵ air/water interfaces,⁶ liquid/liquid interfaces,⁷ and biological cells.⁸

SECM has also emerged as a vital tool in nanoelectrochemistry^{9, 10} to realize unprecedentedly fast kinetic measurements of electrode reactions under extremely high mass transport conditions. The powerfulness of the feedback mode with nanometer distances between the SECM tip and the substrate was demonstrated in the kinetic study of rapid ET reactions at nanotips,^{11, 12} the electrogeneration and detection of short-lived intermediates,¹³ and the electrochemical detection of single molecules.¹⁴⁻¹⁶ Alternatively, nanoscale mass transport conditions can be achieved even with micrometer tip–substrate distances when individual nanobands¹⁷⁻¹⁹ and single-walled carbon nanotubes²⁰ are investigated as SECM substrates.

Recently, we developed a powerful SECM method based on both feedback and substrate generation/tip collection (SG/TC) modes to enable quasi-steady-state voltammetry of rapid ET reactions at macroscopic substrates by employing nanometer tip–substrate distances.²¹ With this method, the reactant, O, or product, R, of a reversible substrate reaction ($O + e \rightarrow R$) is amperometrically detected at the tip in the feedback or SG/TC mode, respectively, during the cyclic sweep of substrate potential, E_s , across the formal potential of the redox couple, E^0 . Despite the voltammetric growth of a planar diffusion layer at the macroscopic substrate, the tip current, i_T , in either operation mode immediately reaches quasi-steady state at nanometer tip–substrate distances, where concentrations of a reversible redox couple are always

equilibrated with substrate potential. Moreover, the resulting high mass transport of redox mediators across the narrow tip–substrate gap kinetically limits the rapid ET reaction at the substrate surface under the tip. Advantageously, a pair of quasi-steady-state i_T – E_S voltammograms thus obtained in feedback and SG/TC modes allow for the reliable determination of kinetic and thermodynamic parameters in the Butler-Volmer (BV) model as well as all transport parameters. A standard ET rate constant, k^0 , of 7 cm/s was determined by nanoscale i_T – E_S voltammetry at tip–substrate distances of ~90 nm as one of the largest k^0 values reported for heterogeneous ET reactions.^{10, 22} In contrast, we predict in this work that, except for these fastest ET reactions, the BV model is not appropriate under high mass transport conditions as practiced for the various nanoscale SECM measurements.

Here we report on a generalized theory for nanoscale i_T – E_S voltammetry of substrate reactions with arbitrary reversibility and mechanism under comprehensive experimental conditions including any substrate potential and both feedback and SG/TC modes. We employ the Marcus–Hush–Chidsey (MHC) formalism for heterogeneous outer-sphere ET reactions²³⁻²⁵ to enable time-dependent finite element simulations of nanoscale i_T – E_S voltammograms for various kinetic regimes beyond the limit of BV kinetics. The MHC model is more realistic at large overpotentials where ET rate constants become smaller than predicted by BV kinetics and eventually become overpotential-independent in contrast to classical Marcus "inverted" behavior.²⁶ This limiting behavior at extreme overpotentials is due to the continuum of electronic states in the electrode and was observed by chronoamperometry of redox centers attached to metal and carbon ultramicroelectrodes.²⁷ Also, the manifestation of a limiting ET rate constant for a diffusional system has been theoretically predicted for steady-state voltammetry at disk nanoelectrodes²⁴ and single-walled carbon nanotubes²⁸ and also reported for cyclic voltammetry of outer-sphere redox couples at gold macroelectrodes modified with self-assembled monolayers of insulating alkanethiols.²⁹

Importantly, nanoscale i_T – E_S voltammograms thus simulated for both feedback and SG/TC modes are generalizable in the form of analytical equations. These equations allow for the determination of an ET rate

constant from a tip current without the prior knowledge of the rate law to reveal the potential-dependence of both cathodic and anodic processes at the substrate from the paired voltammograms. The feasibility of the SECM observation of MHC voltammetric responses at relatively inert electrode materials is theoretically assessed using the numerical and analytical approaches with kinetic parameters as determined by cyclic voltammetry of outer-sphere redox couples at the low-defect basal plane surface of highly oriented pyrolytic graphite (HOPG).³⁰

3.2 MODEL

As reported elsewhere,²¹ our model is defined in a cylindrical coordinate, where a disk-shaped SECM tip is faced in parallel to the surface of a disk-shaped substrate. The disk radius of the macroscopic substrate is 50 times larger than the tip radius, a , and is large enough not to affect simulation results. Feedback and SG/TC modes of SECM are employed to monitor a first-order one-electron process at a macroscopic substrate as given by



where $k_{S,f}$ and $k_{S,b}$ are first-order heterogeneous ET rate constants. The cathodic rate constant is defined by the MHC formalism as²⁴

$$k_{S,f} = k^0 \exp\left(-\frac{E^*}{2}\right) \int_{-\infty}^{\infty} \frac{\exp\left[-\frac{(\varepsilon^* - E^*)^2}{4\lambda^*}\right]}{2 \cosh\left[\frac{\varepsilon^*}{2}\right]} d\varepsilon^* / \int_{-\infty}^{\infty} \frac{\exp\left[-\frac{(\varepsilon^*)^2}{4\lambda^*}\right]}{2 \cosh\left[\frac{\varepsilon^*}{2}\right]} d\varepsilon^*
 \tag{2}$$

With

$$E^* = \frac{F(E_S - E^{0'})}{RT} \quad (3)$$

$$\lambda^* = \frac{\lambda}{k_B T} \quad (4)$$

$$\varepsilon^* = \frac{\varepsilon}{k_B T} \quad (5)$$

where λ (eV) is the reorganization energy of the redox couple and ε is an integration variable. The potential-independence of k^0 in this model implies that the density of states in the electrode is constant and independent of the potential and that the electronic interaction between a redox molecule and each energy level in the electrode is independent of the energy level and of the neighboring levels.³¹ Alternatively, the BV model gives

$$k_{S,f} = k^0 \exp(-\alpha E^*) \quad (6)$$

where α is the transfer coefficient. In either model, the Nernst equation must be satisfied at equilibrium, which requires²⁵

$$k_{S,b} = k_{S,f} \exp(E^*) \quad (7)$$

Finite element simulations were carried out using COMSOL Multiphysics (version 4.1[®], COMSOL, Inc., Burlington, MA) linked to Matlab (version 2010b, MathWorks, Natick, MA). The potential-dependence of cathodic (eq 2) and anodic (eq 7) rate constants, i.e., $k_{S,f}/k^0$ and $k_{S,b}/k^0$, respectively, were evaluated for various λ^* values using Matlab and Mathematica (version 7, Wolfram Research, Inc., Champaign, IL) to find that outcomes of these two approaches agree very well with each other (Figure 1). Moreover, calculated $k_{S,f}/k^0$ and $k_{S,b}/k^0$ values approach to limiting values, k_{lim}/k^0 , reported by Feldberg as²⁴

$$\frac{k_{\text{lim}}}{k^0} = \frac{\sqrt{4\pi\lambda^*} \exp\left(\frac{\lambda^*}{4}\right)}{\left[\pi - \frac{\pi^3}{4(\lambda^* + 4.31)}\right]} \quad (8)$$

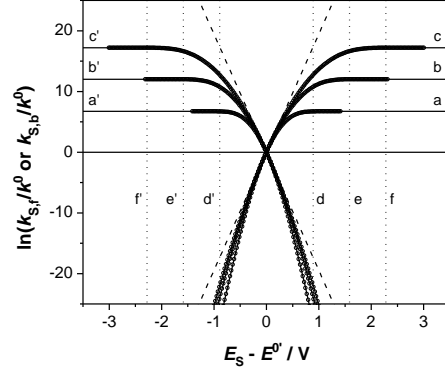


Figure 3-1. Potential-dependent parts of MHC ET rate constants, $k_{S,r}/k^0$ and $k_{S,b}/k^0$, for reduction and oxidation, respectively, at the substrate as evaluated using Matlab for $\lambda^* =$ (a, a') 20, (b, b') 40, and (c, c') 60 as well as using Mathematica (circles). Dotted lines represent substrate potentials where 99 % of k_{lim} is achieved for $\lambda^* =$ (d, d') 20, (e, e') 40, and (f, f') 60 at 298 K (see eq 9). Dashed lines represent BV kinetics with $\alpha = 0.5$

Our results also confirm that >99% of k_{lim} is achieved when overpotential (equivalent to $E_S - E^0$ in this work) is large enough with respect to λ to satisfy the following conditions²⁴

$$|E_S - E^0| \geq 1.35\lambda + \frac{7.7RT}{F} \quad (9)$$

Potential-dependent parts of rate constants thus calculated using Matlab were called externally from COMSOL Multiphysics through Livelink Matlab to define the boundary condition at the substrate surface. Two-dimensional, time-dependent diffusion problems for SECM were solved using the following dimensionless parameters as reported elsewhere²¹

$$\lambda'_0 = k^0 d / D_O \quad (\text{dimensionless standard ET rate constant}) \quad (10)$$

$$L = d / a \quad (\text{dimensionless tip-substrate distance}) \quad (11)$$

$$\sigma = a^2 Fv / 4D_O RT \quad (\text{dimensionless sweep rate for substrate potential}) \quad (12)$$

$$\xi = \sqrt{D_O / D_R} \quad (\text{dimensionless diffusion coefficient ratio}) \quad (13)$$

where d is the tip-substrate distance, v is the sweep rate for substrate potential, and D_O and D_R are diffusion coefficients of species O and R, respectively, in the bulk solution. Unfortunately, "simulation report" cannot be generated using the version 4.1 of COMSOL Multiphysics. Simulation files used for this work are available upon request.

A tip current was calculated for the diffusion-limited amperometric detection of the original mediator, O, in the feedback mode or the substrate-generated species, R, in the SG/TC mode to give a pair of i_T - E_S voltammograms at the same tip-substrate distance. A tip current was obtained in the normalized form (eq 20) with respect to the diffusion-limited current for species O at the tip in the bulk solution, $i_T(\infty)$, as given by

$$i_T(\infty) = 4xnFD_O c_O^* a \quad (14)$$

where x is expressed by eq 21³² as a function of RG ($= r_g/a$; r_g is the outer tip radius, and $RG = 1.5$ and, correspondingly, $x = 1.16$ are employed in this work), $n = 1$ for a one-electron process considered in this model (eq 1), and c_O^* is the concentration of the original mediator in the bulk solution. The x values simulated for different RG values at $L = 50$ agree with theoretical values given by eq 22, thereby validating our simulation results. The dimensionless flux of species O at the macroscopic substrate represents a substrate current. Positive tip (and substrate) currents are based on reduction of the original mediator. Subsequently, feedback and SG/TC tip responses appear in upper and lower panels of the following graphs, respectively.

3.3 RESULTS AND DISCUSSION

3.3.1 Simulations of Nanoscale i_T - E_S Voltammograms Based on the MHC

Formalism

Dimensionless kinetic parameters, λ^* (eq 4) and λ'_O (eq 10), in the MHC formalism were systematically varied to simulate i_T - E_S voltammograms for various kinetic regimes at nanoscale tip-substrate distances (Figures 3-2, 3-7, and 3-8 for $\lambda^* = 40, 60,$ and $20,$ respectively). These λ^* values correspond to realistic λ values of 0.5–1.5 eV at 298 K (i.e., 12–36 kcal/mol) as estimated theoretically³³ or determined experimentally^{29, 34, 35} for various outer-sphere redox mediators (Table 3-1). Characteristic features of the MHC behavior were fully demonstrated by varying λ'_O in a wide range, e.g., from 10 to 10^{-6} for $\lambda^* = 40$ (Figure 3-2). In addition, the tip-substrate distance and time scale of simulations were set to $L = 0.25$ and $\sigma = 4 \times 10^{-4}$, respectively, which are small enough to give quasi-steady-state i_T - E_S voltammograms at any E_S when the reaction at the macroscopic substrate is reversible.²¹ Also, these small L and σ values can be achieved experimentally using an inlaid disk tip with a submicrometer²¹ or nanometer¹¹ radius. For instance, a sharp SECM tip with $a = \sim 0.5 \mu\text{m}$ and $RG = 1.5$ – 2.5 can be readily positioned within $L = 0.25$ ($d = 0.125 \mu\text{m}$ in eq 11) from the substrate surface.²¹ This small L value is also achievable using carefully polished and aligned nanotips.¹¹ With $a \leq 0.5 \mu\text{m}$, the cyclic sweep of substrate potential at $v \leq 100 \text{ mV/s}$ is equivalent to $\sigma \leq 4 \times 10^{-4}$ for a redox mediator with a typical D_O value of $5 \times 10^{-6} \text{ cm}^2/\text{s}$ (see eq 12). In addition, $D_O = D_R$ ($\xi = 1$) was assumed for simplicity although a reversible redox couple with $D_O \neq D_R$ gives a quasi-steady-state i_T - E_S voltammogram in either feedback or SG/TC mode with such small σ and $RG (= 1.5)$.²¹

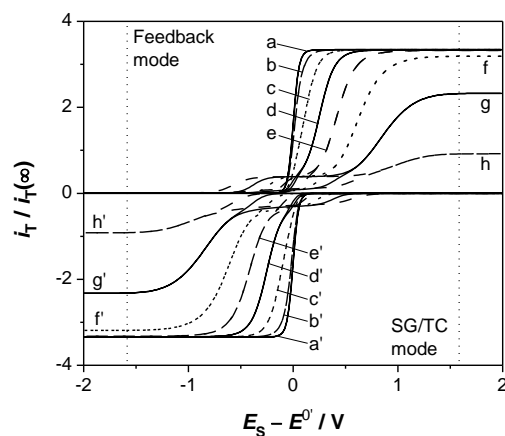


Figure 3-2. Simulated i_T-E_S voltammograms based on the MHC formalism with $\lambda^* = 40$ and $\log \lambda'_0 = (a, a')$ 1, (b, b') 0, (c, c') -1, (d, d') -2, (e, e') -3, (f, f') -4, (g, g') -5, and (h, h') -6. Dotted lines correspond to substrate potentials where 99 % of k_{lim} is achieved at 298 K (see eq 9).

Simulation results with either BV²¹ or MHC model demonstrate that the reversibility of the reaction at the macroscopic substrate controls substrate potentials where a steady-state or quasi-steady-state tip current is obtained in i_T-E_S voltammetry. The whole i_T-E_S voltammogram in either feedback or SG/TC mode is obtained under steady-state or quasi-steady-state conditions to be sigmoidal and completely retraceable at any substrate potential on its cyclic sweep ($\lambda'_0 = 10$ and 1 in Figure 3-2) when the reaction at the macroscopic substrate is reversible as confirmed by simulated cyclic voltammograms (CVs) at the substrate (Figure 3-9). Note that the substrate reaction with $\lambda'_0 = 1$ is locally quasi-reversible under the tip, thereby yielding a broader i_T-E_S voltammogram than the reversible counterpart with $\lambda'_0 = 10$. On the other hand, the tip current does not always reach to steady state or quasi-steady state when the reaction at the macroscopic substrate is kinetically limited to give a non-nernstian substrate CV ($\lambda'_0 \leq 0.1$ in Figure 3-9). The corresponding i_T-E_S voltammograms (Figure 3-2) are retraceable only if substrate potentials are far

enough from E^0 to drive the reaction at the macroscopic substrate to a diffusion limit. Irretraceable portions of the voltammograms around $E_S = E^0$ are transient and give higher current on the forward (or reverse) potential sweep in the feedback (or SG/TC) mode. The substantial current in the feedback mode around $E_S = E^0$ on the forward sweep is due to negative feedback effect at the tip, where mediator molecules diffuse from the bulk solution to be electrolyzed without being regenerated at the practically inert substrate surface in this potential range. In the SG/TC mode, mediator molecules are generated at the whole substrate surface on the forward sweep to be detected at the tip on the reverse sweep, where the magnitude of the tip current around $E_S = E^0$ is close to that of the negative feedback current expected at this tip–substrate distance.

Unique voltammetric features of MHC responses are seen in retraceable portions of i_T-E_S voltammograms. These features are similar to those predicted for steady-state voltammograms at disk electrodes²⁴ except that they are completely sigmoidal without an irretraceable portion. Specifically, the retraceable portion of an i_T-E_S voltammogram based on the MHC mechanism becomes broader than that based on the BV mechanism with $\alpha = 0.5$ when a substrate reaction is slow enough, for instance, $\lambda'_0 < 10^{-1}$ with $\lambda^* = 40$ (Figure 3-2). Importantly, this requirement is achieved even with relatively fast substrate reactions under nanoscale mass transport conditions, e.g., $\lambda'_0 < 10^{-1}$ in eq 9 with $D_O = 5 \times 10^{-6}$ cm²/s corresponds to $k^0 < 0.1$ and < 1 cm/s at $d = 50$ and 5 nm, respectively. In other words, the BV model breaks down at $d = 5$ nm except for fastest ET reactions ($k^0 > 1$ cm/s) reported so far.^{10, 22} More strikingly, the limiting current of an i_T-E_S voltammogram for a slower reaction, for instance, $\lambda'_0 < 10^{-3}$ with $\lambda^* = 40$, becomes smaller than the diffusion-limited current as observed with $\lambda'_0 \geq 10^{-3}$. This smaller limiting current is controlled by k_{lim} at extreme substrate potentials (see eqs 8 and 9).²⁴ Interestingly, this result indicates that an approach curve to a metal at this kinetic limit is more negative than the diffusion-limited positive feedback curve (see below). Overall, broad shapes and low kinetic limiting currents of steady-state and quasi-steady-state MHC responses are observed more readily for a redox couple with smaller λ^* ,

subsequently, with larger λ'_0 and at less extreme potentials (see Figures 3-7 and 3-8 for $\lambda^* = 60$ and 20, respectively).

Noticeably, retraceable portions of i_T-E_S voltammograms in feedback and SG/TC modes display inversion symmetry against E^0 (Figures 3-2, 3-7, and 3-8) as expected from the reciprocity relation of $k_{s,f}(E^*) = k_{s,b}(-E^*)$ in the MHC formalism²⁵ (see eqs 2 and 7). In contrast, retraceable portions of i_T-E_S voltammograms based on the BV mechanism display inversion symmetry only if $\alpha = 0.5$ ²¹ (Figure 3-10). In either mechanism, inversion symmetry is compromised in irretraceable portions around $E_S = E^0$ due to concentration inequalities²⁵ between feedback and SG/TC modes.

3.3.2 Determination of Kinetic Parameters from MHC Responses

Here we demonstrate that λ'_0 and λ^* (and subsequently k^0 and λ) in the MHC mechanism can be determined precisely by nanoscale i_T-E_S voltammetry when a reaction at the macroscopic substrate is slow enough to reveal the dependence of its rate on reorganization energy at large overpotentials without a diffusion limit. The specific conditions required for the complete kinetic analysis of a MHC response is assessed by comparing i_T-E_S voltammograms of redox couples with $\lambda^* = 40$ and 60 in the feedback mode. Such a comparison of the corresponding voltammograms in the SG/TC mode does not provide additional kinetic information because of the inversion symmetry of the paired voltammograms.

The precision of λ'_0 and λ^* values that are determined from a MHC voltammetric response depends on the range of substrate potentials where the retraceable portion of an i_T-E_S voltammogram is observed. With $\lambda'_0 = 0.1$ (Figure 3a), i_T-E_S voltammograms with $\lambda^* = 40$ and 60 (circles and solid line, respectively) are indistinguishable and barely broader than the i_T-E_S voltammogram based on BV kinetics with $\alpha = 0.5$ (dotted line). In this kinetic regime, only λ'_0 can be determined uniquely from an i_T-E_S voltammogram, which is independent of λ^* . This result confirms that the MHC mechanism and the BV

mechanism with $\alpha = 0.5$ are equivalent in the potential region in the vicinity of E^0 (see Figure 3-1).²⁴ As λ'_0 decreases to 10^{-2} and then to 10^{-3} (Figures 3-3b and 3-3c, respectively), an i_T-E_S voltammograms based on the MHC mechanism becomes broader and shifts toward more extreme potentials than expected from the BV mechanism with $\alpha = 0.5$. Moreover, an i_T-E_S voltammogram with smaller λ^* is broader for a given. Nevertheless, i_T-E_S voltammograms with $\lambda^* = 40$ and 60 are nearly indistinguishable for $\lambda'_0 = 10^{-2}$ because they overlap with each other when slightly smaller λ^* is employed for $\lambda^* = 60$ (dashed line). In contrast, such adjustment does not superimpose i_T-E_S voltammograms with $\lambda^* = 40$ and 60 for a slower substrate reaction with $\lambda'_0 = 10^{-3}$, thereby enabling the separate determination of λ^* and λ'_0 . Eventually, λ^* can be determined most precisely when λ'_0 is small enough to kinetically control a limiting current. With $\lambda'_0 = 10^{-4}$ (Figure 3-3d), an i_T-E_S voltammogram with $\lambda^* = 40$ gives a kinetic limiting current at substrate potentials where the diffusion-limited current is observed for $\lambda^* = 60$ in the range of $\lambda'_0 = 10^{-4}$ – 10^{-5} . Moreover, the i_T-E_S voltammograms with $\lambda^* = 60$ are much steeper than the voltammogram with $\lambda^* = 40$.

Overall, the MHC response that is unique with a typical λ^* value of 40 is seen with $\lambda'_0 \leq 10^{-3}$, which corresponds to $k^0 \leq 10^{-3}$ cm/s in eq 10 with $D_O = 5 \times 10^{-6}$ cm²/s and $d = 50$ nm. Such low k^0 values have been reported for outer-sphere redox mediators at relatively inert electrode materials such as HOPG (Table 3-1). In addition, reliable kinetic analysis requires the potential window that is wide enough to observe at least the retraceable portion of a broad voltammogram based on the MHC mechanism. These requirements are assessed below.

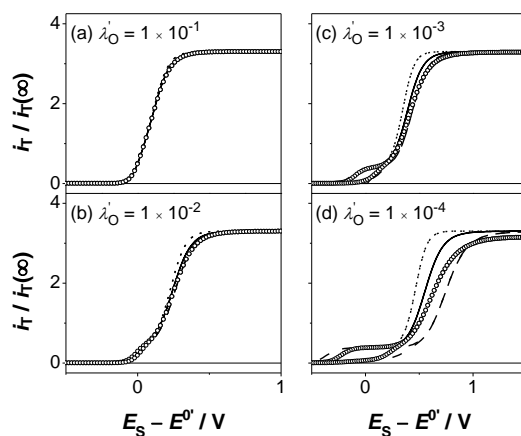


Figure 3-3. Simulated i_T - E_S voltammograms based on MHC kinetics with $\lambda^* = 40$ (circles) and 60 (solid lines) and BV kinetics with $\alpha = 0.5$ (dotted lines). Dashed lines represent MHC responses with $\lambda^* = 60$ and $\lambda'_O =$ (b) 7.5×10^{-3} , (c) 5×10^{-4} , and (d) 1×10^{-5} .

The accurate determination of kinetic parameters from an i_T - E_S voltammogram based on the MHC mechanism requires the discrimination of a MHC response from a BV response. In fact, a steady-state voltammogram based on the MHC mechanism can be fitted with that based on the BV mechanism to yield erroneous α and k^0 values.²⁴ Importantly, a MHC response can be unambiguously discriminated from a BV response by measuring a pair of i_T - E_S voltammograms in both feedback and SG/TC modes. Such a pair of voltammograms based on the MHC mechanism display inversion symmetry against E^0 in contrast to the corresponding pair of i_T - E_S voltammograms based on the BV mechanism with $\alpha \neq 0.5$. Specifically, a broad i_T - E_S voltammogram based on the MHC mechanism in the feedback (or SG/TC) mode can be fitted well using the BV model with incorrectly large k^0 and anomalously large (or small) α , which compromises inversion symmetry (Figure 3-4a). Subsequently, the corresponding MHC voltammogram in the SG/TC (or feedback) mode cannot be fitted with the much steeper voltammogram based on the BV model, thereby revealing its inappropriateness in this kinetic regime. Advantageously, a pair of i_T - E_S voltammograms in

feedback and SG/TC modes are obtained simply by setting the tip potential within an appropriate range in the presence of only oxidized or reduced form of a redox couple in the bulk solution.²¹ In contrast, both oxidized and reduced forms of a redox couple must be prepared and stable in the bulk solution to obtain a pair of steady-state voltammograms at ultramicroelectrodes, which was proposed to avoid the erroneous analysis of a MHC response using the BV model.²⁴ Noticeably, reliable kinetic analysis using a pair of steady-state voltammograms was demonstrated both theoretically³⁶ and experimentally^{37, 38} for nanopipet voltammetry of rapid ion transfers at liquid/liquid interfaces.

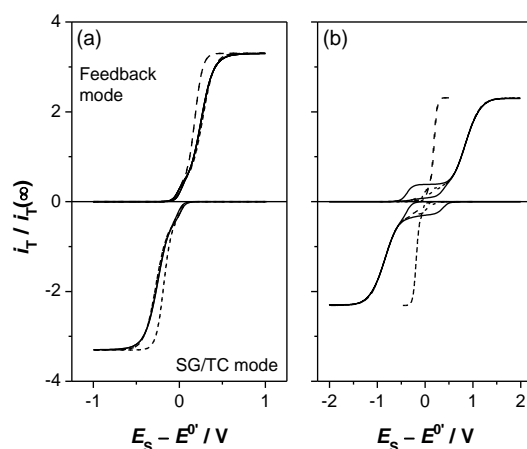


Figure 3-4. Simulated i_T - E_S voltammograms based on the MHC formalism (solid lines) with $\lambda^* = 40$ and λ'_0 = (a) 1×10^{-3} and (b) 1×10^{-5} . Dashed and dotted lines represent simulated i_T - E_S voltammograms based on BV kinetics with (a) $\lambda'_0 = 5 \times 10^{-2}$ and $\alpha = 0.60$ and 0.40 , respectively, and (b) $\lambda'_0 = 9 \times 10^{-3}$ and $\alpha = 0.82$ and 0.18 , respectively.

Additionally, the irretraceable portion of an i_T - E_S voltammogram is useful for the discrimination of a MHC response from a BV response when a substrate reaction is slow enough to give a plateau current around $E_S = E^0$ (Figures 3-4b). Since a slower substrate reaction gives the low plateau current in a wider range of substrate potentials, irretraceable portions of i_T - E_S voltammograms based on MHC and BV

mechanisms are not superimposed when erroneously large λ'_0 is employed in the BV model to fit retraceable portions with each other (Figure 3-4b). Moreover, this fitting procedure requires the adjustment of the diffusion-limited current of the BV response to the kinetic limiting current of the MHC response, which is detected as an error in the tip–substrate distance.²¹ Overall, the discrimination of a MHC response from a BV response in this slow kinetic regime requires only feedback or SG/TC mode, which is useful when only one of the very broad voltammograms is observable within the potential window.

It should be noted that the symmetric broadening of a pair of i_T – E_S voltammograms due to the MHC effect can be discriminated from their asymmetric broadening due to the effect of electrical double layer on a substrate reaction. The asymmetric double-layer effect on rates of forward and reverse substrate reactions results from (i) different charges of oxidized and reduced forms of a redox couple and (ii) different potentials for their electrolysis at the outer Helmholtz plane.³⁹ For instance, the double-layer effect is negligible in the feedback (or SG/TC) mode based on the substrate reaction of an electrically neutral form but can be significant in the SG/TC (or feedback) mode based on the reverse reaction of the other form, which must be charged. A distinction between MHC and double layer effects illustrates the advantage of a pair of steady-state (or quasi-steady-state) voltammograms based on forward and reverse reactions against a single sigmoidal voltammogram dominated by one of the reactions.

3.3.3 Analytical Equations for Nanoscale i_T – E_S Voltammograms

The retraceable portion of an i_T – E_S voltammogram in either feedback or SG/TC mode is obtained under steady-state or quasi-steady-state conditions and, subsequently, can be represented by analytical equations to facilitate its kinetic analysis even when the rate law is unknown (see below). In the steady-state feedback mode, the normalized tip current, $I_T(L, E_S)$, is given by⁴

$$I_T(L, E_S) = I_{T,PF}(L + 1 / \Lambda, RG) + \frac{I_{T,NF}(L, RG) - 1}{(1 + 2.47RG^{0.31} \Lambda)(1 + L^{0.006RG+0.11331} \Lambda^{-0.0236RG+0.91})} \quad (15)$$

with

$$\Lambda = \frac{k_{S,b}a}{D_O} \quad (16)$$

where $I_{T,PF}$ and $I_{T,NF}$ represent normalized tip currents in purely positive and negative feedback conditions and are given by eqs 22 and 24, respectively. Eq 15 fits very well with retraceable portions of the voltammograms simulated for the feedback mode in slow kinetic regimes including those with kinetic limiting currents (top panels of Figure 3-11). For this comparison, potential-dependent $k_{S,b}$ values in eq 15 were calculated from a combination of eqs 2 and 7 using Mathematica (see Figure 1). Interestingly, eq 15 is also applicable for the SG/TC mode when $k_{S,b}$ is replaced by $k_{S,f}$ in eq 16 and $D_O = D_R$ ($\xi = 1$) is assumed (bottom panels of Figure 3-11). Overall, good fits as obtained with eq 15 demonstrate that an i_T-E_S voltammogram in either operation mode is retraceable when a substrate reaction under the tip is totally irreversible and opposite to the tip reaction. In addition, eq 15 agrees well with low plateau currents around $E_S = E^0$ on forward and reverse potential sweeps in feedback and SG/TC modes, respectively. This agreement is slightly compromised for the latter mode because the substrate-generated species continuously diffuses away from the substrate surface to the bulk solution in this plateau-current region. Due to the resulting concentration inequalities,²⁵ inversion symmetry between the forward feedback wave and the reverse SG/TC wave is compromised.

We also propose the following analytical equations for feedback and SG/TC modes, which are more useful than eq 15 when an ET mechanism is unknown (see Supporting Information for their derivations)

$$I_{T,O}^{FB}(E_S, L) = \frac{\pi}{2xL(2/\theta_S + 2D_O/k_{S,b}d + \xi^2 + 1)} + \frac{\xi\theta_S}{\xi\theta_S + 1} \left[I_{T,lim}(L) - \frac{\pi}{2xL(2D_O/k_{lim}d + \xi^2 + 1)} \right] \quad (17)$$

$$I_{T,R}^{ST}(E_S, L) = - \left\{ \frac{\pi}{2xL(2\xi^2\theta_S + 2D_O/k_{S,f}d + \xi^2 + 1)} + \frac{1}{\xi\theta_S + 1} \left[\frac{I_{T,lim}(L)}{\xi} - \frac{\pi}{2xL(2D_O/k_{lim}d + \xi^2 + 1)} \right] \right\} \quad (18)$$

where $I_{T,O}^{FB}(E_S, L)$ and $I_{T,R}^{ST}(E_S, L)$ represent normalized tip currents for the respective operation modes, $\theta_S = \exp(E^*)$, and $I_{T,lim}(L)$ is the normalized limiting current. In comparison to eq 15, eqs 17 and 18 can be more easily solved for $k_{S,b}$ and $k_{S,f}$ as functions of the tip current while k_{lim} must be determined from $I_{T,lim}(L)$ using eq 15. Subsequently, a pair of plots of $k_{S,f}$ or $k_{S,b}$ versus E_S , e.g., Figure 1, can be obtained from a pair of i_T - E_S voltammograms in feedback and SG/TC modes to reveal the potential-dependence of both anodic and cathodic processes at the substrate.

Noticeably, eqs 17 and 18 are valid under steady-state and quasi-steady-state conditions²¹ and do not reproduce irretraceable portions of a voltammogram (Figure 3-11).

Analytical equations are useful for the analysis of approach curves, for which eq 15 was originally applied.⁴ Figure 3-5 shows approach curves generated using eq 15 with the MHC formalism, where $k_{S,b}$ at various overpotentials were calculated using eqs 2 and 7 with $\lambda^* = 40$. In this example, the slow substrate reaction that corresponds to $\lambda'_0 = 10^{-5}$ at $d/a = 0.25$ as used for curves g and g' in Figure 3-1 was considered to emphasize the difference between MHC and BV mechanisms. As overpotential becomes more positive, i.e., Λ becomes larger, the corresponding approach curve based on the MHC mechanism becomes more positive and then reaches to a kinetically limited curve (curve a), which is more negative than the purely positive feedback curve expected for the BV mechanism (dotted line).

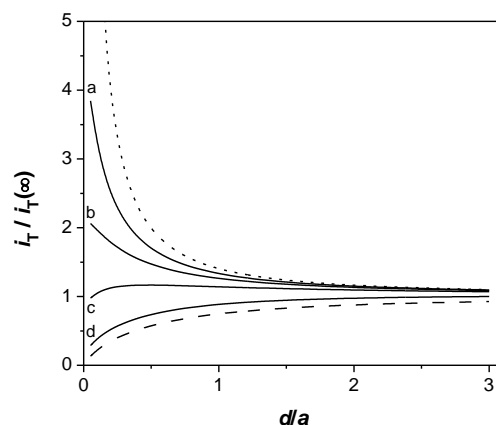


Figure 3-5. Theoretical approach curves (solid lines) calculated using eq 15 with the MHC formalism for $\lambda^* = 40$ and $\Lambda =$ (a) 6.7, (b) 2.8, (c) 1.1, and (d) 0.15. Dotted and dashed lines represent purely positive (eq 23) and negative (eq 22) feedback curves, respectively.

3.3.4 Experimental Observation of MHC Limiting Current

Here we consider the low-defect basal plane surface of HOPG as a model substrate to quantitatively predict that the kinetic limiting current of a MHC voltammetric response will be observable at such a relatively inert electrode by employing nanoscale i_T - E_S voltammetry. Estimated λ values³³ and experimental k^0 values^{40, 41} for various redox mediators at the HOPG surface were used to obtain k_{lim} from eq 8 by assuming that the MHC formalism is valid also for semi-metallic HOPG.³³ With a k_{lim} value, normalized limiting currents, $I_{T,lim}$, at $L = 0.25$ were calculated using eq 15 with $a = 20$ and 200 nm, i.e., $d = 5$ and 50 nm, respectively, and $D_O = 5 \times 10^{-6}$ cm²/s. The comparison of $I_{T,lim}$ with the diffusion-limited $I_{T,PF}$ value (Table 3-1) indicates that mass transport across 5–50 nm-wide tip–substrate gaps is efficient enough to exert significant kinetic effect on a limiting current for redox mediators with $\lambda = 0.6$ – 1.3 eV including MV2 $^{+}/+$ (MV = methylviologen), IrCl₆²⁻³⁻, Fc(COOH)₂⁺⁰ (1,1'-dicarboxyferrocene), W(CN)₈³⁻⁴⁻, Ru(CN)₆³⁻⁴⁻, and Fe(CN)₆³⁻⁴⁻. Moreover, broad i_T - E_S voltammograms of these mediators in the feedback (or SG/TC) mode are observable within the potential limit of HOPG, which is wider than ± 1.0 V versus SCE⁴² and satisfies eq

9 for these mediators in the corresponding operation mode (Table 3-1). In contrast, $\text{Ru}(\text{NH}_6)_6^{3+/2+}$ and $\text{Co}(\text{phen})_3^{3+/2+}$ (phen = 1,10-phenanthroline) with larger λ values of 1.4 and 1.6 eV, respectively, require a narrower gap of <5 nm, where the tip current may be significantly biased by electron tunneling between the tip and the substrate.⁴³ Also, $\text{Ru}(\text{bpy})_2^{3+/2+}$ (bpy = 2,2'-bipyridyl) and $\text{Fe}(\text{phen})_2^{3+/2+}$ with small λ values of 0.5 and 0.6 eV, respectively, need short tip–substrate distances of <5 nm because of their high intrinsic reactivity, which varies with defect density at the HOPG surface.⁴⁴

In contrast, conventional cyclic voltammetry does not allow for the observation of the potential-independent kinetics of slow outer-sphere ET reactions at HOPG or other macroscopic electrodes.⁴⁵ To demonstrate this limitation, simulated substrate CVs based on the MHC mechanism were fitted with broad experimental CVs of the $\text{Fe}(\text{CN})_6^{3-/4-}$ couple at macroscopic HOPG electrodes reported in the seminal work by McCreery and co-workers.⁴⁴ For instance, the best fit for a CV at 10 V/s was obtained using $\lambda^* = 32$ ($\lambda = 0.82$ eV at 298 K) and $k^0 = 5.6 \times 10^{-6}$ cm/s while the totally irreversible CV based on BV kinetics with $\alpha = 0.5$ is much narrower (Figure 3-6). The fit as obtained using the MHC formalism is as good as demonstrated in the McCreery's work by assuming the linear potential-dependence of α in the BV model. In fact, the MHC formalism gives a linear relationship between E_s and apparent transfer coefficient, α_{app} , (see inset of Figure 6), when α_{app} is defined as⁴⁶

$$\alpha_{\text{app}} = -\frac{RT \ln(k_{\text{S,f}} / k^0)}{F(E_s - E^{0'})} = 1 - \frac{RT \ln(k_{\text{S,b}} / k^0)}{F(E_s - E^{0'})} \quad (19)$$

In eq 18 with the MHC formalism, $\lambda^* = 32$ corresponds to $d\alpha_{\text{app}}/dE_s = 0.25 \text{ V}^{-1}$ as found in the original work from the analysis of the experimental CV in Figure 3-5.⁴⁴ This linear relationship, however, is compromised as E_s approaches to the region where k_{lim} is achieved. Therefore, the linear potential-dependence of α_{app} , which has been also reported for various electrode reactions and interpreted by the classical Marcus theory with an inverted region,⁴⁶⁻⁴⁹ indicates that k_{lim} has not been reached without a diffusion limit under moderate mass transport conditions at macroscopic substrates. In fact, the range of

substrate potentials swept in Figure 6 is much narrower than required for achieving k_{lim} for $\lambda^* = 32$, which corresponds to $|E_s - E^{0'}| \geq 1.3$ V in eq 9 at 298 K. These results support that higher mass transport conditions in nanoscale $i_T - E_s$ voltammetry are required for the experimental observation of a kinetic limiting current.

Alternatively, nanoscale mass transport is achieved at the nanometer-sized basal plane surface of HOPG, which is difficult to prepare without the serious formation of defects.²⁴

In addition to the MHC effect, the diffusional effect is likely to play a role in broadening of CVs at HOPG. Experimental CVs of the $\text{Fe}(\text{CN})_6^{3-/4-}$ couple are significantly broader than CVs simulated with a λ^* value of 51 as theoretically estimated for HOPG although smaller λ^* values of 27–44 ($\lambda = 0.7$ –1.13 eV) were experimentally determined for other systems (Table 3-1). This result suggests that the experimental CVs are broadened due to the diffusional effect within various domains at the heterogeneous surface of HOPG as quantitatively assessed using diffusion domain approach.⁵⁰ In fact, the limitation of HOPG in the reproducible experimental test of the MHC formalism is the large variation of grain size and structure among samples even from the same source as confirmed by focused-ion-beam imaging of their surfaces.⁵¹

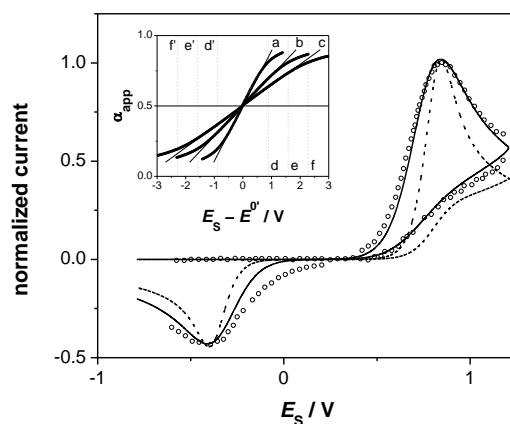


Figure 3-6. Experimental CV (circles) of $\text{Fe}(\text{CN})_6^{4-}$ at the low defect basal plane surface of HOPG at $\nu = 10$ V/s read from the original CV in ref. 44 using Engauge Digitizer (<http://digitizer.sourceforge.net/>). Solid and dotted

lines represent simulated CVs based on MHC ($\lambda^* = 32$, $k^0 = 5.6 \times 10^{-6}$ cm/s, and $E^0 = 0.21$ V) and BV ($\alpha = 0.5$, $k^0 = 5.0 \times 10^{-7}$ cm/s, and $E^0 = 0.22$ V) kinetics, respectively. The inset shows α_{app} (circles) calculated from eq 19 with the MHC formalism for $\lambda^* =$ (a) 20, (b) 40, and (c) 60 using Mathematica. Linear regions are represented by solid lines with $d\alpha_{\text{app}}/dE = 0.397$, 0.215, and 0.148, respectively, and the intercept at $\alpha_{\text{app}} = 0.5$. Dotted lines in the inset indicate substrate potentials where 99 % of k_{lim} is achieved for $\lambda^* =$ (d, d') 20, (e, e') 40, and (f, f') 60 at 298 K (see eq 9).

3.4 CONCLUSIONS

Here we employed the MHC formalism to theoretically predict that MHC voltammetric behavior will be manifested by SECM-based $i_{\text{T}}-E_{\text{S}}$ voltammetry under nanoscale mass transport conditions. Our voltammetric theory is generally applicable to any steady-state and quasi-steady-state condition with arbitrary substrate potential and both feedback and SG/TC modes. Therefore, this deviation from the classical BV model should be considered for the comprehensive range of nanoscale SECM measurements except for fastest heterogeneous ET reactions reported so far ($k^0 > 1$ cm/s).^{10, 22} Our prediction is also extended to steady-state voltammetry of ET reactions at nanometer-sized SECM tips positioned above conductors¹¹ because tip voltammetry can be well described by the general theory⁵² that is analogous to the theory for $i_{\text{T}}-E_{\text{S}}$ voltammetry.²¹ In comparison to nanotips,¹⁰ macroscopic substrates can be fabricated from a much larger variety of electroactive materials to be investigated by SECM, thereby augmenting the significance of our theory.

Steady-state and quasi-steady-state MHC responses in $i_{\text{T}}-E_{\text{S}}$ voltammetry are recognized not only as a broad wave shape but also as a kinetically limited plateau current, which contrasts to classical Marcus "inverted" behavior. The experimental observation of a limiting ET rate constant without a diffusion limit will be possible under high mass transport conditions as achieved at nanoscale tip–substrate gaps in SECM. On the other hand, our theory indicates that the broad wave shape of a MHC response corresponds to the

linear potential-dependence of apparent transfer coefficient in the BV model as observed with various macroscopic electrodes and interpreted by the classical Marcus theory.⁴⁶⁻⁴⁹ Importantly, this linear potential-dependence is the evidence that a limiting ET rate constant due to the MHC mechanism is not reached. In addition, the erroneous analysis of a broad i_T-E_S voltammogram using the BV model can be avoided by measuring a pair of voltammograms in feedback and SG/TC modes, which display inversion symmetry as another important feature of MHC voltammetric behavior under steady-state and quasi-steady-state conditions.

No prior knowledge of the rate law is required for the analysis of the retraceable portion of an i_T-E_S voltammogram, which can be directly converted to a plot of ET rate constant versus substrate potential using analytical equations developed in this work. A pair of such plots thus obtained from a pair of i_T-E_S voltammograms in feedback and SG/TC modes reveal the potential dependence of ET rate constants for both anodic and cathodic processes at the substrate. This analytical approach facilitates applications of i_T-E_S voltammetry to non-BV systems based on electrocatalysis,⁵³ charge-transfer at liquid/liquid interfaces,⁵⁴ nanoparticle-mediated ET at gold electrodes modified with self-assembled monolayers,⁵⁵ and ET at single-walled carbon nanotubes and graphenes.²⁸ In fact, nanoscale mass transport is inevitable when individual single-walled carbon nanotubes are investigated as SECM substrates.²⁰

3.5 SUPPORTING INFORMATION

Supporting Information includes results of finite element simulation, the derivation and assessment of analytical equations, and reaction parameters for various outer-sphere redox couples at HOPG and other macroscopic electrodes.

3.5.1 Finite Element Simulation

An SECM diffusion problem was solved in a dimensionless form by employing the finite element method as reported elsewhere.⁵⁶ A tip current, i_T , was normalized with respect to a limiting current at an

inlaid disk tip in the bulk solution, $i_{T(\infty)}$, to obtain a dimensionless tip current, I_T , as

$$I_T(L, E_S) = \frac{i_T}{i_{T(\infty)}} = \frac{2\pi}{x} \int_0^1 R \left[\frac{\partial C_O(R, L, \tau)}{\partial Z} \right] dR \quad (20)$$

With⁵⁷

$$x = 1 + 0.639 \left[1 - \frac{2}{\pi} \arccos \left(\frac{1}{RG} \right) \right] - 0.186 \left\{ 1 - \left[\frac{2}{\pi} \arccos \left(\frac{1}{RG} \right) \right]^2 \right\} \quad (21)$$

The simulation results discussed in the main text are shown in Figures 2-7, 2-9, 2-10, and 2-11.

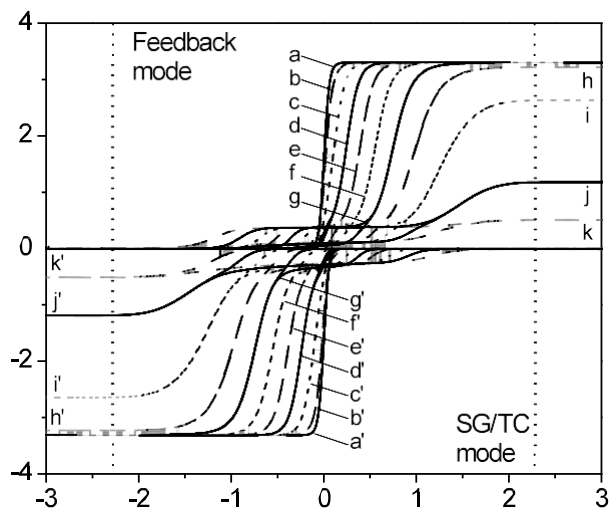


Figure 3-7. Simulated $i-E$ voltammograms based on the MHC formalism with $\lambda^* = 60$ and $\log =$ (a, a') 1, (b, b') 0, (c, c') -1, (d, d') -2, (e, e') -3, (f, f') -4, (g, g') -5, (h, h') -6, (i, i') -7, (j, j') -8, and (k, k') -9. Dotted lines correspond to substrate potentials where 99 % of k_{lim} is achieved at 298 K (see eq 9).

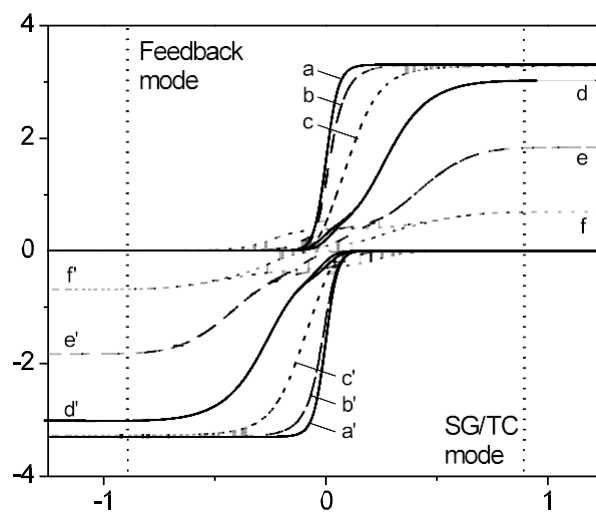
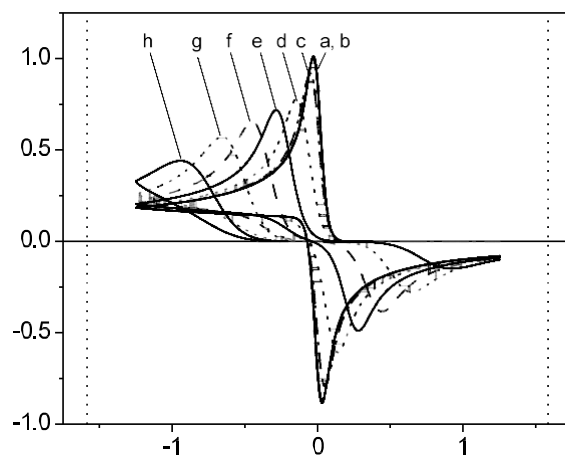


Figure 3-8. Simulated $i-E$ voltammograms based on the MHC formalism with $\lambda^* = 20$ and $\log \lambda'_0 = (a, a')$ 1, (b, b') 0, (c, c') -1, (d, d') -2, (e, e') -3, and (f, f') -4. Dotted lines correspond to substrate potentials where 99 % of k_{lim} is achieved at 298 K (see eq 9).

(a)



(b)

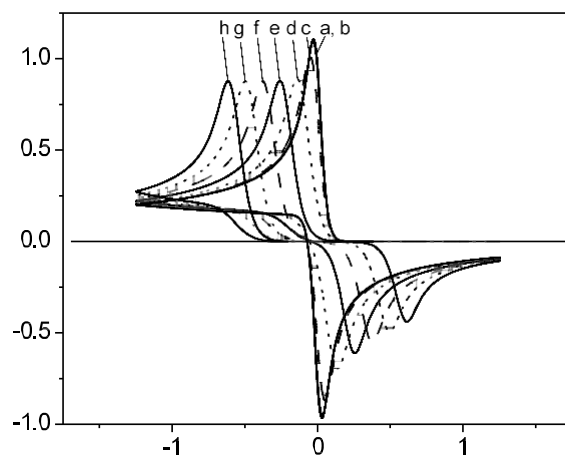


Figure 3-9. Simulated substrate CVs based on (a) MHC formalism with $\lambda^* = 40$ and (b) BV formalism with $\alpha = 0.5$; $\log \lambda'_0 =$ (a) 1, (b) 0, (c) -1, (d) -2, (e) -3, (f) -4, (g) -5, and (h) -6. Curves a and b are reversible and overlap with each other. Dotted lines correspond to substrate potentials where 99 % of k_{lim} is achieved at 298 K (see eq 9).

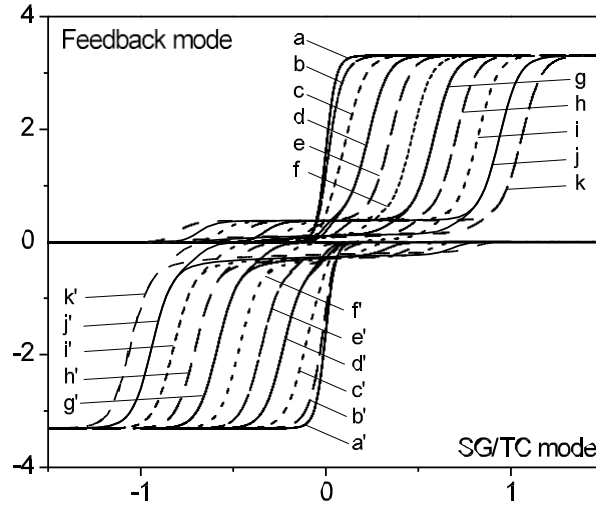


Figure 3-10. Simulated i_T-E_S voltammograms based on BV kinetics with $\alpha = 0.5$ and $\log \lambda'_0 = (a, a')$ 1, (b, b') 0, (c, c') -1, (d, d') -2, (e, e') -3, (f, f') -4, (g, g') -5, (h, h') -6, (i, i') -7, (j, j') -8, and (k, k') -9.

3.5.2 Analytical Equation for Irreversible Substrate Reactions (Eq 15)

Eq 15 was used together with the following equations to calculate the retraceable portion of an i_T-E_S voltammogram when a substrate reaction is totally irreversible under the tip and opposite to the tip reaction (Figure 2-11).⁵⁷

$$I_{T,NF}(L, RG) = \frac{\frac{2.08}{RG^{0.358}} \left(L - \frac{0.145}{RG} \right) + 1.585}{\frac{2.08}{RG^{0.358}} (L + 0.0023RG) + 1.57 + \frac{\ln RG}{L} + \frac{2}{\pi RG} \ln(1 + \pi RG / 2L)} \quad (22)$$

$$I_{T,PF}(L, RG) = \alpha(RG) + \frac{\pi}{4x \arctan(L)} + \left[1 - \alpha(RG) - \frac{1}{2x} \right] \frac{2}{\pi} \arctan(L) \quad (23)$$

With

$$\alpha(RG) = \ln 2 + \ln 2 \left[1 - \frac{2}{\pi} \arctan \left(\frac{1}{RG} \right) \right] - \ln 2 \left\{ 1 - \left[\frac{2}{\pi} \arctan \left(\frac{1}{RG} \right) \right]^2 \right\} \quad (24)$$

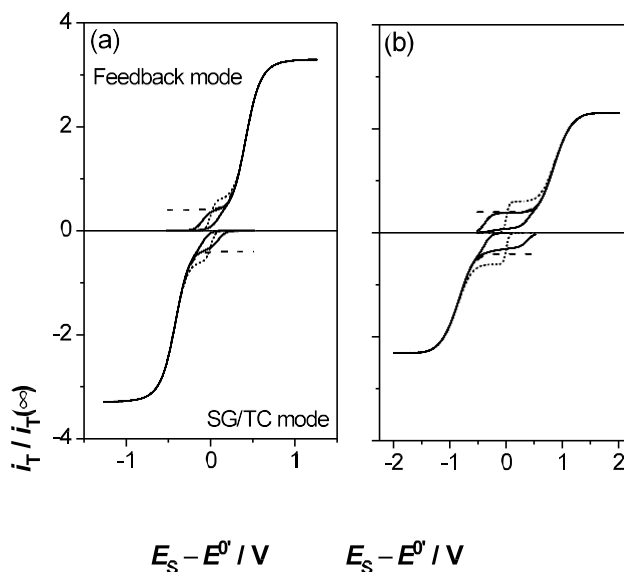


Figure 3-11. Simulated $i_T - E_S$ voltammograms based on the MHC formalism (solid lines) with $\lambda^* = 40$ and $\lambda'_0 =$ (a) 1×10^{-3} and (b) 1×10^{-5} . Dashed and dotted lines represent $i_T - E_S$ voltammograms calculated using eqs 15 and 17 (or 18), respectively.

3.5.3 Analytical Equations for Quasi-Steady-State $i_T - E_S$ Voltammograms (Eqs 17 and 18)

Eqs 17 and 18 are valid under steady-state and quasi-steady-state conditions (Figure 2-11), which are achieved when the reaction at the surface of a macroscopic substrate except under the tip is reversible or diffusion-limited as discussed in the main text. These analytical equations were derived using a model for an SECM-based thin layer cell as reported elsewhere.⁵⁶ In contrast to a BV response, a limiting current based on the MHC mechanism can be controlled by ET kinetics rather than by mediator diffusion. To account for this difference, the normalized kinetic limiting current, $I_{T,lim}(L)$, and the corresponding limiting rate constant, k_{lim} , were introduced in eqs 17 and 18 to replace the diffusion-limited positive-feedback current at a tip, $I_{T,d}(L)$ ($= I_{T,PF}(L)$), in the original equations based on BV

kinetics.⁵⁶ Eqs 17 and 18 are equivalent to the BV counterparts when $k_{\text{lim}} \rightarrow \infty$ and, subsequently, $I_{\text{T,lim}}(L)$
($=I_{\text{T,d}}(L)$).

Table 3-1 Reaction Parameters and Requirements for Observing a Kinetic Limiting Current at HOPG

redox couple	λ eV (λ^{*a})	k^0 cm/s ^b	k_{lim} cm/s ^c	$I_{T,lim}/I_{T,PF}$ at $L = 0.25^d$		E^0 V ^{b,e}	$ E_s - E^0 $ V ^f
				$d = 5$ nm	$d = 50$ nm		
Ru(bpy) ₂ ^{3+/2+}	0.5 (19) ^g	$>2.0 \times 10^{-2}$	$>1.4 \times 10$	>0.67	>0.90	1.04	0.87
	0.56 (22) ^h		$>2.7 \times 10$	>0.78	>0.94		
Fe(phen) ₃ ^{3+/2+}	0.6 (23) ^g	$>7.0 \times 10^{-2}$	$>1.4 \times 10^2$	>0.95	>0.99	0.86	1.01
MV ^{2+/+}	0.6 (23) ^g	1.7×10^{-2}	3.5×10	0.82	0.96	-0.67	1.01
IrCl ₆ ^{2-/3-}	0.8 (31) ^g	3.0×10^{-3}	4.9×10	0.86	0.97	0.74	1.28
Fc(COOH) ₂ ⁺⁰	0.8 (31) ^g	3.0×10^{-3}	4.9×10	0.86	0.97	0.42	1.28
W(CN) ₈ ^{3-/4-}	0.9 (35) ^g	4.0×10^{-4}	1.8×10	0.71	0.92	0.33	1.41
	0.87 (34) ⁱ		1.3×10	0.65	0.90		
	1.0 (39) ⁱ		5.0×10	0.87	0.97		
	0.69 (27) ^j		2.1	0.31	0.60		
Ru(CN) ₆ ^{3-/4-}	1.0 (39) ^g	4.0×10^{-4}	5.0×10	0.87	0.97	0.78	1.55
	0.78 (30) ^j		5.3	0.47	0.78		
Fe(CN) ₆ ^{3-/4-}	1.3 (51) ^g	1.0×10^{-6}	2.6	0.35	0.65	0.25	1.95
	1.13 (44) ^h		9.4×10^{-1}	0.18	0.33		
	0.78 (30) ^{j,k}		1.3×10^{-2}	0.12	0.13		
	0.7 (27) ^{j,l}		5.8×10^{-3}	0.12	0.13		
Ru(NH ₆) ₆ ^{3+/2+}	1.4 (54) ^g	9.0×10^{-4}	6.5×10^3	1.0	1.0	-0.19	2.09
	1.3 (51) ⁱ		2.4×10^3	1.0	1.0		
	1.6 (62) ⁱ		4.8×10^4	1.0	1.0		
	0.58 (23) ^j		1.5	0.27	0.53		
Co(phen) ₃ ^{3+/2+}	1.6 (62) ^g	2.0×10^{-5}	1.1×10^3	0.99	1.0	0.10	2.36
	1.48 (58) ^j		3.2×10^2	0.98	1.0		

a At 298 K. b Voltammetrically determined for HOPG in ref. 58. c From eq 8. d From eq 15. e Approximate values against SCE as obtained by averaging voltammetric peak potentials on laser-activated glassy carbon electrodes. f Substrate potentials where 99 % of k_{lim} is achieved at 298 K (see eq 9). g Theoretically estimated for HOPG in ref. 59. h Experimentally determined for SAM-modified gold electrodes in ref. 60. i Experimentally determined for SAM-modified gold electrodes in ref. 61. j Values in aqueous solutions calculated from photoelectron emission threshold energies in ref. 62. k For ferrocyanide. l For ferricyanide.

ACKNOWLEDGMENTS

This work was supported by a CAREER award from the National Science Foundation (Grant CHE-0645623).

3.6 REFERENCES

- (1) Bard, A. J.; Mirkin, M. V., Eds. *Scanning Electrochemical Microscopy*; Marcel Dekker: New York, 2001.
- (2) Amemiya, S.; Bard, A. J.; Fan, F.-R. F.; Mirkin, M. V.; Unwin, P. R. *Ann. Rev. Anal. Chem.* **2008**, *1*, 95.
- (3) Kwak, J.; Bard, A. J. *Anal. Chem.* **1989**, *61*, 1221.
- (4) Cornut, R.; Lefrou, C. *J. Electroanal. Chem.* **2008**, *621*, 178.
- (5) Xiong, H.; Guo, J.; Amemiya, S. *Anal. Chem.* **2007**, *79*, 2735.
- (6) Zhang, J.; Slevin, C. J.; Morton, C.; Scott, P.; Walton, D. J.; Unwin, P. R. *J. Phys. Chem. B* **2001**, *105*, 11120.
- (7) Wei, C.; Bard, A. J.; Mirkin, M. V. *J. Phys. Chem.* **1995**, *99*, 16033.
- (8) Liu, B.; Rotenberg, S. A.; Mirkin, M. V. *Proc. Natl. Acad. Sci. U.S.A.* **2000**, *97*, 9855.
- (9) Murray, R. W. *Chem. Rev.* **2008**, *108*, 2688.
- (10) Wang, Y. X.; Velmurugan, J.; Mirkin, M. V. *Isr. J. Chem.* **2010**, *50*, 291.
- (11) Sun, P.; Mirkin, M. V. *Anal. Chem.* **2006**, *78*, 6526.
- (12) Velmurugan, J.; Sun, P.; Mirkin, M. V. *J. Phys. Chem. C* **2008**, *113*, 459.
- (13) Bi, S.; Liu, B.; Fan, F.-R. F.; Bard, A. J. *J. Am. Chem. Soc.* **2005**, *127*, 3690.
- (14) Fan, F.-R. F.; Bard, A. J. *Science* **1995**, *267*, 871.
- (15) Fan, F.-R. F.; Kwak, J.; Bard, A. J. *J. Am. Chem. Soc.* **1996**, *118*, 9669.
- (16) Sun, P.; Mirkin, M. V. *J. Am. Chem. Soc.* **2008**, *130*, 8241.
- (17) Xiong, H.; Gross, D. A.; Guo, J.; Amemiya, S. *Anal. Chem.* **2006**, *78*, 1946.
- (18) Kim, E.; Kim, J.; Amemiya, S. *Anal. Chem.* **2009**, *81*, 4788.
- (19) Xiong, H.; Kim, J.; Kim, E.; Amemiya, S. *J. Electroanal. Chem.* **2009**, *629*, 78.
- (20) Kim, J.; Xiong, H.; Hofmann, M.; Kong, J.; Amemiya, S. *Anal. Chem.* **2010**, *82*, 1605.
- (21) Nioradze, N.; Kim, J.; Amemiya, S. *Anal. Chem.* **2011**, *83*, 828.

- (22) White, R. J.; White, H. S. *Anal. Chem.* **2005**, *77*, 214A.
- (23) Chidsey, C. E. D. *Science* **1991**, *251*, 919.
- (24) Feldberg, S. W. *Anal. Chem.* **2010**, *82*, 5176.
- (25) Oldham, K. B.; Myland, J. C. *J. Electroanal. Chem.* **2011**, *655*, 65.
- (26) Tender, L.; Carter, M. T.; Murray, R. W. *Anal. Chem.* **1994**, *66*, 3173.
- (27) Forster, R. J.; Loughman, P.; Keyes, T. E. *J. Am. Chem. Soc.* **2000**, *122*, 11948.
- (28) Heller, I.; Kong, J.; Williams, K. A.; Dekker, C.; Lemay, S. G. *J. Am. Chem. Soc.* **2006**, *128*, 7353.
- (29) Becka, A. M.; Miller, C. J. *J. Phys. Chem.* **1992**, *96*, 2657.
- (30) McCreery, R. L. *Chem. Rev.* **2008**, *108*, 2646.
- (31) Feldberg, S. W.; Sutin, N. *Chem. Phys.* **2006**, *324*, 216.
- (32) Lefrou, C. *J. Electroanal. Chem.* **2006**, *592*, 103.
- (33) Royea, W. J.; Hamann, T. W.; Brunschwig, B. S.; Lewis, N. S. *J. Phys. Chem. B* **2006**, *110*, 19433.
- (34) Terrettaz, S.; Becka, A. M.; Traub, M. J.; Fettinger, J. C.; Miller, C. J. *J. Phys. Chem.* **1995**, *99*, 11216.
- (35) Gorelsky, S. I.; Kotov, V. Y.; Lever, A. B. P. *Inorg. Chem.* **1998**, *37*, 4584.
- (36) Rodgers, P. J.; Amemiya, S.; Wang, Y.; Mirkin, M. V. *Anal. Chem.* **2010**, *82*, 84.
- (37) Wang, Y.; Velmurugan, J.; Mirkin, M. V.; Rodgers, P. J.; Kim, J.; Amemiya, S. *Anal. Chem.* **2010**, *82*, 77.
- (38) Wang, Y.; Kakiuchi, T.; Yasui, Y.; Mirkin, M. V. *J. Am. Chem. Soc.* **2010**, *132*, 16945.
- (39) Bard, A. J.; Faulkner, L. R. *Electrochemical Methods: Fundamentals and Applications*, 2nd ed.; John Wiley & Sons: New York, 2001, p. 571.
- (40) Kneten, K. R.; McCreery, R. L. *Anal. Chem.* **1992**, *64*, 2518.
- (41) Cline, K. K.; McDermott, M. T.; McCreery, R. L. *J. Phys. Chem.* **1994**, *98*, 5314.

- (42) McCreery, R. L.; Cline, K. K. In *Laboratory Techniques in Electroanalytical Chemistry*; Kissinger, P. T., Heineman, W. R., Eds.; Marcel Dekker: New York, 1996, pp 293.
- (43) White, R. J.; White, H. S. *Langmuir* **2008**, *24*, 2850.
- (44) McDermott, M. T.; Kneten, K.; McCreery, R. L. *J. Phys. Chem.* **1992**, *96*, 3124.
- (45) Richardson, J. N.; Harvey, J.; Murray, R. W. *J. Phys. Chem.* **1994**, *98*, 13396.
- (46) Weaver, M. J.; Anson, F. C. *J. Phys. Chem.* **1976**, *80*, 1861.
- (47) Parsons, R.; Passerox, E. *J. Electroanal. Chem.* **1966**, *12*, 524.
- (48) Savéant, J. M.; Tessier, D. *J. Electroanal. Chem.* **1975**, *65*, 57.
- (49) Corrigan, D. A.; Evans, D. H. *J. Electroanal. Chem.* **1980**, *106*, 287.
- (50) Davies, T. J.; Moore, R. R.; Banks, C. E.; Compton, R. G. *J. Electroanal. Chem.* **2004**, *574*, 123.
- (51) Park, S.; Floresca, H. C.; Suh, Y.; Kim, M. J. *Carbon* **2010**, *48*, 797.
- (52) Zoski, C. G.; Luman, C. R.; Fernandez, J. L.; Bard, A. J. *Anal. Chem.* **2007**, *79*, 4957.
- (53) Fernandez, J. L. *J. Electroanal. Chem.* **2010**, *650*, 90.
- (54) Girault, H. H. In *Electroanalytical Chemistry*; Bard, A. J., Zoski, C. G., Eds.; Taylor & Francis: Boca Raton, 2010; Vol. 23, pp 1.
- (55) Bradbury, C. R.; Zhao, J.; Fermín, D. J. *J. Phys. Chem. C* **2008**, *112*, 10153.
- (56) Lefrou, C. *J. Electroanal. Chem.* **2006**, *592*, 103.
- (57) Cornut, R.; Lefrou, C. *J. Electroanal. Chem.* **2008**, *621*, 178.
- (58) Cline, K. K.; McDermott, M. T.; McCreery, R. L. *J. Phys. Chem.* **1994**, *98*, 5314.
- (59) Royea, W. J.; Hamann, T. W.; Brunschwig, B. S.; Lewis, N. S. *J. Phys. Chem. B* **2006**, *110*, 19433
- (60) Terrettaz, S.; Becka, A. M.; Traub, M. J.; Fettingner, J. C.; Miller, C. J. *J. Phys. Chem.* **1995**, *99*, 11216.
- (61) Becka, A. M.; Miller, C. J. *J. Phys. Chem.* **1992**, *96*, 2657.

(62) Gorelsky, S. I.; Kotov, V. Y.; Lever, A. B. P. *Inorg. Chem.* **1998**, *37*, 4584.

4.0 ORIGINS OF NANOSCALE DAMAGE TO GLASS SEALED PLATINUM ELECTRODES WITH SUBMICROMETER AND NANOMETER SIZE

This work has been published as Nikoloz Nioradze, Ran Chen, Jiyeon Kim, Mei Shen, Padmanabhan Santhosh, and Shigeru Amemiya, Origins of Nanoscale Damage to Glass-Sealed Platinum Electrodes with Submicrometer and Nanometer Size, *Anal. Chem.* **2013**, 85, 6198–6202. The thesis author nanofabricated electrodes, collected and analyzed experimental data.

4.1 INTRODUCTION

Glass-sealed Pt electrodes with submicrometer and nanometer size have been successfully developed and applied for nanoscale electrochemical measurements such as scanning electrochemical microscopy (SECM). These small electrodes, however, are difficult to work with because they often lose a current response or give a low SECM feedback in current–distance curves. Here we report that these problems can be due to the nanometer-scale damage that is readily and unknowingly made to the small tips in air by electrostatic discharge or in electrolyte solution by electrochemical etching. The damaged Pt electrodes are recessed and contaminated with removed electrode materials to lower their current responses. The recession and contamination of damaged Pt UMEs are demonstrated by scanning electron microscopy and X-ray energy dispersive spectroscopy. The recessed geometry is noticeable also by SECM, but is not obvious from a cyclic voltammogram. Characterization of a damaged Pt electrode with recessed geometry only by cyclic voltammetry may underestimate electrode size from a lower limiting current owing to invalid assumption of inlaid disk geometry. Significantly, electrostatic damage can be avoided by grounding a Pt electrode and nearby objects, most importantly, an operator as a source of electrostatic charge. Electrochemical damage can be avoided by maintaining potentiostatic control of a Pt electrode without internally disconnecting the electrode from a potentiostat between voltammetric

measurements. Damage-free Pt electrodes with submicrometer and nanometer size are pivotal for reliable and quantitative nanoelectrochemical measurements.

Recently, significant progresses have been made for miniaturization of glass-sealed Pt ultramicroelectrodes (UMEs) to submicrometer and nanometer size.¹⁻⁴ These small Pt UMEs offer extremely high spatial and temporal resolutions for electrochemical measurement such as scanning electrochemical microscopy (SECM).^{5,6} Submicrometer- or nanometer-size Pt UMEs can be successfully prepared by heat-pulling a glass-sealed Pt microwire⁷ or by heat-sealing a sharply etched Pt wire into a glass capillary.⁸ The tip end of the Pt-glass composite is mechanically polished to expose the Pt disk surrounded by a relatively thick glass sheath⁹⁻¹⁴ ($3 < RG < 10$, where RG is the ratio of the radius of the glass sheath, r_g , divided by the electrode radius, a). The heat-pulling/mechanical-polishing approach has been successful also for fabrication of Au¹⁵ and Ag¹⁶ nanodisk electrodes. Moreover, molecularly small Pt UMEs with $a = 1-3$ nm can be obtained by heat-pulling the Pt microwire sealed in a thick-wall glass tube with $RG \gg 10$.¹⁷ On the other hand, a disk UME with $RG < 3$ is often desirable for SECM because such a sharp tip can be positioned closer to a substrate.¹⁸⁻²¹ For this purpose, the tapered end of a glass-sealed Pt UME with $RG > 3$ is heated to melt glass and pull it away from the Pt tip.⁸ The exposed Pt tip is polished mechanically^{8,22} or milled by using focused ion-beam (FIB) technology^{23,24} to obtain a submicrometer-size Pt UME with $RG < 3$.

In this work, we report for the first time that glass-sealed Pt UMEs with submicrometer and nanometer size can be readily and unknowingly damaged at the nanoscale to significantly lower their current responses. Such a small UME can be damaged in air by electrostatic discharge (ESD) to recess the Pt tip and, subsequently, contaminate it with removed Pt and glass. In addition, submicrometer- and nanometer-size Pt UMEs can be electrochemically etched in electrolyte solution and contaminated with the Pt nanoparticles removed from the tip at the beginning or end of voltammetric/ampereometric measurement when connection of the UMEs to a potentiostat is internally switched on or off, respectively. Recession and contamination owing to electrostatic and electrochemical damage can be a

reason why nanoelectrodes often lose a current response¹⁹ or give a low SECM feedback in current–distance curves (i.e., approach curves).²⁵ In fact, a recent AFM study showed recession of glass-sealed Pt nanoelectrodes and contamination of both Pt and glass surfaces with nanoparticles.²⁵ An origin of recession or contamination of the nanoelectrodes, however, was not identified.

4.2 ELECTROSTATIC DISCHARGE AND PROTECTION AGAINST IT

Importantly, nanometer-scale damage to a glass-sealed Pt UME in air can be avoided by employing appropriate ESD protections (Supporting Information), thereby confirming that ESD causes electrode damage. The ESD protections are based on grounding of both a UME and any object that contacts with or exists near the UME. Subsequently, no ESD occurs between the UME and the isopotential object. In our laboratory environments, ESD damage to a Pt UME is seen by scanning electron microscopy (SEM) when an operator does not wear the wrist strap, gloves and lab coat that are conductive and grounded. Without any ESD protection, a human body accumulates a high electrostatic charging voltage of 10–20 kV.²⁶ Overall, injection of electrostatic charge from an operator into a UME is followed by ESD from the sharp Pt tip to a nearby object, which damages the tip.

4.3 EXPERIMENTAL SECTION

4.3.1 Electrode Fabrication and Characterization

We used borosilicate-sealed Pt UMEs with submicrometer size (Figure 4-1A) to resolve ESD damage on the Pt and glass surfaces by SEM. These UMEs with small RG of ~ 2 were fabricated as SECM tips by heat-pulling, heat-annealing, and FIB milling as described above (Supporting Information). We found that ESD damage was made to the Pt UMEs sealed in borosilicate,²⁴ Pb-doped,²³ and aluminosilicate glasses. The damage was less severe with borosilicate glass probably because of its higher conductivity. Noticeably, borosilicate glass has been most widely used to fabricate submicrometer- and nanometer-size Pt UMEs,^{7-9,11,13,15,16,22,24} Quartz-sealed Pt UMEs^{10,13,14} are beyond the scope of this study

and were not tested because quartz cannot be heat annealed using a microforge^{23,24} (MF-900, Narishige, Tokyo, Japan) to reduce *RG* for SECM applications.

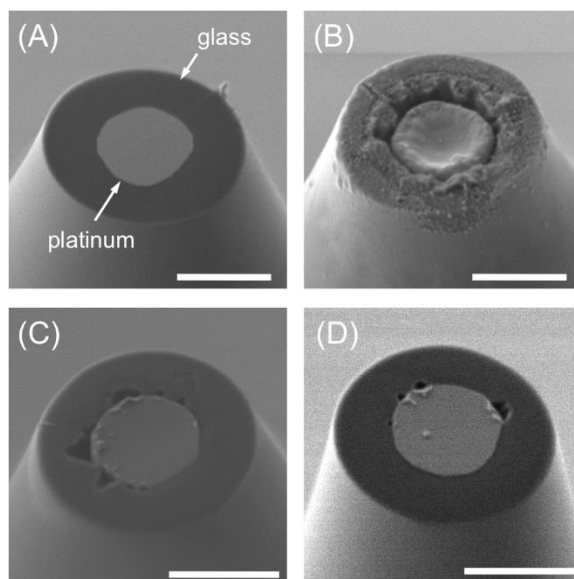


Figure 4-1. SEM images of a borosilicate-sealed Pt UME (A) before and (B) after ESD damage. Parts (C) and (D) show moderately and weakly damaged Pt UMEs, respectively. Scale bars are 1 μm .

4.3.2 Electrostatic Discharge Caused by an Operator.

ESD damage to a glass-sealed Pt UME cannot be completely avoided without the ESD protections although the damage depends on laboratory environmental conditions and operators. Severe damage was made to the tip end (Figure 4-1B) when the contact wire of a submicrometer-size Pt UME with well-defined geometry (Figure 4-1A) was touched by the bare hand of an operator without the ESD protections. The operator does not see, hear, or even feel the ESD, which caused the severe tip damage. The ESD-damaged Pt tip was recessed and its periphery was deformed. Moreover, the surrounding glass sheath was fractured and deformed. Deformation of glass near the Pt tip suggests that ESD melted glass.

The severely damaged boundary between Pt and glass was seen as a dark ring by optical microscopy using a 50× objective lens. Less severe damage (Figure 4-1C and D) was made during summer because of higher humidity or by an operator with less electrostatic charging voltage, which varies with the type of clothing, shoes, etc.²⁶ The weak damage (Figure 4-1D) was caused by handling the tip using ESD-protected tweezers without the other ESD protections. The localization of weak damage at glass near the Pt tip suggests that ESD occurs most extensively at the Pt/glass boundary. Severe damage results from accumulation of moderate or weak ESD damage by repetitive contact with an ESD-unprotected operator.

The severely ESD-damaged UME (Figure 4-1B) gave a poor SECM approach curve with a low feedback response at a Au substrate (Figure 4-2) as expected for a recessed UME.^{25,27} The tip current, i_T , based on diffusion-limited oxidation of ferrocenemethanol (FcMeOH) increased only up to ~2.5 times of the limiting current in the bulk solution, $i_{T,\infty}$, before the glass sheath of the Pt tip contacted the Au substrate. The contact is indicated by the inflection point of the approach curve. The normalized experimental curve is too broad to fit with the theoretical curve based on diffusion-limited positive feedback at an inlaid disk tip²⁸ (Figure 4-2). Such a broad approach curve with small positive feedback effect is expected for a recessed UME.²⁷ Noticeably, recession of the damaged tip is not obvious from its excellent steady-state CV (the inset of Figure 4-2). Without SEM or SECM characterization, inlaid disk geometry may be assumed to unknowingly underestimate the radius of the damaged electrode from its $i_{T,\infty}$ using the following equation

$$i_{T,\infty} = 4xnFD_w c^* a \quad (1)$$

where x is a function of RG ,^{29,30} n is the number of transferred electrons (= 1) in the tip reaction, and D_w ($= 7.8 \times 10^{-6} \text{ cm}^2/\text{s}$)¹¹ and c^* ($= 0.5 \text{ mM}$) are the diffusion coefficient and concentration of FcMeOH in 0.1 M KCl. A limiting current at a recessed UME is lower than expected from eq 1 because of the extra diffusion path from the orifice to the recessed surface.³¹ In fact, eq 1 with an $i_{T,\infty}$ value of 64 pA at the damaged UME with $RG = 2.5$ (i.e., $x = 1.08$) gives a tip radius of 0.39 μm , which is smaller than an approximate radius of 0.47 μm as estimated from the SEM image of this UME before ESD

damage (Figure 4-1A). The underestimated tip radius also contributes to broadening of the experimental approach curve in the normalized form (Figure 4-2).

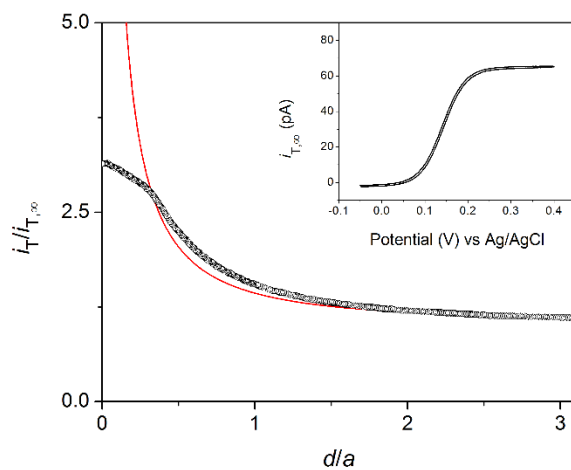


Figure 4-2. SECM approach curve (circles) at an unbiased Au substrate as obtained using the severely ESD-damaged Pt UME (its SEM image is shown in Figure 1B) with FcMeOH as a redox mediator. The tip potential was 0.35 V against a Ag/AgCl reference electrode. Tip scan rate, 19 nm/s. The red line represents a theoretical positive-feedback curve for an inlaid disk tip with $RG = 2.5$. The inset shows the CV of 0.5 mM FcMeOH at the damaged UME in 0.1 M KCl. Potential sweep rate, 20 mV/s.

Electrostatic damage is not due to the fragility of Pt UMEs after heat-annealing or FIB-milling. Severe ESD damage was also observed with a submicrometer-size Pt UME with a thicker glass sheath ($RG \sim 5$ in Figure 4-6A and B), which was FIB-milled without heat annealing. This result confirms that ESD damage is not due to a thin glass sheath or the fragility of Pt and glass stressed by heat annealing. Moreover, ESD damage was made to a Pt UME without heat annealing or FIB milling (Figure 4-6C and D). Upon ESD damage, the protrusion of the tapered Pt tip from the glass sheath was completely lost, which resulted in deep recession of the tip. Therefore, ESD damage is not caused by FIB milling although an FIB- milled surface may be more fragile owing to implantation of Ga^+ from the ion beam.³² Noticeably, a Pt UME was grounded to the sample stage of the FIB instrument to avoid the charging and ESD damage of the tip during milling.

More severe ESD damage was seen with a Pt nanoelectrode (Figure 4-3A and B before and after ESD damage, respectively). The ~ 110 nm-diameter Pt UME was prepared by sealing a Pt microwire into a thicker-wall glass tube ($RG \sim 10$) to avoid protrusion of an as-pulled Pt tip from the surrounding glass (see above). Then, the small Pt tip was exposed from the glass sheath by heat-annealing and was FIB-milled (Figure 4-3A). The ESD-damaged Pt nanotip was completely buried into the glass sheath (Figure 4-3B). The damaged nanoelectrode gave a $i_{T,\infty}$ value of only 1.0 pA for 0.5 mM FcMeOH in 0.1 M KCl (Figure 4-3C). When inlaid disk geometry is assumed, eq 1 with this current value gives a tip radius of 6.1 nm, which is ~ 9 times smaller than the radius of the Pt tip before ESD damage (Figure 4-3A). This result indicates that the size of a Pt nanoelectrode can be significantly underestimated from its limiting current when the electrode is unknowingly recessed owing to ESD damage.

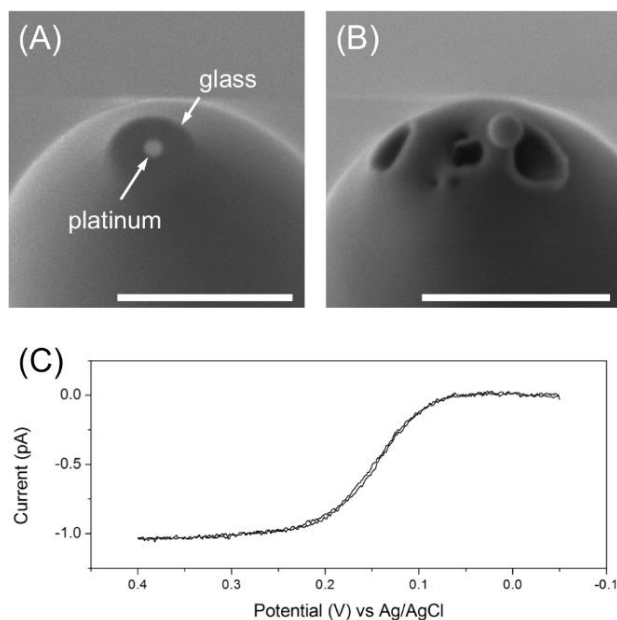


Figure 4-3. SEM images of a ~ 110 nm-diameter Pt nanoelectrode (A) before and (B) after ESD damage. Scale bars are 1 μm . (C) Background-subtracted CV of 0.5 mM FcMeOH in 0.1 M KCl as obtained using the ESD-damaged Pt nanoelectrode. Potential sweep rate, 5 mV/s.

4.3.3 Electrochemical Damage of Electrodes by Potentiostat

Finally, we report on the electrochemical damage made to a glass-sealed Pt UME. Specifically, a submicrometer-size Pt tip was etched and recessed during repetitive measurement of the CVs of FcMeOH in 0.1 M KCl when certain potentiostats (e.g., CHI 910B, CH Instruments, Austin, TX) were used to cycle tip potential between -0.05 and 0.4 V. Such damage was unexpected because even a Pt nanoelectrode is electrochemically stable in this potential range for FcMeOH oxidation.³³ Nevertheless, the SEM image of the Pt UME after measurement of the 38 CVs of FcMeOH (Figure 4-4A) shows ~ 200 nm-depth recession of the Pt tip with adsorbates on the surface of the glass sheath. X-ray EDS of the damaged tip confirmed that the adsorbates are the platinum nanoparticles etched away from the Pt tip (Figure 4-4B). The spatial resolution of X-ray EDS is high enough to resolve the Pt adsorbates on the glass surface from the central Pt region (see Supporting Information). These adsorbates are located near the Pt/glass boundary after measurement of less CVs. The nanometer-deep recession is not due to ESD because this UME was always handled with the ESD protections. Moreover, the features of ESD damage (Figure 3B–D) contrast to those of electrochemical damage, which shows uniform recession of the whole Pt surface and no fracture of the glass sheath at the boundary (Figure 4-4A).

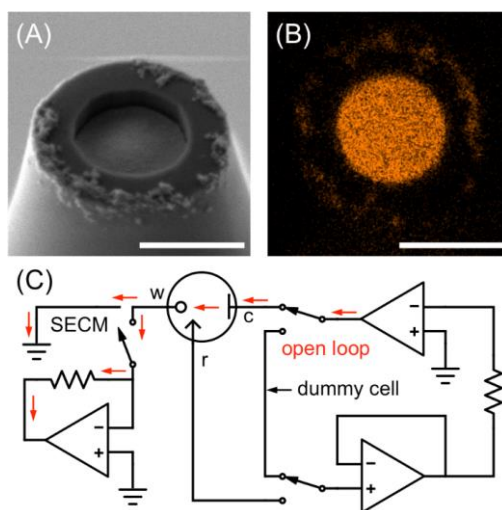


Figure 4-4. (A) SEM and (B) X-ray EDS images of a Pt UME after measurement of the 38 CVs of 0.5 mM FcMeOH in 0.1 M KCl. Scale bars are 1 μm . In the EDS image, orange dots indicate the presence of Pt. (C) Flow

of transient current through the Pt tip between ground and a saturated amplifier under an open-loop configuration at the beginning or end of CV measurement. Red arrows indicate current flow while w, r, and c represent working, reference, and counter electrodes.

A Pt UME is damaged transiently at the beginning (and end) of each CV measurement when the potentiostat is switched from an internal dummy cell to the electrochemical cell (and vice versa). In fact, electrochemical damage to a Pt UME was dramatically suppressed by maintaining internal connection of the potentiostat to the electrochemical cell between CV measurements. This can be achieved by activating the “cell on between runs” function of the potentiostat (see Supporting Information for details). In contrast, the Pt UME as shown in Figures 4-4A and B was electrochemically etched when this function was inactive (see also Supporting Information). This electrochemical damage may not be noticeable by SEM after a few potential cycles. An etching depth of ~5 nm per potential cycle is estimated from an etching depth of ~150 nm after 29 CVs.

The electrochemical etching of a Pt UME is due to the transient tip current driven by the saturation of a counter-electrode amplifier upon the connection of the potentiostat to the electrochemical cell (Figure 4-4C). The connection is established by turning on counter and reference electrodes, and then working electrode. Since electromechanical relays for counter and reference electrodes bounce and do not settle down immediately, the counter-electrode amplifier transiently experiences an open-loop configuration to give a large output voltage (~13 V). Subsequently, high transient current flows from the saturated amplifier to the Pt tip through the electrolyte solution, thereby electrochemically etching the tip. The transient current passes through the Pt tip even before turning on the working electrode because of capacitive coupling through the working-electrode switch and also with the SECM stage. The existence of these capacitive current paths is discussed in Supporting Information.

4.3.4 Protection against Electrochemical Damage of Electrodes

Noticeably, electrochemical damage is unlikely the unique problem of the potentiostat used in this work because the transient open-loop configuration is intrinsic to any potentiostat for a three-electrode cell. This problem may be readily avoided for a two-electrode cell by internally shorting the noninverting input of the reference electrode amplifier to the output of the counter-electrode amplifier in Figure 4-4C. SECM, however, often requires an electrochemical cell with more than two electrodes including a macroscopic substrate electrode.²³

4.4 CONCLUSIONS

In this work, we reported on the electrostatic and electrochemical origins of nanometer-scale damage to glass-sealed Pt UMEs with submicrometer and nanometer size. Both types of damage are severe with the small UMEs, which are readily charged up by a small number of electrons without potentiostatic control. Importantly, ESD damage to a UME in air can be avoided by protecting the UME from a source of electrostatic charge, most importantly, an operator. The body and cloth of the operator must be grounded by using ESD-safe wrist strap, gloves, and lab coat. Electrochemical damage is likely due to the flow of a transient current from a potentiostat amplifier into a UME and can be avoided by maintaining the UME under potentiostatic control in solution. This control can be lost transiently when connection of a potentiostat to the UME is internally switched on or off. Noticeably, the approaches that were proposed in this study to avoid ESD and electrochemical damage were validated for tip size of >100 nm. More ESD protections or a better potentiostat may be needed for protecting a smaller Pt UME from damage.

The new concept of nanoscale electrode damage proposed in this work is general and must be considered broadly for reliable nanoelectrochemical measurements and applications. Both electrostatic and electrochemical damage is possible with any submicrometer- or nanometer-size metal UME including an insulated metal tip for scanning tunneling microscopy. Moreover, “nano ESD” is a global concern in

nanoelectronics³⁴ including the batteries and sensors based on nanostructured electrodes. SECM is useful for detection of a damaged UME with recessed geometry, which gives a low positive feedback while a negative feedback is not sensitive to tip recession.²⁷ Recession and contamination of a damaged UME are not obvious from its well-defined steady-state CV with a lower limiting current, thereby unknowingly underestimating electrode size. In contrast to these metal UMEs, the SECM nanotip based on a nanopipet-supported liquid/liquid interface is apparently free from electrostatic and electrochemical damage.^{35,36} Alternatively, a soft liquid/liquid interface may be spontaneously renewable upon damage.

4.5 SUPPORTING INFORMATION

4.5.1 Chemicals

Ferrocenemethanol (FcMeOH, Strem Chemicals, Newburyport, MA) was recrystallized twice from hexane prior to use. All aqueous solutions were prepared with 18.3 M Ω -cm deionized water (Nanopure, Barnstead, Dubuque, IA).

4.5.2 Fabrication of Glass-Sealed Pt UMEs

A Pt UME was fabricated by heat-pulling the Pt microwire sealed in a glass capillary. Procedures for fabrication of the Pt UMEs sealed in borosilicate³⁷ and Pb-doped²³ glass capillaries were reported elsewhere. Similar procedures were employed for fabrication of Pt UMEs sealed in aluminosilicate glass capillaries (o.d./i.d. = 1.0 mm/0.64 mm, 10 cm in length, Sutter Instrument, Novato, CA). A CO₂-laser puller (model P-2000, Sutter Instrument) was used to stretch a glass capillary with a 25 μ m-diameter Pt wire, seal the wire in the stretched capillary, and pull the glass-sealed wire. A pulled Pt UME was heat annealed by using a microforge (MF-900, Narishige, Tokyo, Japan) and milled by using the FIB of a dual beam instrument (SMI3050SE FIB-SEM, Seiko Instruments, Chiba, Japan) unless otherwise mentioned.

4.5.3 ESD Protections

Glass-sealed Pt UMEs were protected from ESD as follows. An operator wore an ESD-safe lab coat (73506 or 73602, Desco Industries, Canton, MA), a wrist strap (BLUEWS61M, 3M, St. Paul, MN), and ESD-inspection gloves (68120, Desco), and used ESD-protected precision tweezers (7-SA-ET, Excelta, Buellton, CA) to handle a Pt UME in the lab and also in the cleanroom where FIB milling was done. The lab coat and wrist strap were directly grounded or connected to a grounded conductive mat (8811, 3M). The conductive path to ground and the presence of an inline 1 M Ω resistor in the wrist strap were confirmed frequently using a tester (19240, Desco Industries). To avoid ESD during FIB milling, the glass capillary and contact wire of a Pt UME were grounded to the metallic sample stage of the FIB instrument using single-sided adhesive copper tapes (1181, 3M). The grounding also reduced the charging of the glass sheath during FIB milling and SEM imaging. The copper tapes were attached (and detached) using the ESD-protected tweezers. During storage, the contact wire and glass capillary of UMEs were grounded to the conductive foams (12350, Desco) attached to the bottom of the storage case made of conductive plastic (4023, 3M) or aluminum (1590Q, Hammond Manufacturing, Cheektowaga, NY) (Figure 4-5). To avoid contamination from air, the tip cases were stored in a reclosable static shield bag (30068 and 3001012, 3M). For electrochemical measurement and optical microscopy, a UME was held in the groove of a homemade metal adaptor. In addition to the metal adaptor, both SECM and optical microscope (BX-41, Olympus America Inc., Melville, NY) were grounded. A grounded platinum wire was immersed in piranha solution for tip cleaning.

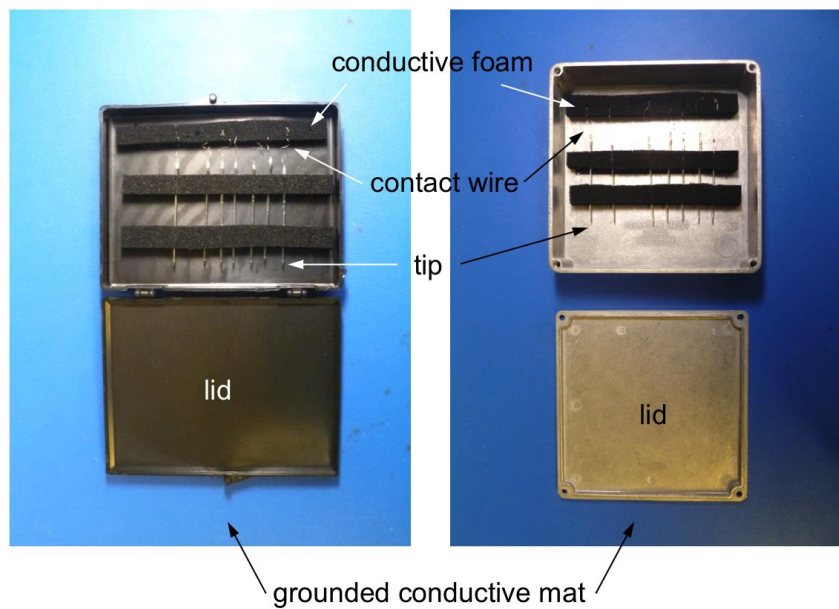


Figure 4-5. Images of the glass-sealed Pt UMEs stored on conductive foams in (left) plastic and (right) aluminum cases.

4.5.4 SEM Characterization of Pt UMEs

Both undamaged and damaged Pt UMEs were characterized by the field-emission SEM of the dual beam instrument as shown in Figures 4-1, 3A and B, and 4A. The SEM images of a submicrometer-size Pt UME with a thick glass sheath before and after ESD damage are shown in Figure 4-6A and B, respectively. An as-pulled Pt UME without heat annealing or FIB milling was also imaged by SEM before and after ESD damage (Figure 4-6C and D, respectively).

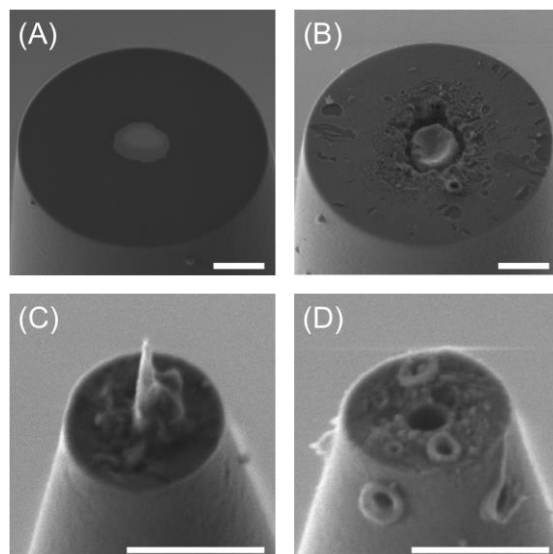


Figure 4-6. SEM images of (A and B) a FIB-milled Pt UME with a thick glass sheath and (C and D) an as-pulled Pt UME. The images were taken (A and C) before and (B and D) after ESD damage. Scale bars are 1 μm .

4.5.5 X-Ray EDS of Electrochemically Damaged Pt UMEs

The electrochemically damaged UME was imaged using X-ray EDS with FESEM (NanoSEM 630, FEI, Hillsboro, OR) as shown in Figure 4B. Characteristic X-rays were collected with the X-Max silicon drift detector (Oxford Instruments, Oxfordshire, UK) equipped with the FESEM. Elements were selected and mapped using Aztec Energy Analyzer Software (Oxford Instruments). Also, X-Ray EDS was obtained at the different locations of the electrochemically damaged Pt UME as indicated in the SEM image (Figure 4-7A). Pt peaks are seen not only at the center of the Pt tip (spectrum 1 in Figure 4-7B) but also at adsorbates on the glass surface (spectra 2 and 3). The Pt peaks at the adsorbate-covered regions of the glass surface do not originate from the central Pt region. No Pt peak was observed at the adsorbate-free region of the glass surface (spectrum 4).

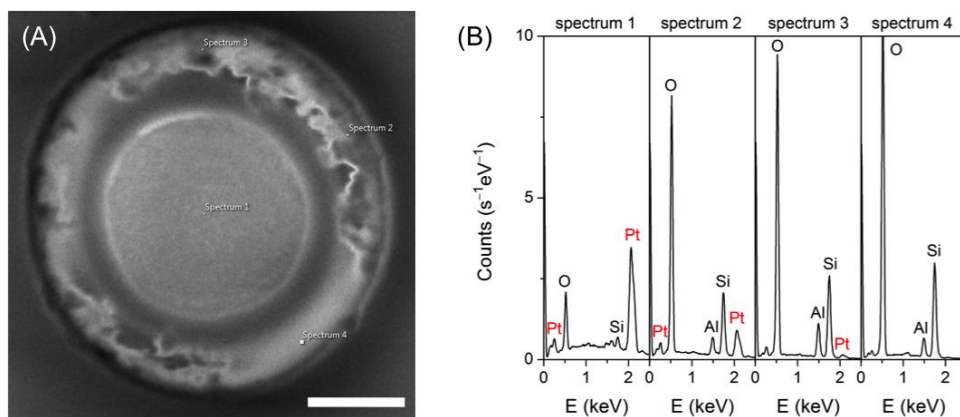


Figure 4-7. (A) SEM image of the electrochemically damaged Pt UME with locations where (B) X-ray EDS was taken. Scale bar is 0.5 μm .

4.5.6 Electrochemical Measurements

A home-built SECM stage³⁴ was employed to obtain the approach curve in Figure 4-2. The approximately 50 nm-thick Au film evaporated on the Si wafer (Ted Pella, Redding, CA) was employed as a conductive substrate. A 5 nm-thick Cr layer served as an adhesion layer between the Si wafer and the Au film. The tip current in the approach curve was monitored using CHI 910B while the “cell on between runs” function was active to avoid tip damage. This function was active also for measuring the CV of FcMeOH in the inset of Figure 4-2 without electrochemically damaging the ESD-damaged Pt UME.

4.5.7 Activation and Inactivation of the “Cell on between Runs” Function

The “cell on between runs” function of CHI 910B was activated and inactivated as follows. A Ag/AgCl reference/counter electrode was immersed in a 0.1 M KCl solution containing 0.5 mM FcMeOH. The counter and reference electrode cables of the potentiostat were attached to the Ag/AgCl electrode. After the “cell on between runs” function was checked in the program, this function was activated by running a dummy CV. Importantly, a Pt UME was not immersed in electrolyte solution or connected to the working electrode cable to the Pt UME. In this way, the UME did not experience transient current owing to electromechanical switching of the potentiostat from the internal dummy cell to

the electrochemical cell (Figure 4-4C). The dummy CV was finished when the potential of the working electrode cable was set to -0.05 V. Then, the Pt UME was connected to the working electrode cable under potentiostatic control at -0.05 V before the Pt tip was immersed in electrolyte solution. After measurement, the Pt tip was removed from the solution. Then, the working electrode cable was disconnected from the Pt UME in air. Finally, the “cell on between runs” function was inactivated by unchecking this function in the program and running CV.

4.5.8 Electrochemical Damage during CV Measurement

The Pt UME shown in Figures 4-4A and B were damaged during CV measurement as follows. Prior to electrochemical damage, the Pt UME was characterized by CV (cycles 1–5) while the “cell on between runs” function was active. The resultant CVs were well-defined (cycle 1 in Figure 4-8A) and reproducible with an average limiting current of 79.8 ± 0.2 pA (Figure 4-8B). This current value is consistent with the radius of the electrode estimated from its SEM image immediately after FIB milling (image not shown). The Pt UME was damaged during measurement of the next 29 CVs (cycles 6–34) when the “cell on between runs” function was inactive. Specifically, this function was unchecked in the program after the 4th CV so that the potentiostat was switched from the electrochemical cell to the dummy cell after the 5th CV. The first 20 CVs (cycles 6–25) were very irreproducible (cycles 7, 14, 16, and 19 in Figure 4-9A) and gave much higher or lower limiting currents (Figure 4-8B). The next 9 CVs (cycles 26–34) were relatively reproducible, but gave consistently lower limiting currents (Figure 4-8B) owing to tip recession. The damaged Pt UME was characterized by CV while the “cell on between runs” function was active. Specifically, the damaged Pt UME was detached from the electrode cable after the 34th CV, cleaned in piranha solution and deionized water, and then immersed in the FcMeOH solution. The Pt UME was connected to the electrode cable after the “cell on between runs” function was activated to set the potential of the working electrode cable to -0.05 V. Subsequently, 4 CVs (cycles 35–38) were obtained without electromechanically disconnecting the UME from the potentiostat. These CVs were very well defined (cycle 35 in Figure 4-8A) and reproducible as represented by an average limiting of $44.5 \pm$

0.2 pA (Figure 4-8B). The limiting currents were lower because of tip recession. After CV characterization, the damaged Pt UME was cleaned in piranha solution and deionized water, and imaged by SEM and X-ray EDS (Figures 3-4A and B, respectively) to confirm recession and contamination of the tip.

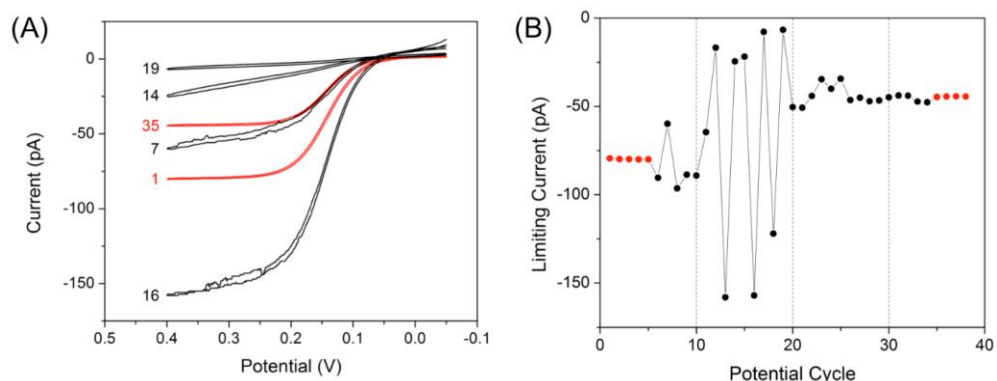


Figure 4-8. (A) Some of the 38 CVs of FcMeOH at a glass-sealed Pt UME and (B) limiting currents. Potential sweep rate, 20 mV/s. In part (A), the numbers indicate the order of potential cycles. The “cell on between runs” function was active (or inactive) before measurement of the CVs shown by red (or black) line and dots in parts (A) and (B), respectively.

4.5.9 Current Paths from a Tip to Ground

In the proposed mechanism (Figure 4-4C), transient current flows from the lead of a Pt UME to the working-electrode amplifier through capacitive coupling with the working-electrode switch when this switch is off. This current path must be present because a Pt tip was seriously damaged without turning on the working electrode (Figure 4-9A) while electromechanical relays for reference and counter electrodes were turned on and off (Figure 4-4C). This unconventional switching was enabled using the software modified by CH Instruments. Similarly severe damage was seen without the shielding of the working electrode cable. This result indicates that the capacitive coupling of the shield with the core wire of the cable is not a current path. The current path through the grounded SECM stage must also exist (Figure 4-4C) because a Pt tip was damaged without its connection to a potentiostat (Figure 4-9B) when the tip was

immersed in the solution and attached to the piezo positioner of the SECM stage through an aluminum holder. The aluminum holder was grounded to avoid ESD from the holder. In contrast, the replacement of the aluminum holder with a Teflon holder resulted in no tip damage when the counter/reference electrode was turned on and off without connecting the tip to the working electrode cable.

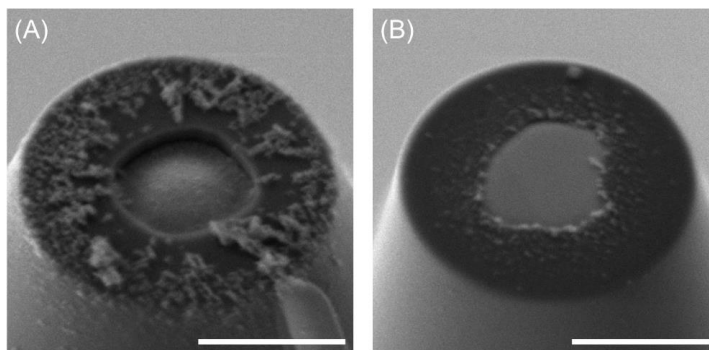


Figure 4-9. SEM images of the Pt tips electrochemically etched by turning on and off the reference/counter electrode for each of 30 potential cycles between -0.05 and 0.4 V while the tip was (A) connected to or (B) disconnected from a working electrode cable. The tips were immersed in the solution but were not turned on. Scale bars, $1 \mu\text{m}$.

ACKNOWLEDGMENTS

This work was supported by the National Institutes of Health (Grant GM073439) and the National Science Foundation (Grant CHE-1213452). We thank Drs. Melisa Yashinski and Trevor Clark, Materials Characterization Lab, Penn State University, for acquiring X-ray EDS, and Dr. Peixin He, CH Instruments, for helpful discussions. The Petersen Institute of NanoScience and Engineering at the University of Pittsburgh is acknowledged for technical support for FIB milling.

4.6 REFERENCES

- (1) Murray, R. W. *Chem. Rev.* **2008**, *108*, 2688.
- (2) Wang, Y. X.; Velmurugan, J.; Mirkin, M. V. *Israel J. Chem.* **2010**, *50*, 291.
- (3) Cox, J. T.; Zhang, B. In *Ann. Rev. Anal. Chem.* **2012**, *5*, 253.
- (4) Singh, P.; Goluch, E.; Heering, H.; Lemay, S. Nanoelectrochemistry: Fundamentals and Applications in Biology and Medicine. In *Applications of Electrochemistry and Nanotechnology in Biology and Medicine II*; Modern Aspects of Electrochemistry, Eliaz, N., Ed.; Springer US: 2012; Vol. 53, p 1.
- (5) Amemiya, S.; Bard, A. J.; Fan, F.-R. F.; Mirkin, M. V.; Unwin, P. R. *Ann. Rev. Anal. Chem.* **2008**, *1*, 95.
- (6) *Scanning Electrochemical Microscopy*; 2nd ed.; Bard, A. J.; Mirkin, M. V., Eds.; CRC Press: Boca Raton, FL, 2012.
- (7) Pendley, B. D.; Abruna, H. D. *Anal. Chem.* **1990**, *62*, 782.
- (8) Lee, C.; Miller, C. J.; Bard, A. J. *Anal. Chem.* **1991**, *63*, 78.
- (9) Shao, Y.; Mirkin, M. V.; Fish, G.; Kokotov, S.; Palanker, D.; Lewis, A. *Anal. Chem.* **1997**, *69*, 1627.
- (10) Katemann, N. B.; Schuhmann, W. *Electroanalysis* **2002**, *14*, 22.
- (11) Sun, P.; Mirkin, M. V. *Anal. Chem.* **2006**, *78*, 6526.
- (12) Zhang, B.; Galusha, J.; Shiozawa, P. G.; Wang, G.; Bergren, A. J.; Jones, R. M.; White, R. J.; Ervin, E. N.; Cauley, C. C.; White, H. S. *Anal. Chem.* **2007**, *79*, 4778.
- (13) Zuliani, C.; Walsh, D. A.; Keyes, T. E.; Forster, R. J. *Anal. Chem.* **2010**, *82*, 7135.
- (14) Mezour, M. A.; Morin, M.; Mauzeroll, J. *Anal. Chem.* **2011**, *83*, 2378.
- (15) Velmurugan, J.; Sun, P.; Mirkin, M. V. *J. Phys. Chem. C* **2008**, *113*, 459.
- (16) Noël, J.-M.; Velmurugan, J.; Gökmeşe, E.; Mirkin, M. *J. Solid State Electrochem.* **2013**, *17*, 385.
- (17) Li, Y.; Bergman, D.; Zhang, B. *Anal. Chem.* **2009**, *81*, 5496.

- (18) Xiong, H.; Guo, J.; Amemiya, S. *Anal. Chem.* **2007**, *79*, 2735.
- (19) Shen, M.; Arroyo-Currás, N.; Bard, A. J. *Anal. Chem.* **2011**, *83*, 9082.
- (20) Chang, J.; Leonard, K. C.; Cho, S. K.; Bard, A. J. *Anal. Chem.* **2012**, *84*, 5159.
- (21) Satpati, A. K.; Bard, A. J. *Anal. Chem.* **2012**, *84*, 9498.
- (22) Bonazza, H. L.; Fernández, J. L. *J. Electroanal. Chem.* **2010**, *650*, 75.
- (23) Nioradze, N.; Kim, J.; Amemiya, S. *Anal. Chem.* **2011**, *83*, 828.
- (24) Kim, J.; Izadyar, A.; Nioradze, N.; Amemiya, S. *J. Am. Chem. Soc.* **2013**, *135*, 2321.
- (25) Nogala, W.; Velmurugan, J.; Mirkin, M. V. *Anal. Chem.* **2012**, *84*, 5192.
- (26) Mardiguian, M. *Electrostatic Discharge: Understand, Simulate, and Fix ESD Problems*; John Wiley & Sons: Hoboken, NJ, 2009.
- (27) Sun, P.; Mirkin, M. V. *Anal. Chem.* **2007**, *79*, 5809.
- (28) Lefrou, C. *J. Electroanal. Chem.* **2006**, *592*, 103.
- (29) Shoup, D.; Szabo, A. *J. Electroanal. Chem.* **1984**, *160*, 27.
- (30) Cornut, R.; Lefrou, C. *J. Electroanal. Chem.* **2007**, *604*, 91.
- (31) Bond, A. M.; Luscombe, D.; Oldham, K. B.; Zoski, C. G. *J. Electroanal. Chem.* **1988**, *249*, 1.
- (32) Kamino, T.; Yaguchi, T.; Ohnishi, T.; Ishitani, T. In-Situ Sample Manipulation and Imaging. In *Focused Ion Beam Systems: Basics and Applications*; Yao, N., Ed.; Cambridge University Press: Cambridge, UK, 2007, p 250.
- (33) Noël, J.-M.; Yu, Y.; Mirkin, M. V. *Langmuir* **2013**, *29*, 1346.
- (34) Kim, J.; Shen, M.; Nioradze, N.; Amemiya, S. *Anal. Chem.* **2012**, *84*, 3489.
- (35) Shen, M.; Ishimatsu, R.; Kim, J.; Amemiya, S. *J. Am. Chem. Soc.* **2012**, *134*, 9856.
- (36) Voldman, S. H. Nano ESD: Electrostatic Discharge in the Nanoelectronic Era. In *Nanoelectronics: Nanowires, Molecular Electronics, and Nanodevices*; Iniewski, K., Ed.; McGraw-Hill: New York, 2011, p 481.
- (37) Kim, J.; Izadyar, A.; Nioradze, N.; Amemiya, S. *J. Am. Chem. Soc.* **2013**, *135*, 2321.

- (38) Nioradze, N.; Kim, J.; Amemiya, S. *Anal. Chem.* **2011**, *83*, 828.
- (39) Kim, J.; Shen, M.; Nioradze, N.; Amemiya, S. *Anal. Chem.* **2012**, *84*, 3489.

5.0 ORGANIC CONTAMINATION OF HIGHLY ORIENTED PYROLYTIC GRAPHITE AS STUDIED BY SCANNING ELECTROCHEMICAL MICROSCOPY

This work has been submitted as Nikoloz Nioradze, Ran Chen, Niraja Kurapati, Anastasia Khvataeva-Domanov, Stéphane Mabic, and Shigeru Amemiya, Organic Contamination of Highly Oriented Pyrolytic Graphite as Studied by Scanning Electrochemical Microscopy, *Anal. Chem.* 2014. The thesis author nanofabricated electrodes, collected and analyzed experimental data.

5.1 INTRODUCTION

Highly oriented pyrolytic graphite (HOPG) is an important electrode material that serves as a structural model of advanced graphitic nanocarbons such as graphene and carbon nanotubes. Here, we apply scanning electrochemical microscopy (SECM) to quantitatively demonstrate that the electroactivity of the HOPG basal surface is compromised by the adsorption of adventitious organic impurities. The resultant layer of hydrophobic contaminants is less permeable to a more hydrophilic (i.e., more charged) form of a redox couple to yield different standard rate constants, k^0 , and mass transport parameters for the oxidation and reduction of the redox couple. We employ SECM-based nanogap voltammetry to reveal these anomalous features by probing both the oxidation and the reduction of a redox couple within a wide range of the HOPG potential. Experimentally, a nanometer-wide gap is formed between the HOPG surface and a 1 μm -diameter Pt tip to achieve high mass transport conditions, which enable the quasi-steady-state measurements of all thermodynamic, kinetic, and mass transport parameters. The oxidation and reduction of the (ferrocenylmethyl)trimethyl ammonium couple at the HOPG surface is accelerated by a factor of >10 when the aqueous concentration of organic impurities, i.e., total organic (or oxidizable) carbon, is decreased from ~ 20 ppb to ~ 1 ppb. The most purified water gives extremely high k^0 values of >17 and >13 cm/s as well as the corresponding nanogap widths of 36 and 45 nm for oxidation and reduction, respectively. Differences in the kinetic and mass transport parameters evidence that the HOPG

surface is covered with airborne contaminants. The electroactivity of graphitic surfaces can be unintentionally lowered by the adsorption of unknown impurities on these good adsorbents to possibly undermine their intended electrochemical applications.^{1,2} Therefore, various preparation methods have been developed to clean or activate the surfaces of graphitic electrodes.³ The origin and identity of adventitious impurities, however, are not well understood. Recently, the airborne contamination of graphene^{4,5} and highly oriented pyrolytic graphite (HOPG)^{4,6} was studied in details to address their intrinsic water wettability. For instance, the water contact angle of a fresh HOPG surface was 64.4° within 10 s after exfoliation and increased to ~90° after 10 min exposure to ambient air.⁶ This change in water contact angle was ascribed to the adsorption of airborne hydrocarbons on the HOPG surface as confirmed by attenuated total reflectance-Fourier transform infrared spectroscopy (ATR-FTIR). Ellipsometry was also employed to monitor the growth of a ~0.5 nm thick film on the HOPG surface exfoliated and stored in ambient air. These experimental results were assessed by using a quantitative theory to conclude that the water contact angle of the HOPG basal plane can increase to ~90° owing to the adsorption of a sub-nanometer thick monolayer of airborne hydrocarbons. This conclusion augments the reliability of previous electrochemical studies, where the HOPG surface was covered with a solution within 10–15 s of exfoliation to minimize airborne contamination.⁷ Such quick protection of the fresh HOPG surface, however, is not practicable in advanced electrochemical measurements such as imaging.⁸⁻¹¹

Adventitious contamination has been considered as the cause of the heterogeneous electroactivity of the HOPG basal plane¹² and graphene/graphite flakes¹³ as revealed by scanning electrochemical microscopy (SECM)^{14,15} combined with atomic force microscopy (AFM).¹⁶ In these SECM–AFM studies, a submicrometer-sized electrode was integrated into the tip of an AFM cantilever to image the electrochemical reactivity of graphitic surfaces as well as their topography and conductivity. Heterogeneous electroactivity to ferrocenemethanol (FcMeOH) was observed in the SECM image of a graphite flake,¹³ which was possibly contaminated in air during exfoliation from HOPG and immobilization on the oxidized silicon wafer as well as in the electrolyte solution of an AFM cell.

Interestingly, less than 1 nm variation was seen in the ~20 nm-height topography of the heterogeneously electroactive surface, which should be partially covered by a molecularly thin insulating layer. In addition, conductivity imaging revealed the heterogeneous passivation of the HOPG surface without any detectable topographic feature.¹² These SECM–AFM studies, however, neither identified nor eliminated a surface contaminant. Moreover, no attempt was made to quantitatively assess the effect of adventitious contamination on the electroactivity of graphitic surfaces.

Here, we report on the SECM study of the HOPG plane surface to quantitatively reveal how its electroactivity is compromised by organic impurities from ambient air and ultrapure water. Significantly, HOPG serves as a structural model of advanced nanocarbon electrode materials such as graphene and carbon nanotubes.^{17,18} Uniquely, we study both the oxidation and reduction of a simple redox couple, (ferrocenylmethyl)trimethyl ammonium (FcTMA^+), under extremely high mass transport conditions by positioning an amperometric Pt tip at a nanometer distance from the HOPG surface. Advantageously, this nanogap-based approach enables the quasi-steady-state measurements of all thermodynamic, kinetic, and mass transport parameters at a macroscopic electrode within a wide range of its potential.¹⁹ Specifically, the feedback mode of SECM is employed to study the reduction of tip-generated FcTMA^{2+} preceded by its permeation through a contaminant layer on the HOPG surface (Figure 1A). Moreover, the substrate generation/tip collection (SG/TC) mode monitors the permeation and the following oxidation of FcTMA^+ at the contaminated surface (Figure 5-1B). Importantly, the hydrophobic contaminant layer is less permeable to more hydrophilic FcTMA^{2+} with higher charge than to FcTMA^+ . Therefore, surface contamination is evidenced by different kinetic and mass transport parameters as determined from a pair of anodic and cathodic voltammograms at the same tip–HOPG distance.

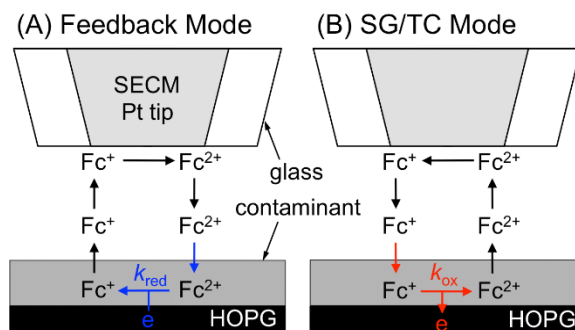


Figure 5-1. Scheme of the (A) feedback and (B) SG/TC modes of SECM at the contaminated HOPG surface under a glass-sealed Pt tip. Fc^+ and Fc^{2+} represent FcTMA^+ and FcTMA^{2+} , respectively.

In this work, we complement the SECM approach with a theoretical approach to assess the effects of organic impurities from ultrapure water and ambient air on the electroactivity of the HOPG basal plane. We employ SECM-based nanogap voltammetry to demonstrate that the electroactivity of the HOPG surface to the FcTMA^+ couple increases by a factor of ~ 10 when the total organic carbon (TOC) of ultrapure water as a measure of organic impurities²⁰ is reduced from ~ 20 ppb to ~ 1 ppb. The most purified water gives extremely high k^0 values of >17 and >13 cm/s as well as the corresponding nanogap widths of 36 and 45 nm for oxidation and reduction, respectively. Amazingly, these k^0 values are comparable to the highest k^0 value reported so far, i.e., 17 cm/s for $\text{Ru}(\text{NH}_3)_6^{3+}$ at a Pt nanoelectrode.²¹ In addition, we confirm theoretically that differences in the effective kinetic and mass transport parameters are due to the preceding contamination of the HOPG surface with a monolayer amount of airborne hydrocarbons.^{4,6}

5.2 EXPERIMENTAL SECTION

5.2.1 Chemicals and Materials

FcMeOH was obtained from Aldrich (Milwaukee, WI) and recrystallized twice from hexane prior to use. The hexafluorophosphate salt of FcTMA^+ was prepared by the metathesis of its iodide salt (Strem

Chemicals, Newburyport, MA) and ammonium hexafluorophosphate (Strem Chemicals). Silicon wafers with 100 nm of gold over a 5.0 nm-thick titanium adhesion layer were obtained from Platypus Technologies (Madison, WI). SPI-1 grade HOPG was obtained from SPI Supplies (West Chester, PA).

5.2.2 Water Purification

A Nanopure water system (D4741, Barnstead, Dubuque, IA) equipped with an ORGANIC free filter (D5026 cartridge kit, Barnstead) was used to obtain ultrapure water with a TOC value of 22 ± 1 ppb as measured by using an A10 TOC monitor (EMD Millipore, Billerica, MA). The water purification system was fed with building deionized water with a resistivity of 0.56 M Ω cm and a TOC value of <0.1 ppm. A Milli-Q Advantage A10 system (EMD Millipore) was used to obtain UV-treated ultrapure water with a TOC value of ~2 ppb as measured by an internal online monitor. To achieve this low TOC value, building deionized water was pretreated with the ultrapure (D0809) and organic removal (D0813) cartridges of a Barnstead B-Pure system (Thermo Scientific, Marietta, OH) and fed into the Milli-Q system. UV-treated ultrapure water was also passed through an external activated-carbon filter (VOC Pak, Millipore) to remove volatile organic contaminants, thereby yielding a TOC value of ~1 ppb as measured by using the A10 TOC monitor. ICP-MS and an ion-selective electrode²² were employed to confirm that major contaminants in the filtered water are electrochemically inactive, i.e., alkaline and alkaline earth metals, in addition to <5 nM Fe, Ni, Ti, and Zn (Table 5-3 in Supporting Information). Both Nanopure water and Milli-Q water were used immediately after collection to prevent the introduction of organic contaminants during storage.²³ In addition, Milli-Q water was collected in a class 100 vertical laminar flow hood (model AC632LFC, AirClean Systems, Raleigh, NC) to prevent its contamination with aerosols.²²

5.2.3 Tip Fabrication

A Pt tip was fabricated by using a CO₂-laser puller, microforge, and a focused ion beam (FIB) instrument as reported elsewhere^{19,24} and protected from electrostatic and electrochemical damages.^{25,26} In our previous work,¹⁹ only >100 nm-wide gap was formed between a FIB-milled Pt tip with 1 μ m diameter

and a polished Pt substrate. The submicrometer width was limited not only by the roughness of the Pt substrate¹⁹ but also by the nanoscale damage of the Pt tip owing to electrostatic discharge and electrochemical etching.²⁵ In this work, we use the flat Au film deposited on oxidized silicon wafer and also protect tips from the nanoscale damages.^{25,26} In addition, we ensure that the milled tip surface is perpendicular to the tip length by compensating the Gaussian broadening of the focused Ga⁺ beam (Figure 5-8, Supporting Information). Specifically, the tip was tilt with respect to Ga⁺ beam by 1.5° to obtain the closest tip–substrate distance that is shorter than that achieved by using the tips tilted by 1.0° and 2.0° for FIB milling (Figure 5-9).

5.2.4 SECM Measurement

A homebuilt SECM instrument with an isothermal chamber²⁷ was used for approach curve measurement and nanogap voltammetry. Pt and Ag/AgCl wires were used as counter and reference electrodes, respectively. An electrochemical cell was prepared by using a glass ring with a Teflon bottom, where HOPG was inserted from the back (Figure 5-11). The glass and Teflon components were cleaned in piranha solution (a 3:1 mixture of 30% H₂O₂ and 95.0–98.0% H₂SO₄) for 90 minutes and in Milli-Q water for 15 minutes (3 times), and dried in air for 5 minutes (Caution: piranha solution reacts violently with organics and should be handled with extreme care!). The top of the assembled cell was sealed by a rubber cap with a silicon gasket to eliminate water evaporation as well as the contamination of the electrolyte solution with airborne organic impurities. The perpendicular alignment of a tip axis with respect to the substrate surface was confirmed within an error of ±0.5° by using a digital angle gauge.

5.3 RESULT AND DISCUSSION

5.3.1 Clean Surface of Pt Tips

The surface of our 1 μm -diameter Pt tips is clean enough to yield highly positive approach curves at a gold substrate in ~ 20 ppb-TOC water (Figure 5-2). Remarkably, tip current, i_T , was enhanced by a factor of ~ 28 in comparison with tip current in the bulk solution, $i_{T,\infty}$, as given by

$$i_{T,\infty} = 4xnFDca \quad (1)$$

where x is a function of RG ,^{28,29} n is the number of transferred electrons in the tip reaction, and D and c are the diffusion coefficient and concentration of a redox mediator in the aqueous solution, respectively. A high normalized tip current of ~ 28 at contact is consistent with the value expected for a tip with $RG = 2.0$ and tilted by $< 1.0^\circ$ with respect to the substrate (Figure 5-10). The normalized approach curve was fitted well with a theoretical curve for positive feedback,³⁰ thereby confirming that tip current was limited by the diffusion of FcMeOH across the tip–substrate gap. The theoretical analysis of the approach curve gave an extremely short contact distance, d_c , of 12 nm ($d_c/a = 0.026$). This narrow gap width is comparable to or even narrower than the width of the nanogaps formed by using Pt²¹ and Au³¹ nanotips with $a = 14.7\text{--}142$ nm and $RG = 3\text{--}10$ over a flat Au surface.

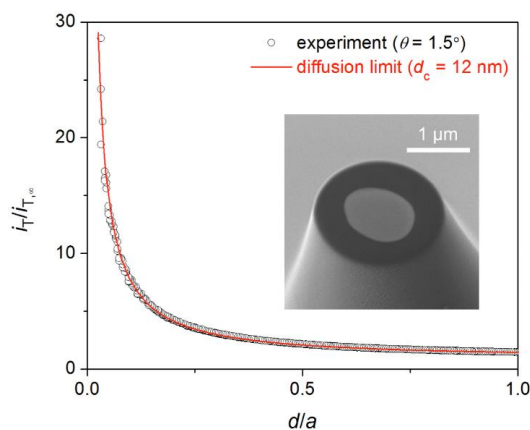


Figure 5-2. Experimental (circles) and theoretical (red line) approach curves at an unbiased Au substrate in 0.5 mM FcMeOH and 0.1 M KCl as obtained by using an FIB-milled Pt tip with $\theta = 1.5^\circ$, $a = 0.47$ μm , and $RG = 2.0$. Probe scan rate, 19 nm/s. Tip potential, 0.35 V vs. Ag/AgCl.

5.3.2 Approach Curve at HOPG in Filtered Water

The presence of a contaminant layer on the HOPG surface in filtered ultrapure water (~20 ppb TOC) results in moderately positive approach curves to puzzle their interpretation. For instance, we measured SECM approach curves to observe a much lower feedback effect from HOPG (Figure 5-3) than that from the flat Au substrate (Figure 5-2) when the same ~20 ppb-TOC ultrapure water was used. This is not due to the use of different redox mediators because approach curves at the HOPG surface were also moderately positive with FcMeOH (data not shown). The tip current was enhanced only by a factor of ~3.5 at the tip–HOPG contact in comparison with tip current in the bulk solution. Subsequently, a submicrometer contact distance of 0.14 μm ($d_c/a = 0.26$) was obtained by fitting the experimental approach curve at the HOPG surface with a theoretical curve for pure positive feedback (red line in Figure 5-3A).³⁰ This contact distance is too large for a flat HOPG (SP1-grade), which has only a few step edges¹¹ under a 1 μm -diameter Pt tip. We ascribe the submicrometer contact distance to the erroneous fitting of the experimental curve to the pure positive feedback curve. In fact, the experimental curve fits slightly better with a kinetically limited approach curve³² to yield a heterogeneous electron-transfer (ET) rate constant of 0.53 cm/s and a tip–substrate contact distance of 13 nm (blue line). This contact distance is more consistent with the short tip–substrate distance that was achieved by employing the flat Au substrate (Figure 5-2A). This interpretation is inconsistent with the fact that the HOPG potential during approach curve measurement was negative enough to ensure a potential-independent feedback response as confirmed voltammetrically (see below). Apparently, the feedback effect from the HOPG plane surface in ~20 ppb-TOC ultrapure water was controlled neither by mediator diffusion across the tip–HOPG gap nor by the potential-dependent ET kinetics at HOPG. This anomalous approach curve is ascribed to the feedback effect that is limited by the potential-independent permeation of FcTMA²⁺ through the contaminant layer on the HOPG surface.

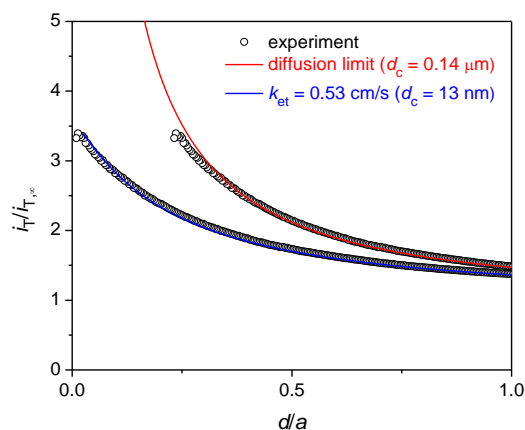


Figure 5-3. Approach curves at HOPG in 0.3 mM FcTMA⁺ and 0.05 M KCl (circles) as fitted to theoretical curves limited by mediator diffusion (red line) or by ET kinetics at the HOPG surface (blue line). Probe scan rate, 49 nm/s. Tip and substrate potentials, 0.5 and 0.1 V vs. Ag/AgCl, respectively. The theoretical curves used $a = 0.48$ μm , $RG = 2.5$.

5.3.3 Nanogap Voltammetry at HOPG in Filtered Water

The presence of a contaminant layer on the HOPG surface was evidenced by nanogap voltammetry in 20 ppb-TOC Nanopure water purified by fresh filters. In this experiment, a FIB-milled Pt tip was positioned at a fixed feedback distance from the HOPG surface to amperometrically detect FcTMA⁺ or FcTMA²⁺ in the feedback or SG/TC mode, respectively, during the successive cycles of the HOPG potential. A pair of the voltammograms was obtained at the same tip position to eventually yield a family of paired voltammograms at various tip positions (Figure 5-4A; the same color is used for each pair of voltammograms measured at the same tip position). In both operation modes, the tip current was measured at quasi-steady states to reach a plateau value with the sufficiently positive or negative HOPG potential in the SG/TC or feedback mode, respectively.¹⁹ The limiting current at the same tip position, however, was always lower in the feedback mode than in the SG/TC mode. Subsequently, the fitting of the experimental voltammograms with theoretical ones¹⁹ gave a shorter tip–substrate distance in the SG/TC mode than in the feedback mode (see Table 5-1 for parameters used for this fitting). This

difference in the tip–substrate distance between the two operation modes is not due to the thermal drift of vertical tip position with respect to the HOPG surface, which was minimized by accommodating the SECM stage in an isothermal chamber.^{27,33} In fact, nearly identical voltammograms were obtained when potential cycles were repeated for either mode (data not shown).

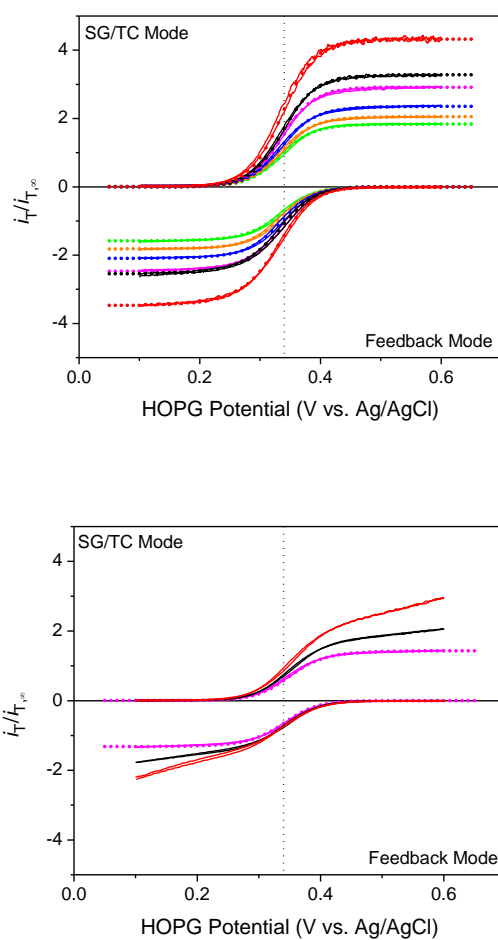


Figure 5-4. Experimental (solid lines) and theoretical (dotted lines) nanogap voltammograms at HOPG in 0.3 mM FcTMA⁺ and 0.05 M KCl prepared by water purified through (A) fresh and (B) 17 month old filters. Potential sweep rate, 0.05 V/s. Tip potentials are 0.5 and 0.15 V for the feedback and SG/TC modes, respectively. Theoretical curves used $(a, RG) =$ (A) (0.48 μm , 2.5) and (B) (0.54 μm , 1.8) in addition to $E^{0c} = 0.34$ V (vertical dotted lines) and parameters in Table 1.

Table 5-1. Parameters from Figure 5-4A

Feedback Mode			SG/TC Mode		
d^a	k^{0b}	λ	d^a	k^{0b}	λ
0.12	1.1	2.2	0.1	2.6	4.3
0.19	0.7	2.2	0.13	2.6	5.6
0.21	0.8	2.8	0.17	1.7	4.8
0.28	0.8	3.7	0.23	0.9	3.5
0.36	0.6	3.6	0.29	1.2	5.8
0.46	0.3	2.3	0.34	1.2	6.8

^a in μm . ^b in cm/s .

Different k^0 and d values were obtained from pairs of nanogap voltammograms (Table 5-1) owing to the different permeability of the contaminant layer on the HOPG surface to FcTMA^+ and FcTMA^{2+} (Figure 5-1). In the feedback mode, low permeation of tip-generated FcTMA^{2+} through the hydrophobic layer results in apparently lower k^0 values (0.7 ± 0.3 cm/s) and lower limiting currents, which correspond to erroneously longer tip–HOPG distances (Table 5-1). By contrast, significantly higher k^0 values (1.7 ± 0.3 cm/s) and shorter tip–HOPG distances were obtained in the SG/TC mode at the same tip positions, where less hydrophilic FcTMA^+ is more readily transported through the contaminant layer and oxidized at the underlying HOPG surface. In fact, the nanogap voltammograms in the SG/TC mode are nearly Nernstian, as indicated by high normalized standard rate constant, λ ($= dk^0/D$), with an average value of 5 ± 1 in comparison with that of 2.8 ± 1 for voltammograms in the feedback mode. Noticeably, these large λ values are still distinguishable from those of ≥ 10 for reversible nanogap voltammograms, where both anodic and cathodic branches are measured to precisely determine thermodynamic, kinetic, and mass

transport parameters.^{34,35} In fact, the experimental nanogap voltammograms gave a normal α value of 0.5 and a consistent formal potential, $E^{0'}$, of 0.34 V vs. Ag/AgCl (Figure 5-4A).

A more serious effect of a contamination layer on the nanogap voltammograms of the FcTMA^{2+/+} couple was seen when ultrapure water was obtained by using ~17 month-old filters. This result indicates the importance of TOC monitoring, which prevents an unnoticed increase in the TOC of ultrapure water when the filters of a water purification system are consumed. By contrast, water purity was checked in previous electrochemical studies of HOPG^{9-11,36-39} only by measuring water resistivity, which is not affected by electrically neutral organic impurities.⁴⁰

Specifically, we observed the very low enhancement of the tip current ($i_T / i_{T,\infty} < 3$) at the HOPG surface in ultrapure water prepared by using the old filters despite a normal resistivity of 18.2 M Ω ·cm (Figure 5-4B). The low enhancement of the tip current was also seen in approach curve, where a low positive feedback effect resulted in a $i_T / i_{T,\infty}$ value of only 2.5 at the tip–HOPG contact (Figure 5-11). Anomalously, the tip current in both feedback and SG/TC modes increased gradually toward more negative and positive potentials, respectively, without reaching a plateau (red and black curves) with the exception of a wide tip–HOPG separation (magenta curves). The limiting current in the SG/TC mode, however, was higher than that in the feedback mode as expected for the contaminated HOPG surface, thereby yielding inconsistent d values of 0.54 and 0.67 μm for the respective operation modes. Moreover, a k^0 value of 0.15 cm/s in the feedback mode was lower than that of 0.19 cm/s in the SG/TC mode, which is limited by the faster permeation of FcTMA⁺ through the contaminant layer. Noticeably, both k^0 values are significantly lower than those in water purified by fresh filters (Table 5-1) and are still high enough to yield a reversible CV when the substrate current was measured (Figure 5-13)

5.3.4 Highly Positive Approach Curve at HOPG in UV-Treated Water

The additional UV treatment of filtered ultrapure water not only decreased TOC but also gave more positive feedback curves at the HOPG surface, which is less contaminated. Highly positive

approach curves were obtained at HOPG in UV-treated water with a TOC value of 2 ppb (Figure 5-5A) in comparison with approach curves in ~20 ppb-TOC ultrapure water (Figure 5-4A). This result confirms that a lower feedback effect in the latter water is due to the organic contamination of HOPG surface in the water. A very close tip–substrate distance of 32 nm was obtained when the approach curve was fitted with a purely positive feedback curve (red line) while a good fit with a kinetically limited curve (blue line) gave a slightly closer contact distance of 17 nm and an ET rate constant of 2.0 cm/s. These d_c values are closer to each other than those determined from approach curves in filtered water (Figures 5-3 and 5-12), thereby indicating that the analysis of a more positive approach curve is more accurate. The effective ET rate constant is also higher in the UV-treated water than that in the filtered water, which contaminates the HOPG surface more seriously. In fact, only a slightly higher feedback effect was observed with ~1 ppb-TOC water as obtained by purifying UV-treated water through an activated carbon filter (Figure 5-5B), thereby indicating that 2 ppb-TOC water is pure enough not to seriously contaminate the HOPG surface, which is covered with airborne contaminants (see below).

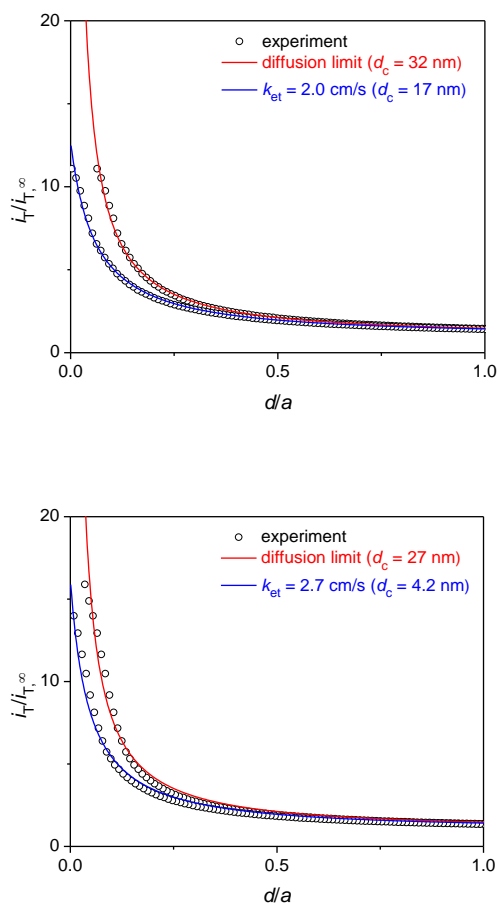


Figure 5-5. Approach curves at the HOPG surface in 0.3 mM FcTMA⁺ and 0.05 M KCl in UV-treated ultrapure water (A) before and (B) after filtration through an additional activated-carbon filter. Probe scan rate, 49 nm/s. Tip and substrate potentials, 0.50 and 0.15 V vs. Ag/AgCl, respectively. The theoretical curves used (a , RG) = (0.48 μm , 2.5) and (0.48 μm , 2.5) for (A) and (B), respectively.

5.3.5 High Electroactivity of HOPG in ~1 ppb TOC Water

We employed nanogap voltammetry to reveal the extremely high electroactivity of HOPG in ~1 ppb-TOC water (Figure 5-6). The nanogap voltammograms fit well with reversible voltammograms, thereby enabling us only to estimate the minimum k^0 values corresponding to $\lambda = 10$ (Table 5-2). The largest k^0 values of ≥ 13 cm/s and ≥ 17 cm/s as well as the corresponding tip–HOPG distances of 45 and 36

nm were estimated from the voltammograms in the feedback and SG/TC modes, respectively. The higher k^0 value and the shorter distance in the SG/TC mode indicate that the HOPG surface is still contaminated with airborne impurities. In fact, the higher permeability of the airborne contaminant layer to FcTMA^+ results in a higher mass transport condition, and subsequently, a higher limiting current in the SG/TC. Nevertheless, these k^0 values in ~ 1 ppb-TOC water are several times higher than those measured in ~ 20 ppb-TOC water (Table 5-1). Together with the result of the approach curve experiment in Figure 5-5, this result indicates that the airborne-contaminated HOPG surface is not further contaminated with organic impurities in 2 and ~ 1 ppb-TOC water. Noticeably, the tip current that is largely enhanced at short tip-HOPG distances in ~ 1 ppb-TOC water significantly fluctuates, which corresponds to a change of only ± 1 nm in the distance. Such a small distance fluctuation can be ascribed to the vibration of the SECM system or the fluctuation of the piezo stage.²⁷

The k^0 values at the HOPG surface in ~ 1 ppb-TOC water (Table 5-2) is unprecedentedly high for a graphitic electrode. A range of 0.1–1 cm/s was estimated for FcTMA^+ at HOPG by SECCM,¹⁰ where a ~ 0.5 μm -sized θ pipet was employed as a tip to reach a reversible limit with $k^0 = 1$ cm/s owing to the hindrance of mass transport by the inner wall of the pipet.⁴¹ Higher mass transport conditions were achieved in this work by using a larger 1 μm -diameter disk tip, which can be positioned at an extremely close distance of down to 36 nm from HOPG. Our k^0 values for FcTMA^+ at the HOPG surface also exceed a k^0 value of 9 cm/s for FcTMA^+ at single-wall carbon nanotubes as determined by SECCM without a mass transfer limitation owing to the small tube diameter.⁴² Much lower k^0 values of 0.03–0.5 cm/s were obtained for FcTMA^+ at single-layer and multi-layer graphenes by using SECCM.⁸ The k^0 values might be underestimated in the SECCM studies of nanotubes and graphenes, where inadequate attention was paid to surface contamination in air and water.

Amazingly, the highest k^0 value of ≥ 17 cm/s as estimated for FcTMA^+ at HOPG in this study is comparable to the highest k^0 value reported so far, i.e., 17 cm/s for $\text{Ru}(\text{NH}_3)_6^{3+}$ at a Pt nanoelectrode.²¹ On the one hand, the high k^0 value at a Pt nanoelectrode may be underestimated because the surface of such a

small electrode can be contaminated with trace organic impurities in ultrapure water.⁴³ In fact, Scherson and Tolmachev pointed out theoretically that 1 ppb-TOC water requires 12 seconds to achieve $\theta = 1.0$ for a ~ 50 nm-radius Pt electrode owing to the small electrode size and efficient diffusional mass transport.⁴³ On the other hand, the high k^0 value at the HOPG surface may be due to the enhanced local density of states (DOS) at point defects, which can be formed during the peeling of the HOPG surface by scotch tape. In fact, STM studies have demonstrated the dramatic enhancement of the DOS at atomic defects⁴⁴ as well as the surrounding sp^2 carbon atoms over ~ 6 nm distance owing to their good conjugation.⁴⁵ This long-range effect contrasts with the local and very weak disturbance of the DOS at step edges.⁴⁶ In addition, nanometer-sized defects on the basal surface were observed by STM when HOPG was peeled by scotch tape or spontaneously cleaved by a blade to expose a fresh surface.⁴⁷ In fact, we sometimes observed a large fluctuation of tip current at a very short tip–HOPG distance (Figure 5-12, Supporting Information). The huge current is ascribed to electron tunneling between the flat Pt tip and a nanostructural defect protruded from the HOPG surface.

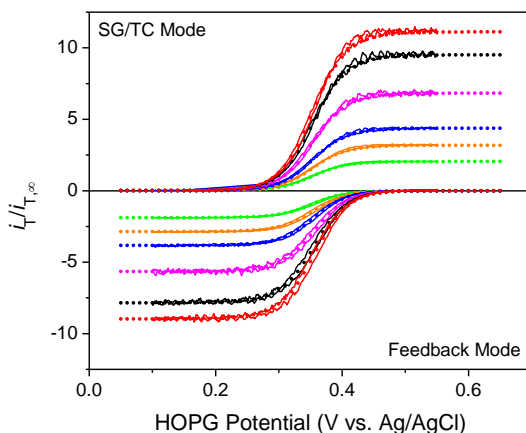


Figure 5-6. Nanogap voltammograms at HOPG in ~ 1 ppb-TOC water containing 0.3 mM FcTMA⁺ and 0.05 M KCl. Solid and dotted lines represent experimental and theoretical voltammograms, respectively. The parameters used for the theoretical curves are listed in Table 2. Potential sweep rate, 0.05 V/s. Tip potential, 0.50 and 0.15 V in the feedback and SG/CT modes, respectively.

Table 5-2. Parameters from Figure 5-6

Feedback Mode		SG/TC Mode	
<i>d</i> , nm	<i>k</i> ⁰ , cm/s,	<i>d</i> , nm	<i>k</i> ⁰ cm/s
45	13	36	17
52	12	42	14
74	8.1	60	10
116	5.2	99	6
168	3.6	146	4.1
309	1.9	271	2.2

5.3.6 Effects of Contaminants from Air and Water

Here, we estimate the effects of organic impurities in air and water on the electroactivity of the HOPG surface by estimating its coverage with the contaminants. Specifically, we assume that the adsorption of organic impurities to the planar macroscopic surface is diffusion-limited and irreversible to yield a surface coverage, θ , as

$$\theta = \frac{2c_c\sqrt{D_c t/\pi}}{6.3 \times 10^{-9} (\text{mol}/\text{cm}^2)} \quad (2)$$

where c_c and D_c are the concentration and diffusion coefficient of organic impurities in air or water, respectively, and t is the duration of contamination, and the denominator represents the density of graphitic carbon atoms. The numerator of eq 2 was obtained by integrating the diffusional flux of organic impurities from air (or water) to the macroscopic electrode surface as given by the Cottrell equation (see Supporting Information), where the convective transport of the impurities was neglected.

Eq 2 was used to find the HOPG surface is mainly covered with a monolayer amount of airborne contaminants owing to their high diffusion coefficient ($D_c = \sim 0.1 \text{ cm}^2/\text{s}$) in ambient air. If a graphitic surface is exposed to ambient air in a typical laboratory environment ($c_c = 20 \text{ ppm v/v}$, i.e., $0.15 \text{ }\mu\text{M}$ benzene as a model for the sake of generality⁴³), $\theta = 1.0$ is reached in 7 minutes, which is nearly equal to the time required for integrating a freshly peeled HOPG surface into an SECM cell in our experiment. In addition, this theoretical prediction is consistent with recent studies,^{4,6} which demonstrated a monolayer coverage of HOPG with airborne hydrocarbons at ~ 10 minutes. Eq 2 also gives $\theta = 0.16$ for $t = 10 \text{ s}$, which was required for protecting the exfoliated HOPG surface with a solution in the previous electrochemical studies of HOPG electrochemistry.⁷ This result indicates that a contamination-free HOPG surface (e.g., $\theta < 0.01$) is practically unobtainable by preparing the surface in ambient air. Eq 1 predicts that $\theta < 0.01$ can be maintained for 25 minutes when a graphitic surface is exposed to ultrapure gas with $c_c < 0.1 \text{ ppm v/v}$ ($< 0.75 \text{ nM}$ benzene).

We used eq 2 also to estimate the coverage of the HOPG surface with organic impurities in ultrapure water. Typically, the HOPG surface is exposed to ultrapure water for 1 hour in nanogap voltammetry, which is much longer than the surface is exposed to ambient air. Moreover, the concentration of organic impurities in 20 ppb-TOC water ($c_c = 0.28 \text{ }\mu\text{M}$ for benzene) is higher than that in ambient air (see above). A much smaller θ value of 0.06, however, was obtained from eq 2 owing to a much lower D_c value of $\sim 10^{-5} \text{ cm}^2/\text{s}$ in water. We propose that trace organic impurities in 20 ppb-TOC water significantly lower the electroactivity of the HOPG surface because pinholes through its airborne contaminant layer are filled by organic impurities in water to effectively block the access of aqueous redox species to the underlying HOPG surface (Figure 5-7A). By contrast, a very low θ value of 0.005 is obtained from eq 2 for a macroscopic electrode immersed for 1 hour in UV-treated ultrapure water (i.e., 2 ppb TOC for 28 nM benzene). The UV-treated ultrapure water seems pure enough to maintain the

pinholes of the airborne contaminant layer (Figure 4-7B) as indicated by approach curve experiments in 2 and ~1 ppb-TOC water (Figure 5-5).

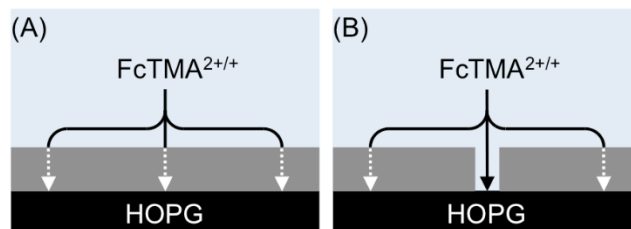


Figure 5-7. Scheme of diffusional transport of $\text{FcTMA}^{2+/+}$ (or FcTMA^+) through a contaminant layer on the HOPG surface in (A) 20 and (B) 2 ppb-TOC water.

5.4 CONCLUSION

In this work, we employed nanogap voltammetry based on SECM to sensitively detect the adsorption of organic impurities from ultrapure water to the HOPG surface as evidenced by using the simple $\text{FcTMA}^{2+/+}$ couple. Significantly, our nanogap voltammetry approach is the only electrochemical method that is powerful enough to reveal the anomalous electrochemical behaviors of a contaminated HOPG surface, which requires the quantitative kinetic study of both the oxidation and the reduction of a redox couple under high mass transport conditions. The electroactivity of a contaminated HOPG surface to the $\text{FcTMA}^{2+/+}$ couple is high enough to obtain reversible cyclic voltammograms under much lower mass transport conditions. The SECM–AFM studies of a contaminated HOPG surface were limited to the qualitative interpretation of heterogeneous images due to surface contamination.^{12,13} By contrast, such adventitious contamination of a HOPG surface was neither considered nor noticed in the SECCM studies,^{9,11} where the graphitic surface was always exposed to air or inert gas to intrinsically cause surface contamination during imaging. The quick and serious airborne hydrocarbon contamination of a HOPG

surface has been confirmed by water contact angle measurement, ATR-FTIR, and ellipsometry,^{4,6} while our electrochemical approach complimentary assesses surface contamination in ultrapure water.

The elimination of a surface contaminant layer from a graphite surface is a challenging task, which is required for studying the intrinsic electroactivity of a pristine surface. Contamination with hydrocarbons is unavoidable in ambient air even for a macroscopic graphitic electrode. We predict theoretically that a clean graphitic surface can be maintained only in a highly pure gas with an extremely low hydrocarbon content. Commercially available glove bags, however, control only humidity and the oxygen level and use plasticizers and glues, which seriously contaminate graphitic surfaces.⁴ The contamination of a graphitic surface in ultrapure water can be prevented for a macroscopic electrode by using UV-treated ultrapure water with a TOC value of ~2 ppb. The lowest TOC value of 1 ppb for commercial water purifiers available on the market today may be not low enough to prevent the organic contamination of micrometer- and nanometer-sized graphitic electrodes owing to their small size and efficient diffusional mass transport. In this study, the sufficiently clean surface of a ~1 μm -diameter Pt electrode is ensured by highly positive approach curve at a Au substrate as well as by its excellent fit with a theoretical curve (Figure 5-2). By contrast, submicrometer- and nanometer-sized carbon tips with small *RG* shows only a very low positive feedback effect that deviates from a theoretical curve.^{48,49}

5.5 SUPPORTING INFORMATION

5.5.1 FIB milling

The incident angle of focused Ga^+ beam was systematically changed to precisely control the angle of the end of ~1 μm -diameter Pt tips with respect to their axis. The milled tip end was tilted with respect to the tip axis when the Ga^+ beam was perpendicular to the tip axis (Figure 5-8A). This tilt angle is due to Gaussian tail in the energy distribution of the Ga^+ beam and depends on the sputtering rates of the milled materials. To compensate the tilt angle, the incident angle of the Ga^+ beam with respect to the tip axis was systematically varied by tilting the sample stage (Figure 5-8B). The tip surface was most

perpendicular to the tip axis when the sample stage was tilted by 1.5° , thereby achieving the closest tip–substrate distance of 12 nm (Figure 5-2). With tilt angles of 1.0° and 2.0° , the closest distances were limited to 23 and 24 nm, respectively (Figure 5-9).

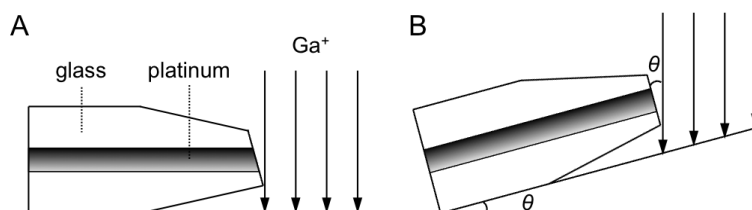


Figure 5-8. Scheme of FIB milling of glass-sealed Pt tips (A) without and (B) with tilting the sample stage.

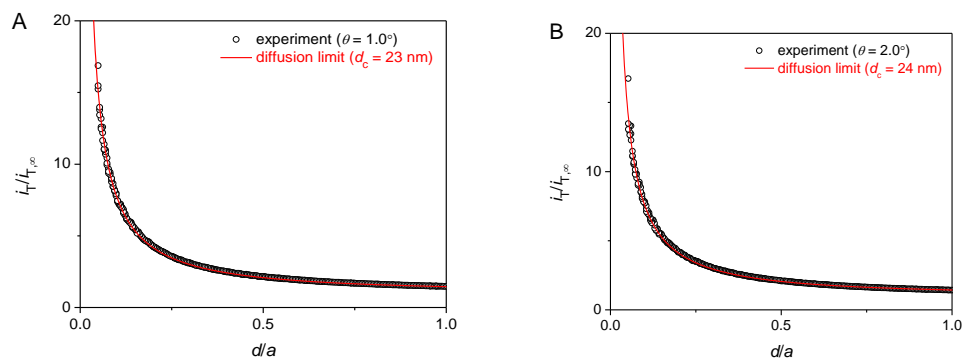


Figure 5-9. Experimental (circles) and theoretical (red line) approach curves at an unbiased Au substrate in 0.5 mM FcMeOH and 0.1 M KCl as obtained by FIB-milled Pt tips with $(\theta, a, \text{RG}) = (1.0^\circ, 0.47 \mu\text{m}, 2.1)$ and $(2.0^\circ, 0.47 \mu\text{m}, 1.8)$ in (A) and (B), respectively. Probe scan rate, 19 nm/s.

5.5.2 Feedback Current at Tip–Substrate Contact

3D finite element simulation was performed by using COMSOL Multiphysics (version 3.5a, COMSOL, Inc., Burlington, MA) to obtain positive and negative feedback current at the contact of a disk-shaped tip with conductive and insulating substrates, respectively. The details of the finite element simulation are given in the attached simulation report. The tip current at contact, $i_{T,c}$, was normalized with respect to $i_{T,\infty}$. In this simulation, the substrate was tilted with respect to the tip surface as defined by an

angle, θ_c , within a range of 1° – 3° (inset of Figure 5-10A). In addition, tip RG was changed within a range of 1.1–10 to demonstrate that higher positive feedback effect is expected with smaller RG (Figure 5-10A). This result is due to a shorter contact distance for a tip with smaller RG as given by

$$\frac{d_c}{a} = RG \sin \theta_s \quad (3)$$

In fact, higher positive feedback effect is also seen for a smaller tilt angle (Figure 4-10A) as expected from eq 3. Importantly, a sharper tip with smaller RG is also advantageous to observe more negative feedback effect owing to the shorter contact distance as predicted by eq 3 (Figure 5-10B). The most negative feedback response is expected with $RG = 1.8$ – 2.0 , which depends on the tilt angle. With smaller RG , less negative feedback is expected because of the leakage of the thin-layer cell formed between the tip and the substrate.

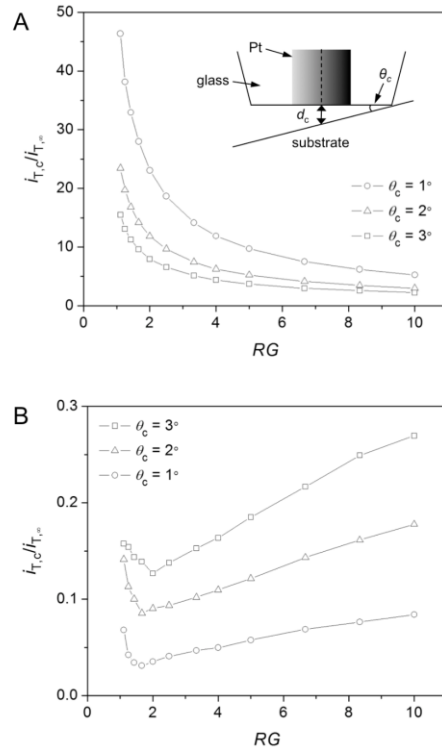


Figure 5-10. Simulated tip current at the contact of a disk-shaped tip with (A) conductive or (B) insulating substrate tilted by θ_c (see the inset of part A).

5.5.3 Sealed SECM Cell

SECM measurements with HOPG were carried out by using a sealed SECM cell (Figure 5-11) to minimize the contamination of the aqueous electrolyte solution with airborne organic impurities during the measurement.

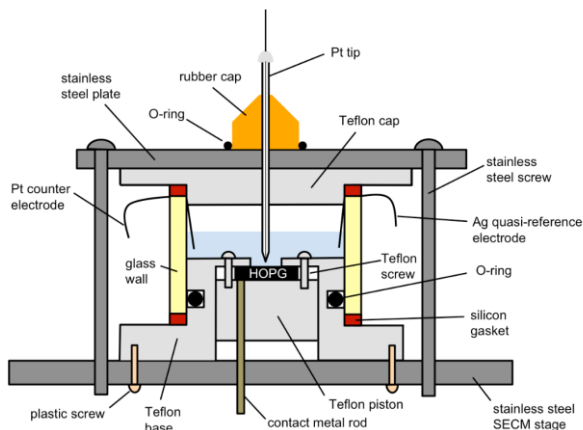


Figure 5-11. Scheme of a SECM cell with an aqueous solution in the compartment based on glass wall and Teflon cap and base.

5.5.4 Water Purification with Old Filters

Figure 5-12 shows an experimental approach curve at HOPG in ultrapure water that was purified by using 17 month-old filters. The resistivity of the ultrapure water was still 18.2 M Ω cm. The positive feedback effect, however, was very small as expected from a kinetically limited curve. The serious passivation of the HOPG surface is also seen in nanogap voltammograms (Figure 5-4).

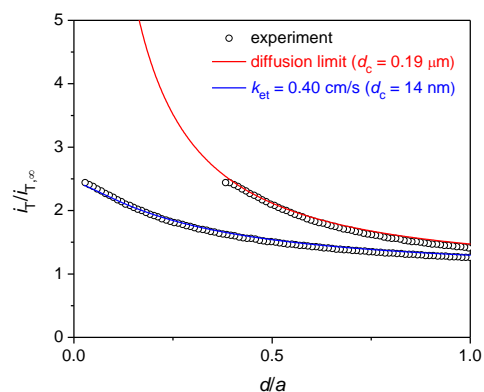


Figure 5-12. Experimental (circles) and theoretical (solid lines) approach curves at HOPG in 0.3 mM FcTMA⁺ and 0.05 M KCl in water purified by old filters. The theoretical curve used $a = 0.48 \mu\text{m}$ and $RG = 1.8$.

5.5.5 CV of FcTMA⁺ at HOPG

The current at the HOPG was measured during nanogap voltammetry to obtain a reversible CV of FcTMA⁺ in ultrapure water purified through the 17 month-old filters of the nanopure water system (Figure 5-13). This CV gives a peak separation of $\sim 60 \text{ mV}$ as well as a $E^{0'}$ value of 0.34 V vs. Ag/AgCl.

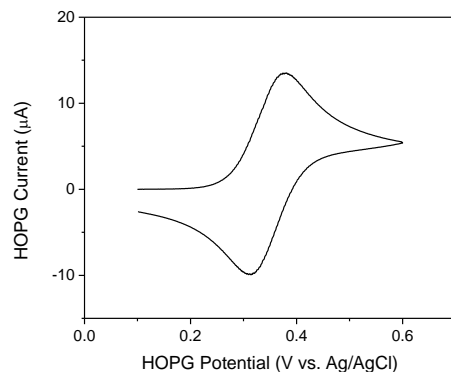


Figure 5-13. A reversible CV of FcTMA⁺ at the HOPG surface in ultrapure water purified by using 17 months old filters for the Nanopure water purifier.

5.5.6 Elemental Analysis of Ultrapure Water

We employed ICP-MS to determine the concentrations of various elements in ultrapure water without and with filtration through the activated-carbon filter, i.e., VOC pak (Millipore), as listed in Table 5-3. The low nanomolar levels of Fe and Zn were detected in the VOC-filtered water. The concentration of Cr was somehow lowered after filtration.

Table 5-3. Concentrations of Various Elements in Ultrapure Water

element	no filter	VOC	element	no filter	VOC
Ag	<1 ppt	<1 ppt	Mn	<1 ppt	4 ppt
Au	<1 ppt	<1 ppt	Pd	<1 ppt	<1 ppt
Co	<1 ppt	<1 ppt	Pt	<1 ppt	<1 ppt
Cr	5 ppt	1 ppt	Rh	<1 ppt	<1 ppt
Cu	<1 ppt	1 ppt	Ru	<1 ppt	<1 ppt
Fe	2 ppt	75 ppt	Tl	<1 ppt	<1 ppt
Ir	<1 ppt	<1 ppt	Zn	<5 ppt	50 ppt

5.5.7 Tunneling Current between the Pt Tip and HOPG

We often observed tunneling current between the Pt tip and the HOPG substrate when nanogap voltammetry was measured at short tip substrate distances in <3 ppb-TOC ultrapure water (Figure 5-13). Such tunneling current was not observed by using ~20 ppb-TOC ultrapure water.

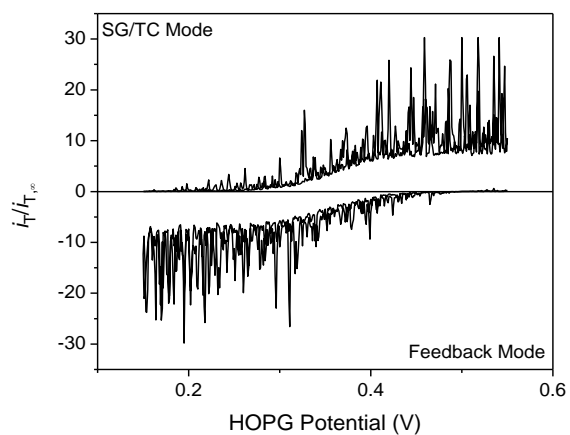


Figure 5-14. Tunneling current on nanogap voltammograms at HOPG in 0.3 mM FcTMA⁺ and 0.05 M KCl in ~1 ppb-TOC water. Potential sweep rate, 0.05 V/s.

ACKNOWLEDGEMENTS

This work was supported by the National Science Foundation (CHE-1213452). We thank Prof. Richard L. McCreery, Department of Chemistry, University of Alberta, for helpful discussion about HOPG electrochemistry. We also thank Prof. Stephen G. Weber and Jing Zhang, Department of Chemistry, University of Pittsburgh, for their advice on lowering the TOC of ultrapure water. Frank Ingellis, Millipore, is acknowledged for TOC measurement. R.C. thanks for the graduate study fellowship from the Arts and Sciences, University of Pittsburgh.

5.6 REFERENCES

- (1) McCreery, R. L.; Cline, K. K. In *Laboratory Techniques in Electroanalytical Chemistry*; Kissinger, P. T., Heineman, W. R., Eds.; Marcel Dekker: New York, 1996, p 293.
- (2) McCreery, R. L. In *Interfacial electrochemistry: theory, experiment, and applications*; Wieckowski, A., Ed.; Marcel Dekker: New York, 1999, p 631.
- (3) Swain, G. M. In *Handbook of Electrochemistry*; Zoski, C. G., Ed.; Elsevier: New York, 2007, p 111.
- (4) Li, Z.; Wang, Y.; Kozbial, A.; Shenoy, G.; Zhou, F.; McGinley, R.; Ireland, P.; Morganstein, B.; Kunkel, A.; Surwade, S. P.; Li, L.; Liu, H. *Nat. Mater.* **2013**, *12*, 925.
- (5) Kozbial, A.; Li, Z.; Conaway, C.; McGinley, R.; Dhingra, S.; Vahdat, V.; Zhou, F.; D'Urso, B.; Liu, H.; Li, L. *Langmuir* **2014**, *30*, 8598.
- (6) Kozbial, A.; Li, Z.; Sun, J.; Gong, X.; Zhou, F.; Wang, Y.; Xu, H.; Liu, H.; Li, L. *Carbon* **2014**, *74*, 218.
- (7) McDermott, M. T.; Kneten, K.; McCreery, R. L. *J. Phys. Chem.* **1992**, *96*, 3124.
- (8) Güell, A. G.; Ebejer, N.; Snowden, M. E.; Macpherson, J. V.; Unwin, P. R. *J. Am. Chem. Soc.* **2012**, *134*, 7258.
- (9) Lai, S. C. S.; Patel, A. N.; McKelvey, K.; Unwin, P. R. *Angew. Chem. Int. Ed.* **2012**, *51*, 5405.
- (10) Snowden, M. E.; Guell, A. G.; Lai, S. C. S.; McKelvey, K.; Ebejer, N.; O'Connell, M. A.; Colburn, A. W.; Unwin, P. R. *Anal. Chem.* **2012**, *84*, 2483.
- (11) Patel, A. N.; Collignon, M. G.; O'Connell, M. A.; Hung, W. O. Y.; McKelvey, K.; Macpherson, J. V.; Unwin, P. R. *J. Am. Chem. Soc.* **2012**, *134*, 20117.
- (12) Frederix, P.; Bosshart, P. D.; Akiyama, T.; Chami, M.; Gullo, M. R.; Blackstock, J. J.; Dooleweerd, K.; de Rooij, N. F.; Stauffer, U.; Engel, A. *Nanotechnology* **2008**, *19*.
- (13) Wain, A. J.; Pollard, A. J.; Richter, C. *Anal. Chem.* **2014**, *86*, 5143.

- (14) Amemiya, S.; Bard, A. J.; Fan, F.-R. F.; Mirkin, M. V.; Unwin, P. R. *Annu. Rev. Anal. Chem.* **2008**, *1*, 95.
- (15) *Scanning Electrochemical Microscopy*; 2nd ed.; Bard, A. J.; Mirkin, M. V., Eds.; Taylor and Francis: New York, 2012.
- (16) Eifert, A.; Kranz, C. *Anal. Chem.* **2014**, *86*, 5190.
- (17) McCreery, R. L. *Chem. Rev.* **2008**, *108*, 2646.
- (18) McCreery, R. L.; McDermott, M. T. *Anal. Chem.* **2012**, *84*, 2602.
- (19) Nioradze, N.; Kim, J.; Amemiya, S. *Anal. Chem.* **2011**, *83*, 828.
- (20) Clark, K.; Retzik, M.; Darbouret, D. *Ultrapure Water* **1997**, *14*, 21.
- (21) Sun, P.; Mirkin, M. V. *Anal. Chem.* **2006**, *78*, 6526.
- (22) Kabagambe, B.; Garada, M. B.; Ishimatsu, R.; Amemiya, S. *Anal. Chem.* **2014**, *86*, 7939.
- (23) Gabler, R.; Hegde, R.; Hughes, D. *J. Liq. Chromatogr.* **1983**, *6*, 2565.
- (24) Kim, J.; Izadyar, A.; Nioradze, N.; Amemiya, S. *J. Am. Chem. Soc.* **2013**, *135*, 2321.
- (25) Nioradze, N.; Chen, R.; Kim, J.; Shen, M.; Santhosh, P.; Amemiya, S. *Anal. Chem.* **2013**, *85*, 6198.
- (26) Kim, J.; Kim, B.-K.; Cho, S. K.; Bard, A. J. *J. Am. Chem. Soc.* **2014**, *136*, 8173.
- (27) Kim, J.; Shen, M.; Nioradze, N.; Amemiya, S. *Anal. Chem.* **2012**, *84*, 3489.
- (28) Shoup, D.; Szabo, A. *J. Electroanal. Chem.* **1984**, *160*, 27.
- (29) Cornut, R.; Lefrou, C. *J. Electroanal. Chem.* **2007**, *604*, 91.
- (30) Lefrou, C. *J. Electroanal. Chem.* **2006**, *592*, 103.
- (31) Velmurugan, J.; Sun, P.; Mirkin, M. V. *J. Phys. Chem. C* **2008**, *113*, 459.
- (32) Cornut, R.; Lefrou, C. *J. Electroanal. Chem.* **2008**, *621*, 178.
- (33) Shen, M.; Ishimatsu, R.; Kim, J.; Amemiya, S. *J. Am. Chem. Soc.* **2012**, *134*, 9856.
- (34) Rodgers, P. J.; Amemiya, S.; Wang, Y.; Mirkin, M. V. *Anal. Chem.* **2010**, *82*, 84.

- (35) Wang, Y.; Velmurugan, J.; Mirkin, M. V.; Rodgers, P. J.; Kim, J.; Amemiya, S. *Anal. Chem.* **2010**, *82*, 77.
- (36) Lee, C.-Y.; Guo, S.-X.; Bond, A. M.; Oldham, K. B. *J. Electroanal. Chem.* **2008**, *615*, 1.
- (37) Davies, T. J.; Moore, R. R.; Banks, C. E.; Compton, R. G. *J. Electroanal. Chem.* **2004**, *574*, 123.
- (38) Kirkman, P. M.; Güell, A. G.; Cuharuc, A. S.; Unwin, P. R. *J. Am. Chem. Soc.* **2013**, *136*, 36.
- (39) Zhang, G.; Kirkman, P. M.; Patel, A. N.; Cuharuc, A. S.; McKelvey, K.; Unwin, P. R. *J. Am. Chem. Soc.* **2014**, *136*, 11444.
- (40) Clark, K.; Retzik, M.; Darbournet, D. *Ultrapure Water* **1997**, *14*, 21.
- (41) Rodgers, P. J.; Amemiya, S. *Anal. Chem.* **2007**, *79*, 9276.
- (42) Guell, A. G.; Ebejer, N.; Snowden, M. E.; McKelvey, K.; Macpherson, J. V.; Unwin, P. R. *Proc. Natl. Acad. Sci. U.S.A.* **2012**, *109*, 11487.
- (43) Scherson, D. A.; Tolmachev, Y. V. *Electrochem. Solid-State Lett.* **2010**, *13*, F1.
- (44) Ugeda, M. M.; Brihuega, I.; Guinea, F.; Gomez-Rodriguez, J. M. *Phys. Rev. Lett.* **2010**, *104*, 4.
- (45) Ruffieux, P.; Gröning, O.; Schwaller, P.; Schlapbach, L.; Gröning, P. *Phys. Rev. Lett.* **2000**, *84*, 4910.
- (46) Niimi, Y.; Matsui, T.; Kambara, H.; Tagami, K.; Tsukada, M.; Fukuyama, H. *Phys. Rev. B* **2006**, *73*, 085421.
- (47) Chang, H.; Bard, A. J. *Langmuir* **1991**, *7*, 1143.
- (48) Takahashi, Y.; Shevchuk, A. I.; Novak, P.; Babakinejad, B.; Macpherson, J.; Unwin, P. R.; Shiku, H.; Gorelik, J.; Klenerman, D.; Korchev, Y. E.; Matsue, T. *Proc. Natl. Acad. Sci. U.S.A.* **2012**, *109*, 11540.
- (49) McKelvey, K.; Nadappuram, B. P.; Actis, P.; Takahashi, Y.; Korchev, Y. E.; Matsue, T.; Robinson, C.; Unwin, P. R. *Anal. Chem.* **2013**, *85*, 7519.

6.0 CONCLUSIONS

The first chapter described the development of a novel SECM approach to enable quasi-steady-state voltammetry of rapid ET reactions at macroscopic substrates. The wide range of substrate potentials is applicable under quasi-steady-state conditions to cover both cathodic and anodic regions far from E^0 , one of which reaches the limited range of substrate potentials employed in the traditional steady-state feedback mode. Subsequently, a pair of quasi-steady-state i_T - E_S voltammograms is obtained in both feedback and SG/TC modes to enable the separate and reliable determination of all transport (D_O , D_R , and d), thermodynamic (E^0), and kinetic (R and k^0) parameters. This quasi-steady-state approach requires a short tip-substrate distance and a reversible reaction at a macroscopic substrate except under the tip to be intrinsically suitable for the kinetic study of a rapid substrate reaction, which can be slowed at substrate potentials around E^0 and probed both cathodically and anodically under high mass-transport conditions. In fact, k^0 values of up to ~ 7 cm/s for TCNQ as obtained by this approach are the largest determined for a substrate reaction by SECM.

The third chapter employed the Marcus-Hush-Chidsey formalism to theoretically predict that MHC voltammetric behavior will be manifested by SECM-based i_T - E_S voltammetry under nanoscale mass transport conditions. Our voltammetric theory is generally applicable to any steady-state and quasi-steady-state condition with arbitrary substrate potential and both feedback and SG/TC modes. The deviation from the classical BV model should be considered for the comprehensive range of nanoscale SECM measurements except for fastest heterogeneous ET reactions reported so far ($k^0 > 1$ cm/s). Our prediction is also extended to steady-state voltammetry of ET reactions at nanometer-sized SECM tips positioned above conductors because tip voltammetry can be well described by the general theory that is analogous to the theory for i_T - E_S voltammetry. No prior knowledge of the rate law is required for the analysis of the retraceable portion of an i_T - E_S voltammogram, which can be directly converted to a plot of ET rate constant versus substrate potential using analytical equations developed in this work.

In the third chapter we reported on the electrostatic and electrochemical origins of nanometer-scale damage to glass-sealed Pt UMEs with submicrometer and nanometer size. Both types of damage are severe with the small UMEs, which are readily charged up by a small number of electrons without potentiostatic control. Importantly, ESD damage to a UME in air can be avoided by protecting the UME from a source of electrostatic charge, most importantly, an operator. The body and cloth of the operator must be grounded by using ESD-safe wrist strap, gloves, and lab coat. Electrochemical damage is likely due to the flow of a transient current from a potentiostat amplifier into a UME and can be avoided by maintaining the UME under potentiostatic control in solution. This control can be lost transiently when connection of a potentiostat to the UME is internally switched on or off. The new concept of nanoscale electrode damage proposed in this work is general and must be considered broadly for reliable nanoelectrochemical measurements and applications. Both electrostatic and electrochemical damage is possible with any submicrometer- or nanometer-size metal UME including an insulated metal tip for scanning tunneling microscopy. Moreover, “nano ESD” is a global concern in nanoelectronics including the batteries and sensors based on nanostructured electrodes.

In chapter 5, we employed nanogap voltammetry based on SECM to sensitively detect the adsorption of organic impurities from ultrapure water to the HOPG surface as evidenced by using the simple $\text{FcTMA}^{2+/+}$ couple. Contamination with hydrocarbons is unavoidable in ambient air even for a macroscopic graphitic electrode. We predict theoretically that a clean graphitic surface can be maintained only in a highly pure gas with an extremely low hydrocarbon content. Commercially available glove bags, however, control only humidity and the oxygen level and use plasticizers and glues, which seriously contaminate graphitic surfaces. The contamination of a graphitic surface in ultrapure water can be prevented for a macroscopic electrode by using UV-treated ultrapure water with a TOC value of ~ 2 ppb. The SECM–AFM studies of a contaminated HOPG surface were limited to the qualitative interpretation of heterogeneous images due to surface contamination. By contrast, such adventitious contamination of a HOPG surface was neither considered nor noticed in the SECCM studies, where the graphitic surface was

always exposed to air or inert gas to intrinsically cause surface contamination during imaging. Significantly, our nanogap voltammetry approach is the only electrochemical method that is powerful enough to reveal the anomalous electrochemical behaviors of a contaminated HOPG surface, which requires the quantitative kinetic study of both the oxidation and the reduction of a redox couple.

The quasi-steady-state approach developed in this work will find various applications beyond the study of rapid substrate reactions. For instance, the separate assessment of transfer coefficient for cathodic and anodic reactions will be important when the double layer or Marcus-Hush effect is significant. A voltammetric SG/TC measurement with a macroscopic substrate at quasi-steady-state is complementary to the true steady-state counterpart with an ultramicroelectrode substrate as recently developed for the SG/TC study of short-lived intermediates.

The analytical approach developed in the third chapter facilitates applications of i_T-E_S voltammetry to non-BV systems based on electrocatalysis, charge-transfer at liquid/liquid interfaces, nanoparticle-mediated ET at gold electrodes modified with self-assembled monolayers, and ET at single-walled carbon nanotubes and graphenes. In fact, nanoscale mass transport is inevitable when individual single-walled carbon nanotubes are investigated as SECM substrates.

Achievements in this work will make contribution not only in scientific field but also in practical application of nanoscale electrochemistry in nanotechnology. The developed nanogap-enabled SECM will help to locally study electrochemical reactivity of different nanostructured materials such as graphene and carbon nanotubes. Nanofabricated, reliable ultramicroelectrodes for SECM will find application in the electrochemical mapping of surfaces and interfaces, imaging and activity measurements of individual biological assemblies, whether in vivo or in vitro. This could lead to advances in areas such as nanobiotechnology and molecular biology.

Based on these accomplishments, the capacity of nanoscale SECM will be greatly increased to characterize and understand various nanomaterials and interfaces at the nanoscale.